

Fluidic Self-Assembly of Millimeter-Scale Thin Parts at Air-Water Interface

Kwang Soon Park

A dissertation
submitted in partial fulfillment of the
requirements for the degree of

Doctor of Philosophy

University of Washington

2012

Reading Committee:
Karl F. Böhringer, Chair
Rajashree Baskaran
Eric Klavins

Program Authorized to Offer Degree:
Electrical Engineering

University of Washington

ABSTRACT

Fluidic Self-Assembly of Millimeter-Scale Thin Parts at Air-Water Interface

Kwang Soon Park

Chair of the Supervisory Committee:

Professor Karl F. Böhringer

Electrical Engineering

This dissertation focuses on a novel method to achieve high yield assembly of millimeter-scale thin silicon parts from an air-water interface. Surface functionalized silicon parts assemble in preprogrammed hydrophilic locations on an assembly substrate with self-alignment in unique orientation. The process and design factors are systematically analyzed and optimized using DOE (Design of Experiment) that leads to high yield.

First, a novel fluidic self-assembly (FSA) at the air–water interface is introduced. An experimental and theoretical study of a high yield self-assembly process with a surface programmable template is undertaken and modeled. An analysis of the fluidic self-assembly method at an air–water interface is presented with an emphasis on the combined effect of a substrate tilting angle and part size. For 1×1 , 3×3 and 5×5 mm² parts with 100 μm thickness, the substrate tilting angles for effective assembly are experimentally determined and the surface tension induced torques are derived based on a newly developed model. The analysis result indicates that there is a limit on the lateral size of the parts that can be assembled when only one substrate tilting angle is used. Based on the analysis, a novel method, which is capable of assembling parts of higher lateral dimensions using parametric changes in the substrate tilting angle, is proposed. Due to no control over the rotational angle, square parts are assembled in four possible orientations (0°, 90°, 180°, 270°) due to their square shape.

The FSA method is improved to achieve orientation-specific FSA of millimeter-scale thin parts

by adding magnetic materials. The effect of magnetic force is analyzed and a critical magnetic force that guarantees successful assembly is systematically derived. For various gap values between a magnet and Ni patterned parts, magnetic force distributions are generated using Monte-Carlo simulation and employed to predict assembly yield. An analysis of these distributions shows that a decline in yield following the probability density function can be expected with degrading conditions. Experimentally determined critical magnetic forces are in good agreement with derived values from a model of competing forces acting on a part. A general set of design guidelines is also presented from the developed model and experimental data.

Based on an analysis of the magnetic force, a parallel heterogeneous assembly method is developed. The FSA system selectively assembles appropriate parts at corresponding sites from a mixed collection of $2000 \times 2000 \times 100$ and $4000 \times 4000 \times 100 \mu\text{m}^3$ parts using a single pull-up process. A statistical analysis of the distributions of magnetic forces delimits the suitable range for the strength of Faraday waves to fix non-optimal initial placements and orientations.

Besides the square patterned parts, orientation-specific assembly of thin circular parts (diameter 2 mm, thickness $100 \mu\text{m}$) is demonstrated. Components for optics (camera, microlens on photovoltaic cells), sensors, actuators and MEMS devices are often in a circular shape because of simple and symmetric design. Thus, assembly of thin circular parts in unique orientation is required. Large deviation of rotation angle of parts is improved by optimizing magnet position through the analysis of in-plane magnetic fields, which induces the dominant force after the parts are placed in the trench.

The detailed effect of fluid viscosity on FSA performance is studied through experimental and analytical approaches. The FSA method is subdivided into three process steps (approach, rotation, pull-up) and their viscosity dependency is investigated. The detailed effect of viscosity on assembly speed and yield is studied using a derived modeling equation and experimental results. The effect of the feedback control at different fluid viscosities is also analyzed.

As extension of 2D self-assembly, the first proof-of-concept of 3D integration using the proposed FSA of chip-scale parts ($100 \mu\text{m}$ thickness) is presented. 3D integration is achieved by assembling new parts over previously assembled parts. Assembly proceeds as an assembly substrate is pulled up through an air-water interface and electrical and mechanical bonding is achieved through a solder reflow process. The maximum number of layers that can be achieved is simulated and analyzed. Via resistance including the effect of degradation of solder over repeated reflow process is measured.

Inspired by the analysis of the response of the Ni patterned parts to the magnetic field, a novel self-assembly of a 3D structure by controlling a folding angle is realized. The tendency of

ferromagnetic thin Ni patterns to align along magnetic flux triggers self-folding after the capillary force is diminished. Two strategies to control folding angle are presented with experimental results. As a proof of concept, a millimeter-scale bus (folding angle = 90°) and pyramid shaped (folding angle $> 90^\circ$) are assembled.

Three future works are proposed as extended applications of described assembly methods. First, a pyramid shaped 3D photovoltaic cell is proposed. It increases light absorption by trapping reflected light. Second, self-disassembly in analogues to sculpting to build a desired 3D structure is described. Third, a novel 3D printing strategy that prints a 3D structure from top to bottom using small parts in a ultrasonic- or x-ray-transparent container is presented.

TABLE OF CONTENTS

	Page
ABSTRACT	i
LIST OF FIGURES	vii
LIST OF TABLES	xiv
ACKNOWLEDGMENTS	xvi
CHAPTER 1. Introduction	1
CHAPTER 2. Fluidic Self-Assembly of Millimeter Scale Thin Parts at Air-Water Interface	6
2.1 Introduction	6
2.2 Fabrication	7
2.3 Parameter selection through screening test	8
2.4 Parameter analysis	8
2.5 Optimization and 100 % assembly	11
2.6 Effect of Faraday waves	14
2.7 Conclusion	16
CHAPTER 3. Mechanics and Scaling of Self-Assembly of Thin Parts at Air-Water Interface	17
3.1 Introduction	17
3.2 Part size scaling	17
3.3 Assembly model	20
3.4 Single angle assembly	22
3.5 Feedback assembly for large parts	23
3.6 Conclusions	24
CHAPTER 4. Orientation Controlled Parallel Assembly Using Magnetic Field	25
4.1 Introduction	25
4.2 Assembly process	25
4.3 Fabrication	28
4.4 The effect of Faraday waves	29
4.5 The effect of magnetic field	32
4.6 Assembly model	35
4.6.1 Shape of meniscus	36

4.7	Model verification.....	37
4.8	Design guidelines.....	39
4.8.1	Parameter selection.....	39
4.8.2	System design.....	39
4.9	Conclusions.....	41
CHAPTER 5. Parallel Heterogeneous Integration.....		43
5.1	Introduction.....	43
5.2	Assembly process.....	43
5.3	Approach violations.....	45
5.4	Selection of strength of Faraday waves.....	47
5.5	Conclusions.....	48
CHAPTER 6. Self-Assembly of Thin Circular Parts.....		49
6.1	Introduction.....	49
6.2	Assembly process.....	49
6.2.1	System setup.....	49
6.2.2	Assembly overview.....	49
6.3	Optimization of part rotation.....	50
6.3.1	Assembly performance.....	50
6.3.2	Part rotation in a binding site.....	52
6.3.3	Optimization.....	52
6.4	Conclusions.....	54
CHAPTER 7. Effect of Viscosity.....		55
7.1	Introduction.....	55
7.2	Fluidic self-assembly strategy.....	55
7.2.1	FSA system setup.....	55
7.2.2	Assembly process.....	55
7.3	Effect of viscosity.....	58
7.3.1	Approach.....	58
7.3.2	Assembly yield and speed.....	66
7.4	Conclusion.....	69

CHAPTER 8. 3D Integration Using Self-Assembly	70
8.1 Introduction	70
8.2 Assembly process	70
8.2.1 Overview of FSA with unique orientation	70
8.2.2 Fabrication	73
8.3 Results	75
8.3.1 3D integration using self- assembly	75
8.4 Conclusions	78
CHAPTER 9. 3D Origami	79
9.1 Introduction	79
9.2 Assembly overview	79
9.2.1 2D assembly	80
9.2.2 Fabrication	81
9.3 3D structures via self-folding	81
9.3.1 Self-folding	81
9.3.2 The bus ($\theta_f = 90^\circ$) and pyramid ($\theta_f > 90^\circ$)	83
9.4 Conclusions	85
CHAPTER 10. Conclusions and Future work	86
10.1 Conclusions	86
10.2 Future work	87
10.2.1 3D photovoltaic cell	87
10.2.2 Self-disassembly using reusable smart aand	89
10.2.3 3D printing	89
References	91

LIST OF FIGURES

Figure 2.1: The experimental setup consists of a water container, linear electromagnetic vibration table, dip coater, substrate and parts floating at air-water interface.	6
Figure 2.2: Contact angle change during pull-up. Parts will be assembled on the oxide area with a thin water layer. (a) High contact angle for the approach of part. (b) Water remains on the oxide area for assembly.	7
Figure 2.3: Effect with slope of four factors to assembly yield. X-axis presents the factor levels and Y-axis indicates yield.	9
Figure 2.4: Contour plots of assembly yield versus agitation frequency (x-axis) and amplitude (y-axis) for four substrate designs in Table 2.3.	10
Figure 2.5: Contour plots of assembly yield versus agitation frequency (x-axis) and amplitude (y-axis) for four substrate designs in Table 2.4.	12
Figure 2.6: Parts ($1 \times 1 \text{ mm}^2$ parts with $100 \text{ }\mu\text{m}$ thickness) rearrangement by agitation. The dark squares are the hydrophilic sites and the gold regions are the hydrophobic surfaces. (a) Substrate/water interface. (b) Pull-up and pause. (c) After agitation. (d) 100 % assembly.	12
Figure 2.7: Faraday wave vs. applied frequency. As frequency increases shorter wavelength (higher k) is observed.	14
Figure 2.8: Comparison of k values. Theoretical and experimental values are compared.	15
Figure 2.9: Simulated motion of a part ($1000 \times 1000 \times 100 \text{ }\mu\text{m}^3$) at air-water interface. The initial position of a part is (70, 50) mm and vertical agitation with 80 Hz / 1.4 g is applied. Color indicates the surface level.	15
Figure 3.1: Behavior of meniscus convexity at various substrate tilting angles. The shape of the meniscus changes depending on the substrate tilting angle.	18
Figure 3.2: The behavior of meniscus convexity θ^* at various substrate tilting angles. (a) Experimental result of meniscus convexity response to substrate tilting angle for the Au/SAM surface. (b) Experimental result of meniscus convexity response to substrate tilting angle for the oxide surface. (c) Image analysis result for (a) and (b). The slope near the substrate has a linear relationship with the substrate tilting angle α and keeps	

the constant difference between hydrophobic (Au/SAM) and hydrophilic (oxide) surfaces.....	18
Figure 3.3: Part approaching the substrate. The part size is $3000 \times 3000 \times 100 \mu\text{m}^3$. (a) Abrupt change of meniscus slope prevents the part approach. (b) Low convexity helps part approach.	19
Figure 3.4: For successful assembly, the parts go through three steps: approach, flat surface and assembly.	20
Figure 3.5: Diagram for the simplified capillary torque model. Horizontal and inclined solid lines indicate the bottom oxide side of the part floating at the air-water interface and the oxide binding site under the water, respectively.	21
Figure 3.6: Analysis of the capillary torque vs. part size (1×1 , 3×3 and $5 \times 5 \text{ mm}^2$ parts with $100 \mu\text{m}$ thickness) in single angle assembly feedback assembly (see Table 3.2).	22
Figure 3.7: Schematic of feedback assembly. A part forms line contact at α_1 . The critical capillary torque is obtained at α_2 and the part is assembled by pulling up the substrate.	23
Figure 4.1: The experimental setup for orientation-specific assembly. The system consists of a water container, linear electromagnetic vibration table, dip coater, substrate, magnets and parts floating at the air-water interface.	26
Figure 4.2: Schematic of two parts on a substrate for simulation of magnetic forces. F_1 and F_2 indicate the force on a part on a binding site and on its neighboring part, respectively. Part 2 should be repelled.	26
Figure 4.3: Full process flow for orientation-specific assembly. (a) Parts approach the substrate driven by the downward meniscus and magnetic field and (b-d) are assembled by substrate pull-up. (e) Parts are attached to a final substrate. (f) The process is completed by removing assembled parts from the assembly substrate.	27
Figure 4.4: The proposed FSA system can be modified for roll-to-roll process with a flexible substrate. Instead of a magnet template, a roller with magnets attached attracts and assembles the released parts.	28
Figure 4.5: Part ($2000 \times 2000 \times 100 \mu\text{m}^3$) rearrangement by surface Faraday waves (top view). Dark squares are hydrophilic binding sites and gold regions are hydrophobic surfaces. (a) 90° correction. (b) 180° correction. (c) One binding site is empty and the other one is approached by two parts. (d) Surface Faraday waves (80 Hz, 1.5 g) are applied,	

resulting in a rearrangement of the parts.	30
Figure 4.6: Part angle distribution. (a-c) before agitation, (d-f) after agitation in a magnetic field. A peak with high density of parts oriented at -90° is observed after agitation.	31
Figure 4.7: Assembly result with unique orientation. High yield (100 %) is achieved using a visual check of one-on-one part-to-site registration for each row before substrate pull-up.	31
Figure 4.8: Experimental setup to determine the critical magnetic force F_{mc} . The magnetic force acting on the part can be controlled via the gap size.	32
Figure 4.9: Distributions of the magnetic forces, F_m with different gaps. F_m distribution is the result of Monte-Carlo simulation considering accumulated error from magnet-substrate alignment, part position and measurement error. The colored areas indicate the assembly yield. The critical magnetic force, F_{mc} is found to be $6.4 \mu\text{N}$	34
Figure 4.10: Comparison of predicted and experimental yield under the estimated critical magnetic force $F_{mc} = 6.4 \mu\text{N}$. The graph shows 11 % RMS error and 17 % maximum error.	34
Figure 4.11: Competing forces on a part during substrate pull-up. The magnetic force should be greater than the repelling force caused by gravity and the slope of meniscus.	35
Figure 4.12: The effect of the shapes of the menisci on repelling force. (a) A square patterned substrate creates a more curved meniscus. (b) The hydrophilic bottom surface of a part induces repelling force.	36
Figure 4.13: Net force change according to applied magnetic force on 2 mm sized parts with (a) a square patterned substrate and (b) a stripe patterned substrate.	38
Figure 4.14: Contour plot of the simulated magnetic forces on Part 2. Part 2 with a magnetic force of less than the critical value will be repelled and result in successful assembly. Critical design conditions for a square patterned substrate and a stripe patterned one are also shown by dotted lines.	40
Figure 5.1: Heterogeneous assembly system with parts at air-water interface. (a) Assembly system consists of a water container on a linear electromagnetic shaker, and a stepper motor. (b) The magnetic force applied on a part, as a function of the size of the Ni pattern and the distance between the Ni pattern and a magnet, determines the size of the part to be assembled.	43

Figure 5.2: Assembly process for parallel heterogeneous assembly. Randomly distributed parts (2, 4 mm) at the air-water interface approach the binding sites with unique orientation and they are assembled by substrate pull-up.44

Figure 5.3: Three approach violations in assembly process with magnetic forces determined from simulations. Correctly oriented 2 and 4 mm parts experience 10.0 and 32.5 μN , respectively. Weak magnetic force ($< 0.5 \mu\text{N}$) due to the increased gap (Ni pattern to magnet) makes the wrong parts easily repelled by weak Faraday waves. (a) 4 mm parts on 2 mm binding sites. (b) Parts in wrong orientation. (c) 2 mm parts on 4 mm binding sites.45

Figure 5.4: Faraday waves for one-to-one part-to-binding site registration. (a) Part rearrangement by Faraday waves. A 2 mm part on a 4 mm binding site is replaced with a 4 mm part after agitation. (b) Assembly is done by substrate pull-up. (c) Example of heterogeneous FSA (2 and 4 mm parts).46

Figure 5.5: Determination of gap. (a) Suitable gap is determined to be 1.1 mm for stable assembly. (b) Two distinct distributions enable differentiation by part size.47

Figure 6.1: (a) Experimental setup. (b) Three steps for assembly; part approach, flat surface/registration and assembly.50

Figure 6.2: Test setup for determination of part-to-part interaction (attraction forces).51

Figure 6.3: (a) Simulation and experimental results of the maximum force on a moving part on Faraday waves. Gravity and drag force are considered. (b) Transient response of the Faraday waves (80 Hz / 1.5 g).51

Figure 6.4: Assembly results before shifting magnets. (a) Parts are generally oriented upward but have wide deviation. (b) The distribution of orientations shows three distinct groups.52

Figure 6.5: Simulation of the in-plane magnetic fields [A/m]. (a) The top surface of the magnets are set at $z = 0$. (b) In-plane (x-y) components of magnetic fields at $z = 0.5 \text{ mm}$ where assembly occurs.53

Figure 6.6: Minimization of part rotation by shifting magnets by 0.8 mm. In-plane magnetic field and magnetic forces (a) before and (b) after shifting magnets.54

Figure 6.7: Assembly results after shifting magnets. (a) Orientation-specific assembly of 90 parts with less deviation. (b) Distribution has a standard deviation of 3.7°54

Figure 7.1: The experimental setup consists of a water container, a linear electromagnetic vibration table, a stepper motor, an assembly substrate, magnets and parts floating at the air-water interface.....	56
Figure 7.2: Full assembly process flow. (a) Parts approach the substrate driven by downward meniscus and magnetic field and (b-d) are assembled by substrate pull-up.....	57
Figure 7.3: Experimental setup to evaluate (a) a drag coefficient and (b) acceleration along the magnetic field ($d = 22$ mm).....	60
Figure 7.4: Extraction of a drag constant through graph fitting at 22°C . The equation with a drag constant $b = 1.88 \times 10^{-6}$ N/(m/s) fits the exponentially decreasing velocity.	60
Figure 7.5: Part approach at different viscosities. Parts ($2000 \times 2000 \times 100 \mu\text{m}^3$) are highlighted by solid lines. The parts are accelerated towards the substrate by the magnetic field. The initial velocity of a part is 0. (a) 0.9557 mPa·s, (b) 0.6531 mPa·s and (c) 0.4668 mPa·s.....	62
Figure 7.6: Approach time vs. viscosity. The approach time increases proportionally to the viscosity. 95 % confidence intervals are indicated.....	62
Figure 7.7: Rotation time vs. the viscosity of water. (a) 90° rotation and (b) 180° rotation. The 95 % confidence intervals for the means are presented. 30 data are used at each viscosity.....	64
Figure 7.8: Trajectories of Ni patterns on wrongly oriented parts ($2000 \times 2000 \times 100 \mu\text{m}^3$) at air-water interface. Ni patterned parts in background shows their initial orientation. (a) 90° rotation. (b-d) 180° rotation.....	65
Figure 7.9: Assembly result without feedback. Higher yield is observed at lower viscosity. Row-level yield does not reach 100 % with 7 s of agitation. (a) substrate-level and (b) row-level yield.....	66
Figure 7.10: Assembly result with feedback. (a) substrate-level and (b) row-level yield. Higher yield is observed at lower viscosity. The row-level yield reach near 100 % with 20 s agitation.....	67
Figure 7.11: The dependence of assembly speed on the viscosity. The feedback control improves the assembly speed more effectively at lower viscosity.....	68

Figure 8.1: Assembly system. (a) Experimental setup for assembly consists of a water container on a linear electromagnetic shaker, a stepper motor with the controller, a substrate and parts floating at an air-water interface. (b) Design of parts and binding sites. Each part has six TSVs (diameter = 200 μm) and each binding site has six electrodes for electrical measurement.71

Figure 8.2: Assembly process. After assembly of each layer of parts, solder reflow process is needed for electrical and mechanical connection. 3D integration of multiple layers is achievable through a layer-by-layer assembly.72

Figure 8.3: Fabrication process flow for (a) the assembly template and (b) parts.74

Figure 8.4: Part with gap between parts. (Left) 6 Au TSVs (diameter = 200 μm) and a Ni pattern ($200 \times 200 \times 13 \mu\text{m}^3$) are patterned. (Right) Measured gap between parts is 22 μm . Part size is $2000 \times 2000 \times 100 \mu\text{m}^3$ 75

Figure 8.5: Simulated magnetic force decreases with increasing gap. The minimum magnetic force for successful assembly is 6.6 μN (at 0.99 mm). 13 μm thick Ni pattern is assumed. The total gap between a magnet and a Ni pattern on the 4th layer is 918 μm76

Figure 8.6: Assembly results. 4 layers of 2 mm sized parts are assembled on 2×2 binding sites.77

Figure 8.7: Distributions of measured resistance through (a) single TSV (Mean = 0.08 Ω , StDev = 0.012 Ω) and (b) 4 TSVs in series (Mean = 0.33 Ω , StDev = 0.051 Ω).77

Figure 9.1: Magnetic field of a single magnet. (a) Magnetic flux and its density [T] (cross-sectional view), (b) vertical components (top view) and (c) horizontal components (top view) of magnetic field at the surface of an assembly substrate [A/m].80

Figure 9.2: Design of binding sites and parts for the Pyramid. Dotted circles present magnets beneath an assembly substrate. (a) Bus shape. (b) Pyramid shape.81

Figure 9.3: Self-folding by magnetic field. Simulated magnetic flux is shown. (a) An assembled part with the water in-between kept in a trenched binding site. (b) Self-folding after drying out of the water.82

Figure 9.4: Folding angle control by shifting a magnet. To prevent the shift of the part with a magnet, the bottom of the part needs to be pinned by a hinge. (a) A standing part

(folding angle $\theta_f = 90^\circ$). (b) $\theta_f > 90^\circ$ and (c) $\theta_f < 90^\circ$ is achieved by horizontal shift of the magnet.	82
Figure 9.5: Folding angle control using additional magnet. The lower magnets act as a hinge to pin the parts. Simulated magnetic flux and test results. (a) A standing part (folding angle $\theta_f = 90^\circ$). (b) $\theta_f > 90^\circ$ and (c) $\theta_f < 90^\circ$ is achieved by additional magnets with opposite polarity.	83
Figure 9.6: Assembly of the Bus by horizontal shift of magnets. (a) After self-folding ($\theta_f \approx 90^\circ$). (b) A released structure after solder reflow.	84
Figure 9.7: Assembly of the Pyramid by horizontal shift of magnets. (a) After self-folding ($\theta_f \approx 90^\circ$). (b) Increased folding angle by shifting magnets. (c) The Pyramid shape before solder reflow. (d) A released structure after solder reflow.	84
Figure 10.1: Concentrated photovoltaic (CPV) cells. (a) Conventional PV cells reflect the incident light. (b) Proposed PV cells trap the incident light inside the pyramid shaped structure. The PV cells on the tilted parts can be removed and used as mirrors. (c-d) PV cell array.	88
Figure 10.2: A dog-shaped structure can be self-disassembled from an initial configuration of 27 suspended modules.	89
Figure 10.3: A 3D printing scheme for “W” shaped structure. (a) First layer writing. (b) Pull-up and cooling the first layer and second layer writing. (c) Final layer writing. (d) Completed structure.	90

LIST OF TABLES

Table 1.1: Selected Works in Millimeter-scale Self-assembly. (S: Shape matching, C: Capillary, V: Vibration, M: Magnetic field, A: Adhesive, I: Air-liquid, or liquid- liquid interface, W: Wet environment, D: Dry environment).....	2
Table 2.1: Design factors for screening test (assembly substrate).Three design were tested at various frequencies (35/45/55 Hz) and actuator output (1.5/1.75/2.0 g).....	8
Table 2.2: Design factors with levels. Nine substrate and nine agitation conditions make a total of 81 runs.	9
Table 2.3: Range and effect of four factors to assembly yield. Yield can be effectively improved by widening horizontal spacing rather than vertical spacing.....	10
Table 2.4: Design factors with levels. Four substrate and nine agitation conditions make a total of 36 runs.	11
Table 2.5: Result of analysis of variance. 82.8 % of total observed variation is due to the variation of the parameters.....	13
Table 3.1: Single angle assembly test result. The substrate tilting angle should be larger than the minimum α values to form line contact. The surface tension induced torque per area decreases as part size increases. The torque and torque per area are calculated based on the capillary torque model. This result indicates that the critical torque per unit area for successful assembly is between 0.048 and 0.071 $\mu\text{N/m}$	19
Table 3.2: Feedback assembly test result. The substrate tilting angles are changed from Table 3.1 after forming line contact. The surface tension induced torque per unit area for each part should be larger than its critical value (0.066 $\mu\text{N/m}$) for assembly. The torque and torque per unit area are calculated based on the model at the maximum substrate tilting angle.....	23
Table 4.1: Assembly results for different gaps and simulated magnetic force F_m (average, average ± 3 sigma) for the square patterned substrate. Yields are predicted using Monte-Carlo simulation (N = 4000) and F_m distribution. Critical magnetic force F_{mc}	

for successful assembly is estimated to be 6.4 μN based on the method of least squares.33

Table 4.2: Assembly results for different gaps and simulated magnetic force F_m for the stripe patterned substrate. Critical magnetic force F_{mc} is estimated to be 3.8 μN37

Table 4.3: Result of comparison (model vs. experiment). Part size and substrate design are considered. Model predicts the critical magnetic forces with error less than 3.9 %....38

Table 4.4: Design parameters and their contributions to assembly yield. Three design factors, each with two values, make eight combinations. Each run is repeated 30 times.....39

Table 4.5: Simulated magnetic forces on a part on a binding site (Part 1) and on a neighboring part (Part 2). Experimental assembly yields are also presented.....40

Table 7.1: Selected viscosities. The viscosity of water decreases to approximately half, as temperature increases from 22 to 60 °C. The temperature is controlled by a heating tape.....58

Table 7.2: Drag coefficients of water at different viscosities. The drag coefficients at 0.6592 and 0.4665 mPa·s are calculated using the experimentally obtained result at 0.9548 mPa·s.60

Table 7.3: Approach time ($d = 22$ mm) at different viscosities. Effective magnetic force $F_{m,eff}$ is calculated to be 4.63 μN at all viscosities. For statistical analysis, all experiments are repeated 30 times.61

Table 7.4: Summary of experimental results. 90° rotation time shows a clear linear dependence on viscosity while 180° rotation time does not. For statistical analysis, all experiments are repeated 30 times.63

Table 7.5: Selected results from each viscosity. 90° rotation time shows a clear dependence on the viscosity of water while 180° rotation time does not.....65

Table 7.6: Summary of the effect of the viscosity on yield with and without feedback. Lower viscosity increases assembly yield as well as assembly speed. 100 % yield is achieved with feedback control.68

ACKNOWLEDGMENTS

The writing of this dissertation has been one of the most significant challenge and accomplishment I have ever had to face. Without the generous support, patience and guidance of the following people, this study would not have been completed. It is to them than I owe my deepest gratitude.

- Professor Karl F. Böhringer who undertook to act as my supervisor and supporter during my studies despite his many other academic and professional commitments. His wisdom, knowledge and commitment to the highest standards inspired and motivated me.
- Members of MEMS group, especially Ji Hao Hoo and Cagdas Varel, who participated in this research project despite the enormous work pressures they were facing.
- Yun Kim and Steven Garmanian who supported and took care of my family. Thank you all from the bottom of my heart. You made my family feel at home.
- Hyunju Oh, my wife, who has always supported, encouraged and believed in me, in all my endeavors and who so loving and unselfishly cared for Jaewon and Jaeyoon. Her love, support and constant patience have taught me so much about sacrifice and compromise.
- Jaewon Park, my first son, who was born when I started my study and who always shows me his smile even when he was sick. He is my precious and his smile is the best part of my life.
- Jaeyoon Park, my second son, who was born just after my final exam and who smiled at me at his birth.

CHAPTER 1. INTRODUCTION

In biological systems, receptor-ligand, antigen-antibody, DNA-protein, sugar-lectin and RNA-ribosome interactions occur through non-covalent bonding such as hydrogen bonds, metal coordination, hydrophobic forces, van der Waals forces, π - π interactions, electrostatic and/or electromagnetic effects. These specific non-covalent interactions between two or more molecules are known as molecular recognition, which can be divided into static and dynamic categories. Static molecular recognition describes a one-to-one type reaction between a host and a guest molecule to form a host-guest complex; the specific recognition sites need to be prepared for specific guest molecules. In dynamic molecular recognition, the first guest to the first binding site of a host affects the association constant of a second guest with a second binding site. These diverse interactions have inspired and motivated modern research in self-assembly at the nano-to-millimeter scale [1, 2]. The self-assembly in this dissertation can be understood as an extension of static molecular recognition to the millimeter scale. The other types of molecular recognition suggest directions for research to achieve assembly of heterogeneous parts onto a common substrate and/or 3D stacking.

As the electronics industry nears the ultimate physical limits of historic CMOS scaling [3], prevailing growth driven by a continuous reduction in cost per function can no longer be sustained by scaling of transistor size alone. The assembly and packaging area is increasingly undertaking the responsibility of maintaining current growth rates, and it is doing so based on the principles of functional diversification and function densification. Functional enrichment, also known as “More-than-Moore” [4, 5] is a focus on system integration rather than transistor scaling. As an effort for cost reduction, 3D packaging is emerging by the demands of portable consumer products interacting with human and environment (such as AV player, GPS, smartphone, digital camera, etc.). A combination of multiple digital and non-digital components in a single unit known as system in package (SiP) can contain memory, logic devices, active/passive MEMS, optical components and other devices and thus has multiple functions. There are 2D (horizontal) and 3D (stacked and embedded) SiP structures. Compared to 2D packaging, 3D integration provides higher performance, lower power consumption, smaller area and lower cost. 3D packaging becomes important in numerous industrial areas where miniaturization trends increase the need for high integration density (number of assembled parts per unit space) and fitting of components in small design spaces. It can benefit security, healthcare industry, alternative energy and intelligent cars with fuel economy and driving safety [6]. To increase the effectiveness of 3D integration, thinner components are desired.

Table 1.1: Selected Works in Millimeter-scale Self-assembly. (S: Shape matching, C: Capillary, V: Vibration, M: Magnetic field, A: Adhesive, I: Air-liquid, or liquid- liquid interface, W: Wet environment, D: Dry environment)

No.	Company / University	Assembly method	Part size		l/Aspect ratio	3D Integration density [a.u.]	Specific orientation	Yield [%]
			Lateral dimension [μm]	Thickness [μm]				
1	IME [7] (Singapore)	V, M, D	1000	200-500	2.0-5.0	0.188	No	97
2	Stanford [8]	C, A, W	400	15-50	8.0-26.7	0.458	No	100
3	UW [9]	S, A, W	100 ^C	10-20	5-10	0.062	Yes	97
4	UMN [10]	A, I(L/L), W	20	10	2	0.004	No	98
5	Harvard [11]	C, V, A, W	300	400	0.75	0.023	No	98
6	UFL [12]	V, M, A, W	1000	500	2	0.413	Yes	99
7	UW [13]	V, D	1270	200	6.35	0.599	Yes	100
8	UW [14]	V, D	790	330	2.39	0.484	No	99.8
9	UW [15]	V, D	370	150	2.47	0.301	No	100
10	UW [16]	C, V, I (A/L), W	1000-2000	100	10-20	4.127	No	100
11	UW [17]	C, V, M, I (A/L), W	2000	100	20	6.603	Yes	100

For these reasons, many research groups have studied self-assembly systems, which employ various driving forces such as gravity [9], surface tension [11, 18, 19], electrostatic [20] or electromagnetic force [10, 21, 22] and often require adhesives, liquid solder, shape matching structures or two different liquids [10]. They, however, have lower yield compared to the pick-and-place assembly due to their stochastic nature [23]. Various self-assembly methods using capillary reactions for the capture and self-alignment are investigated, as well as template-based self-assembly in dry and wet environment. Table 1.1 summarizes selected works in millimeter-scale self-assembly. It is evident that the last two instances (item 10 and 11) have higher aspect ratio and high packing density with unique orientation among all self-assembly methods. Previous works in micro-to-millimeter scale self-assembly [7-16] in Table 1.1 are plotted against key parameters in Figure 1.1, accompanied by the work described in this

dissertation (triangular and circular marker). High 3D integration density (number of assembled parts per unit space) is achieved by high 2D integration density and low aspect ratio.

The ability to assemble parts from different processes in a unique orientation is important for maximal area efficiency in circuit and component design as well as flexibility in the types of devices that can be fabricated. It also contributes towards improving functional diversification and function densification (More-than-Moore [4, 5]). Here, we present a novel fluidic self-assembly (FSA) method supported by numerical and statistical analysis to achieve high-yield orientation-specific self-assembly of millimeter-scale thin silicon parts from an air-water interface. Surface functionalized thin silicon parts ($2000 \times 2000 \times 100$, $4000 \times 4000 \times 100 \mu\text{m}^3$) are assembled in preprogrammed hydrophilic binding sites on a substrate with self-alignment and unique orientation assisted by a magnetic field.

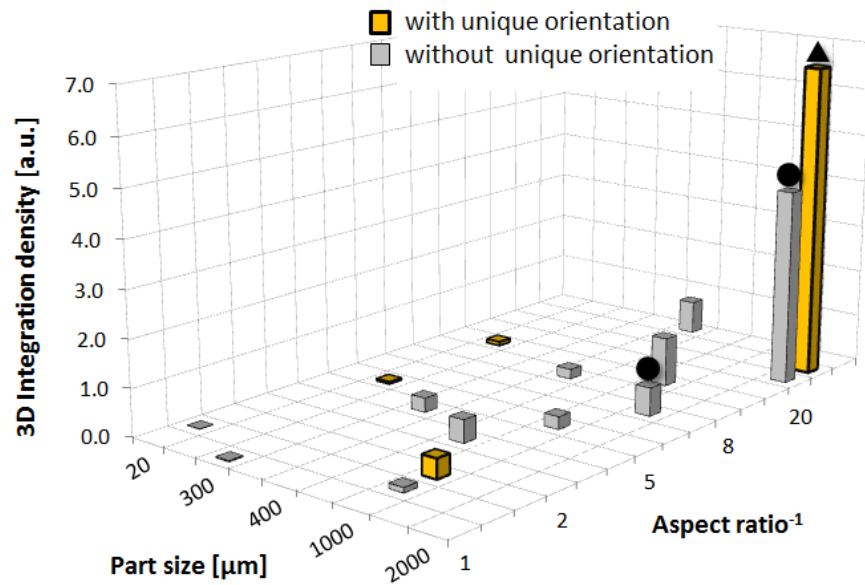


Figure 1.1: Part size and relative 3D integration density of selected works in micro-scale self-assembly. The latest work (triangular marker) achieves high 3D integration density using thin (low aspect ratio) parts. The circular markers indicate self-assembly without control over orientation. The average of 3D integration density of selected works is 1.

Unlike other liquid solder-based self-assembly, the proposed FSA system uses water-based capillary action and magnetic fields as driving mechanism. In liquid solder-based assembly, volume loss and a change in the solder composition occur over time due to a continuous re-oxidation and oxide removal process, which limits the total assembly time and simplicity of the

assembly system. Moreover, the temperature should be maintained constant and the pH of the assembly solution needs to be controlled to prevent surface oxide on the metal and the solder surface [10, 24]. In contrast, the proposed FSA system is simple and more robust to assembly time, temperature and pH, because there is no source that changes the composition of the medium over time and the system uses the hydrophilic oxide surfaces for assembly.

This dissertation focuses on a novel method to achieve high yield assembly of millimeter-scale thin silicon parts from an air-water interface. The first proposed assembly method without control over orientation is improved to be able to assemble parts (square, circular, rectangular) in unique orientation. It is further improved to be able to distinguish desired parts from an unsorted collection of many different parts. In addition, the effects of the fluid viscosity and feedback control are experimentally and analytically studied. Finally, the 2D fluidic self-assembly is extended to realize 3D integration and 3D structures (3D origami).

Chapter 2 introduces a novel FSA [16, 25, 26] at the air–water interface and demonstrates high yield using specific surface Faraday waves [27, 28], which achieve a selective assembly to programmed sites from an excess part supply. Well-known statistic methods such as DOE (Design of Experiment), ANOVA (Analysis of Variances) and RSM (Response Surface Method) are employed from system design to analysis. All experiments and analysis based on statistics produce highly reliable and reproducible results with minimum effort.

Chapter 3 details a comprehensive model and experimental support that extends the applicability of the assembly method to a wide range of part sizes and designs. Here, the focus is on the combined effect of substrate tilting angle and part size. Experimental results and surface tension induced torques calculated based on a newly developed model reveal that there is a limit on the lateral part size when we use a constant substrate tilting angle. Based on the analysis, a novel method to overcome the size limit on assemblable parts by parametric change in substrate tilting angle is proposed.

Chapter 4 introduces a novel method supported by numerical and statistical analysis to achieve orientation-specific FSA of millimeter-scale thin silicon parts from an air-water interface. Surface functionalized silicon parts ($2000 \times 2000 \times 100 \mu\text{m}^3$) are assembled in preprogrammed hydrophilic locations on a substrate with self-alignment and unique orientation by a magnetic field. From test and additional simulations, a guideline for the assembly system design is suggested.

Chapter 5 presents a novel methodology for the orientation-specific parallel heterogeneous integration of parts of various sizes. Assembly sites are designed to only attract specific parts from an unsorted pool using the combined effect of Faraday waves and magnetic forces,

achieving one-to-one, part-to-site registration. We demonstrate FSA of two types of thin parts ($2000 \times 2000 \times 100$ and $4000 \times 4000 \times 100 \mu\text{m}^3$) onto the same substrate through a one-step process. Statistical analysis of the distributions of magnetic forces delimits the suitable range for strength of Faraday waves to fix non-optimal initial placements and orientations.

Chapter 6 presents an analytical work performed to minimize the rotation angle of self-assembled thin circular parts (diameter = 2 mm, thickness = $100 \mu\text{m}$). Large deviation of rotation angle of parts is analyzed and improved by optimizing magnet position. 90 parts are assembled row-by-row in one minute. Compared with FSA of square parts, assembly speed is increased due to reduced part-to-part interaction.

Chapter 7 details the effect of fluid viscosity on FSA at an air-water interface through experimental and analytical approaches. The assembly method is subdivided into three process steps (approach, rotation, pull-up) and their viscosity dependency is investigated. The motion of a moving part is described using a derived modeling equation. High yields at different viscosities are demonstrated using thin square parts ($2000 \times 2000 \times 100 \mu\text{m}^3$). Near 100 % yield can be achieved by adding visual feedback control for the application of Faraday waves. The combined effect of the application time and the fluid viscosity is analyzed.

Chapter 8 is presents the first proof-of-concept 3D integration using self-assembly of chip-scale parts ($100 \mu\text{m}$ thickness). 3D integration is achieved by assembling new parts over previously assembled parts. Assembly proceeds as an assembly substrate is pulled up through an air-water interface and electrical and mechanical bonding is achieved through a solder reflow process. Magnetic fields and temporary Faraday waves are introduced for one-to-one part-to-site registration in proper orientation. The maximum number of layers that can be achieved is simulated and analyzed. Via resistance including the effect of degradation of solder over repeated reflow process is measured.

Chapter 9 presents a novel self-assembly of 3D structures by controlling the folding angle through the analysis of the magnetic field. As a proof of concept, millimeter-scale pyramid shaped structure with a folding angle $> 90^\circ$ is fabricated.

Chapter 10 summarizes the work done thus far, and also details potential future works.

CHAPTER 2. FLUIDIC SELF-ASSEMBLY OF MILLIMETER SCALE THIN PARTS AT AIR-WATER INTERFACE

2.1 Introduction

The system consists of a water container on a linear electromagnetic vertical vibration table and a dip coater, substrate and parts floating at an air-water interface (Figure 2.1). The measured acceleration uniformity over the vibration table is 0.72 %. This is measured using a laser vibrometer (Polytec OFV-534 laser unit and OFV-2500 vibrometer controller) and the difference between maximum and minimum acceleration is only 20 mg when driven at 80 Hz / 1.4 g.

The substrate can be tilted at any angle with the water surface and pulled up vertically by the dip coater. This angle is optimized for highest yield using experimental data and analytical models to be discussed later in this dissertation. During substrate pull-up, the parts approach the substrate due to the meniscus formed by the hydrophobic (SAM: self-assembled monolayer-coated Au) / hydrophilic (oxide) patterns on the substrate and become assembled (Figure 2.2). Specific surface waves are applied to prevent multiple parts from approaching one site and to achieve one-on-one part-to-site registration. According to [29], the contact angle between tilted substrate and water depends on speed of pull-out. However, the shape of the meniscus is time-independent for small pull-out speed [30]. Therefore we can ignore the effect of the speed for all substrate tilting angles and assume the system is quasi-static in modeling and analysis in the following sections.

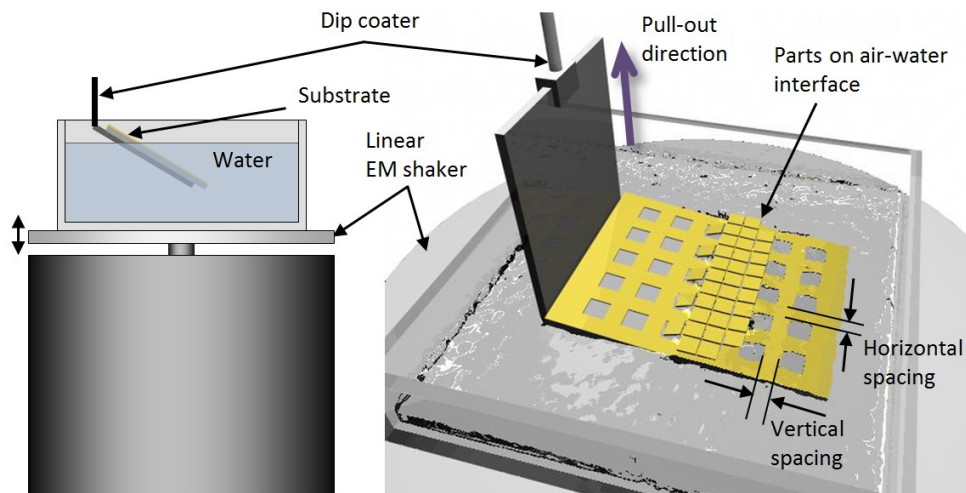


Figure 2.1: The experimental setup consists of a water container, linear electromagnetic vibration table, dip coater, substrate and parts floating at air-water interface.

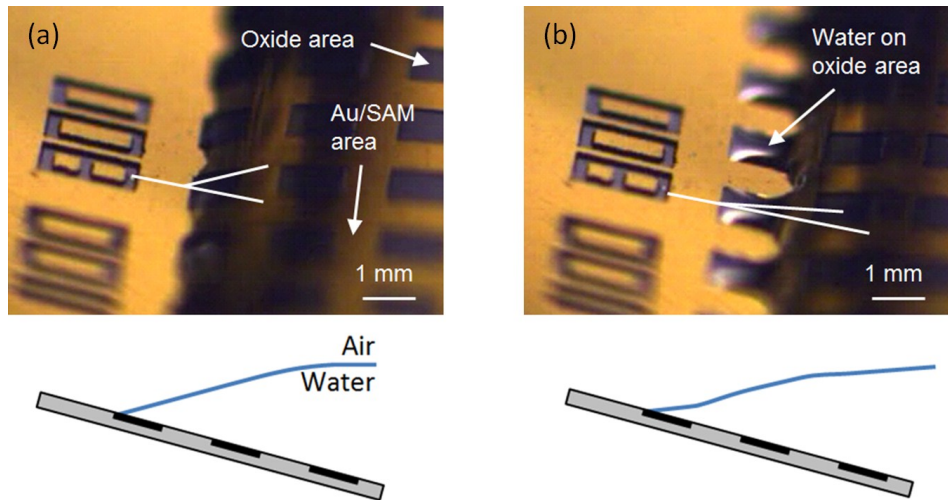


Figure 2.2: Contact angle change during pull-up. Parts will be assembled on the oxide area with a thin water layer. (a) High contact angle for the approach of part. (b) Water remains on the oxide area for assembly.

2.2 Fabrication

The substrate is fabricated from a 4 inch silicon wafer coated with Cr (10 nm) and Au (100 nm) by electron beam evaporation. The wafer is spin coated with AZ4620 resist followed by photolithography to define the square patterns. The exposed Au and Cr layers are removed subsequently using wet etching. A standard Bosch DRIE (deep reactive ion etching) process is used to etch the exposed silicon sites to approximately 70 μm depth. After photoresist removal, the patterned substrate is cleaned in oxygen plasma and then soaked in a solution of 1 mM dodecanethiol in ethanol overnight. A thiol SAM selectively attaches to the gold surface and makes them hydrophobic [31]. In this experiment, the purpose of the SAM layer is to increase the wettability contrast between the Au/SAM background area and oxide binding sites. The wafer substrate is then diced into several pieces for assembly tests.

Fabrication of parts is achieved by standard photolithography, Cr/Au evaporation, wet-etch and dry-etch steps on the front side of the SOI wafer. Dry-etching exposes the buried oxide layer and HF etching releases the parts. Then individual parts are stored in ethanol solution.

The silicon oxide layer on the substrate and parts serves as a passivation layer and ion absorption is minimized using deionized water. The Au coated side is treated with SAM that renders the surface hydrophobic. The SAM formed from thiols on gold is stable for days to weeks [32] while the assembly process takes less than few minutes. Thus, high wettability contrast is maintained until the assembly is completed.

2.3 Parameter selection through screening test

To investigate the factors that influence assembly, nine substrates with different spatial patterns (Table 2.1) are tested at various frequencies (35/45/55 Hz) and actuator output (1.5/1.75/2.0 g). In this preliminary experiment, the angle between the substrate and water surface is 10° and pull-up speed is 1 mm/min. In this range, only Substrate#1 with wider spacing between hydrophilic sites has selective assembly and the highest yield (45 %) at 55 Hz / 1.5 g. The other substrates do not show any selective assembly because narrow spacing does not produce distinct stick-slip motion. From this result, horizontal/vertical spacing, and agitation condition are set as important factors in the experiment.

Table 2.1: Design factors for screening test (assembly substrate). Three designs were tested at various frequencies (35/45/55 Hz) and actuator output (1.5/1.75/2.0 g).

Substrate	Si area	Horizontal spacing	Vertical spacing
#1		1.1 mm	1.8 mm
#2	1.2×1.2 mm ²	0.8 mm	0.2 mm
#3		mm	0.8 mm

2.4 Parameter analysis

To analyze the effect of these factors, we use the levels in Table 2.2 and select full factorial design in fully randomized order to minimize unexpected bias. Based on the previous experiment, horizontal / vertical spacing is determined to be larger than 200 μm to achieve selective assembly. However, a design with 500 μm spacing exhibits no selective assembly and all designs with 35 Hz agitation achieve no assembly. Therefore, 500 μm and 35 Hz are not presented in the analysis.

To measure the contribution of each factor to yield, these experimental data are analyzed. In the effect analysis result in Figure 2.3, the x-axis for each graph presents the factor levels and the y-axis indicates yield. The higher the slope, the larger is the effect on yield. Horizontal spacing has a larger effect than that of vertical spacing. High frequency (55 Hz) and low acceleration (1.5 g) leads to optimum agitation condition. The results (Table 2.3, Figure 2.3 and Figure 2.4) show that the yield can be effectively improved by widening horizontal spacing rather than vertical spacing. The contour plots for each substrate in Figure 2.4 show the same trend that higher frequency and lower acceleration will produce higher yield. Further experimental conditions for optimization, frequency and acceleration range are determined based on contour plots.

Table 2.2: Design factors with levels. Nine substrate and nine agitation conditions make a total of 81 runs.

Factor	Level
Substrate	
Horizontal spacing	500 / 800 / 1100 μm
Vertical spacing	500 / 800 / 1100 μm
Agitation	
Frequency	35 / 45 / 55 Hz
Acceleration	1.50 / 1.75 / 2.00 g

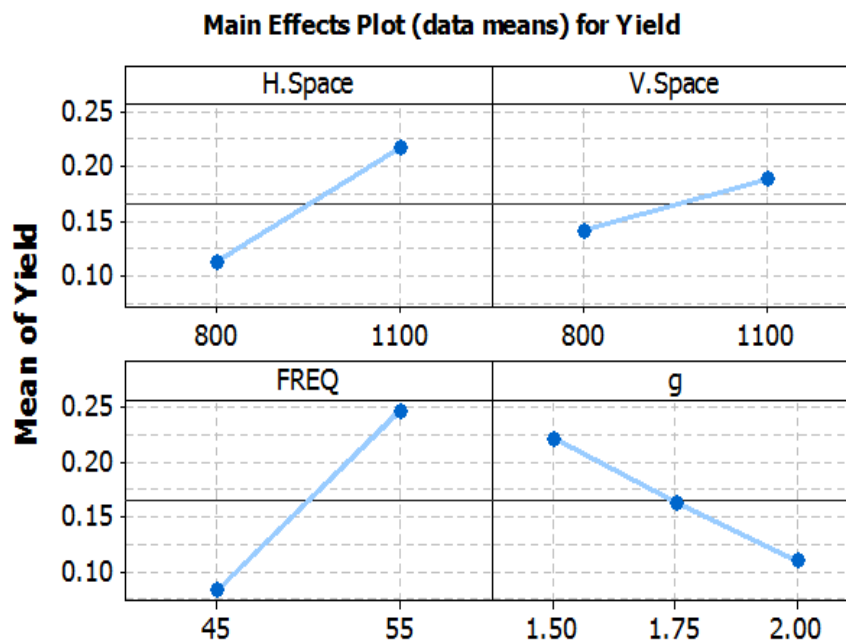
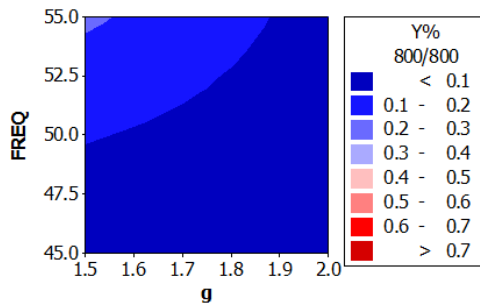


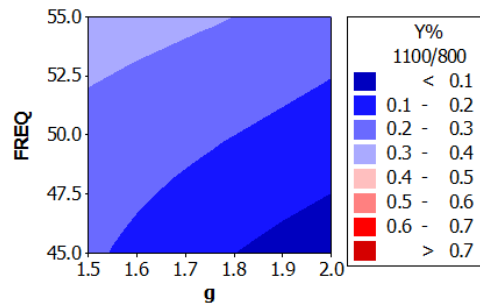
Figure 2.3: Effect with slope of four factors to assembly yield. X-axis presents the factor levels and Y-axis indicates yield.

Table 2.3: Range and effect of four factors to assembly yield. Yield can be effectively improved by widening horizontal spacing rather than vertical spacing.

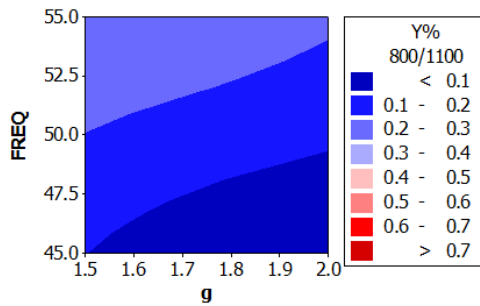
Factor	Range	Effective yield change
Substrate		
Horizontal spacing	800/1100 μm	10.4 %
Vertical spacing	800/1100 μm	4.6 %
Substrate		
Frequency	45 / 55 Hz	16.4 %
Acceleration	1.50/1.75/2.00 g	11.3 %



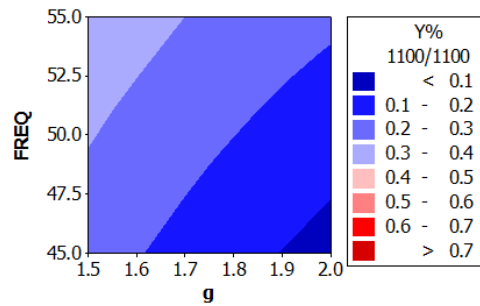
(a) 800(H) \times 800(V)



(b) 1100(H) \times 800(V)



(c) 800(H) \times 1100(V)



(d) 1100(H) \times 1100(V)

Figure 2.4: Contour plots of assembly yield versus agitation frequency (x-axis) and amplitude (y-axis) for four substrate designs in Table 2.3.

2.5 Optimization and 100 % assembly

From the analysis result in Figure 2.3 and Figure 2.4, the optimum agitation condition seems to be in the left upper region of the contour plots. Therefore, to find the optimal agitation condition, full factorial design with four parameters in Table 2.4 is used. Again, we employ Design of Experiment methodology to find an optimal space for high yield.

As shown in Figure 2.5, different designs have the maximum yield at the agitation condition (~ 80 Hz, 1.4 g). However, complete assembly is not observed and this low yield is noted due to the lack of control of one-on-one part-to-site registration. We avoid multiple parts approaching one binding site by use of surface waves. This assembly has the highest yield when parts in Figure 2.6(b) are rearranged by agitation so that only one part faces one binding site as shown in Figure 2.6(c). The misaligned parts can be aligned through the energy minimization process during agitation. Even if two parts occupy one binding site, only one part with higher capillary force will remain after applying agitation. The agitation time without pulling up the substrate is around 20 s on average. The statistical analysis of the minimum agitation time for this rearrangement using MinitabTM indicates that longer agitation produces higher probability of rearrangement and 50 s agitation has 100 % probability of appropriate arrangement.

Table 2.4: Design factors with levels. Four substrate and nine agitation conditions make a total of 36 runs.

Factor	Level
Substrate	
Horizontal spacing	800 / 1100 μm
Vertical spacing	800 / 1100 μm
Agitation	
Frequency	65 / 80 / 95 Hz
Acceleration	1.0 / 1.5 / 2.0 g

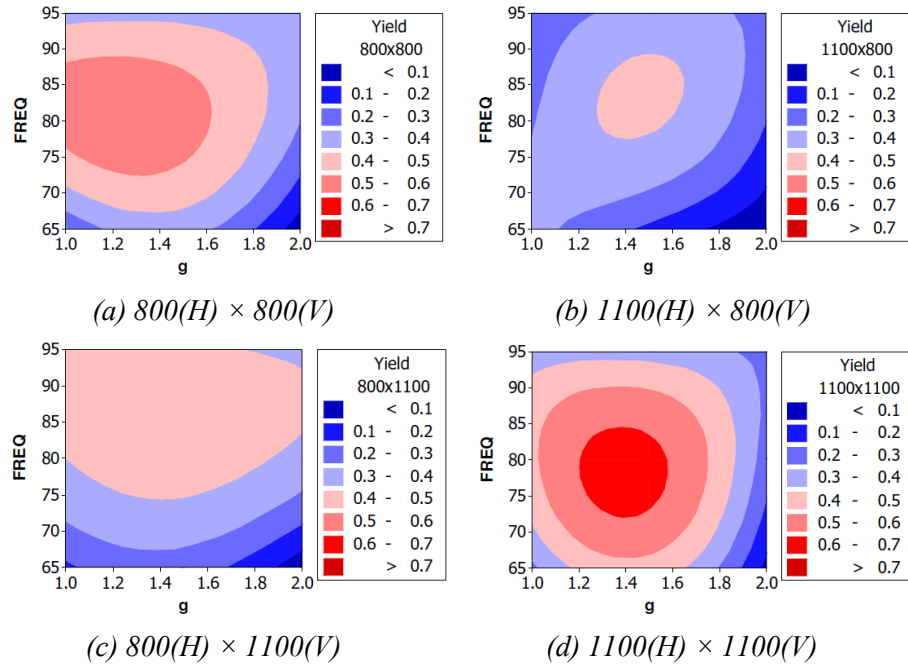


Figure 2.5: Contour plots of assembly yield versus agitation frequency (x-axis) and amplitude (y-axis) for four substrate designs in Table 2.4.

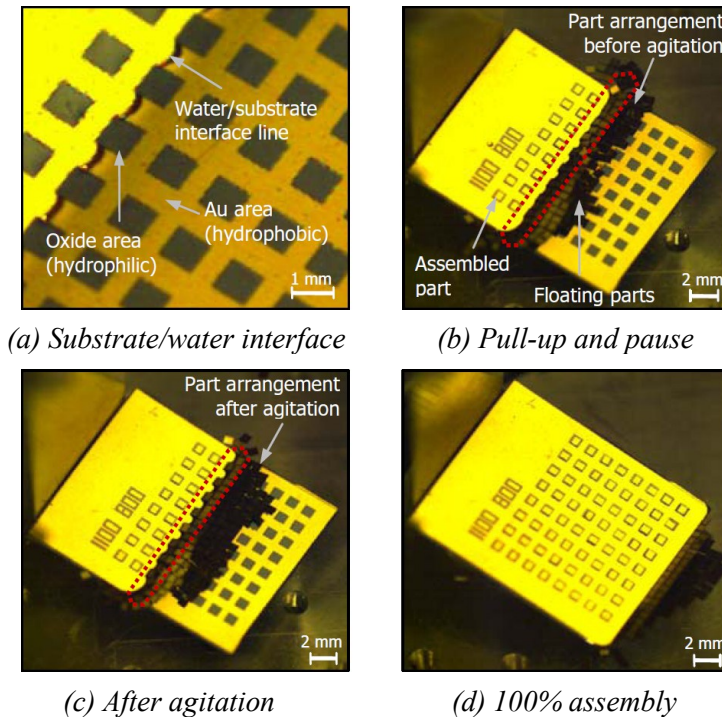


Figure 2.6: Parts ($1 \times 1 \text{ mm}^2$ parts with $100 \mu\text{m}$ thickness) rearrangement by agitation. The dark squares are the hydrophilic sites and the gold regions are the hydrophobic surfaces. (a) Substrate/water interface. (b) Pull-up and pause. (c) After agitation. (d) 100% assembly.

To verify the reliability of the experimental data, a method called ANOVA (analysis of variance) is used. In an ANOVA test, total observed variance (SS_T) is partitioned into two components: the treatment sum of squares (SS_{TR}) and the error sum of square (SS_E) depending on the explainability. This relationship can be written as

$$SS_T = SS_{TR} + SS_E \quad (2.1)$$

According to the ANOVA result in Table 2.5, SS_{TR} which is explainable forms 82.8 % of total observed variation (SS_T) and is due to the variation of the parameters. The portion of error (SS_E) which is unexplainable is only 17.2 % of the total variation. This error can be caused by uncontrollable factors in the experiment such as repetition, measurement, shaker frequency / amplitude variation and different part distribution on the air-water interface. This analysis assures the reliability of the experiment. In addition, the formula for the one-way ANOVA F-test statistic is

$$F = \frac{MS_{TR}}{MS_E} \quad (2.2)$$

Table 2.5: Result of analysis of variance. 82.8 % of total observed variation is due to the variation of the parameters.

Source of Variation	Sum of Squares	Degrees of Freedom	Mean Squares	F
Parameters	2.06138	31	0.06650	11.77
Error	0.42936	76	0.00565	
Total	2.49074	107		

Here, the mean squares (MS_{TR} and MS_E) are quantities computed by dividing the sum of squares by its number of degrees of freedom. This equation indicates the ratio of explainable variance and unexplainable variance. By comparing the components of the total variation, the statistical significance of treatment is tested. The critical F value is the number that the test statistic must exceed to reject the test and it is determined by the significance level, the number of groups to compare and the degrees of freedom. In the experiment, the critical F value is 4.17 at $\alpha = 0.05$. Since $F = 11.77 > 4.17$, the effect of parameters is proved to be significant at 5 % significance level.

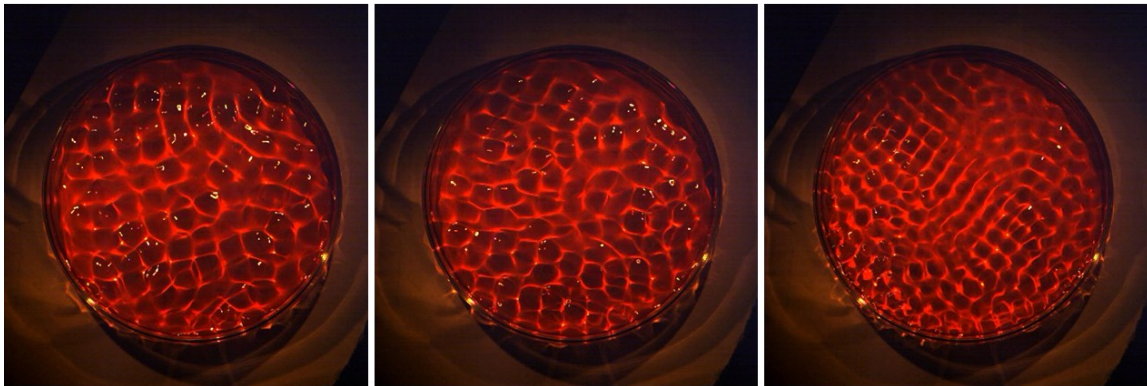
Based on this result, 100 % yield (Figure 2.6(d)) can be achieved by repeating the following three

steps for each row: (i) pull-up without agitation and pause and (ii) agitation (~ 80 Hz/1.4 g), until one-to-one part-to-site registration is achieved, and (iii) pull-up for assembly. Once the parts are registered on binding sites, they can be successfully assembled.

2.6 Effect of Faraday waves

Typical yield loss in FSA is due to lack of control of one-on-one part to site registration. In the proposed method, the parts are restricted to a surface layer and hence many are available for assembly. We avoid multiple parts approaching a site by use of surface waves. Based on the experimental data, we hypothesize that the actuator temporal frequency dependent Faraday wave spatial frequency is a critical factor that affects selective assembly. This addition of surface Faraday waves is a critical new component in the assembly process design compared with previous FSAs.

To investigate the effect of Faraday waves on parts rearrangement, frequencies from 50 to 100 Hz are applied to form Faraday waves (Figure 2.7). For a frequency range from 50 to 100 Hz, the wave numbers k are calculated using the equations in [27, 28] and compared to theoretical values in Figure 2.8. At the optimal frequency of this FSA system, the wave length of surface Faraday wave is 6.9 mm. Besides one-to-one part-to-substrate registration which enables 100 % yield (Figure 2.6), Faraday waves also help parts approach to a substrate. The simulation result in Figure 2.9 shows that Faraday waves accelerate part approach to the substrate.



(a) 50 Hz

(b) 75 Hz

(c) 100 Hz

Figure 2.7: Faraday wave vs. applied frequency. As frequency increases shorter wavelength (higher k) is observed.

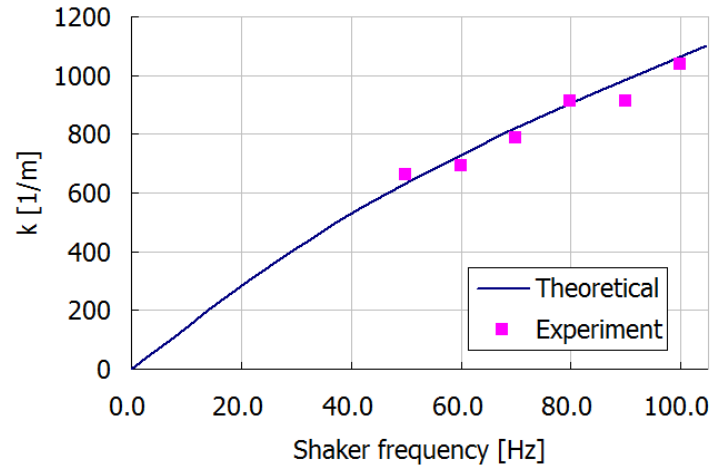
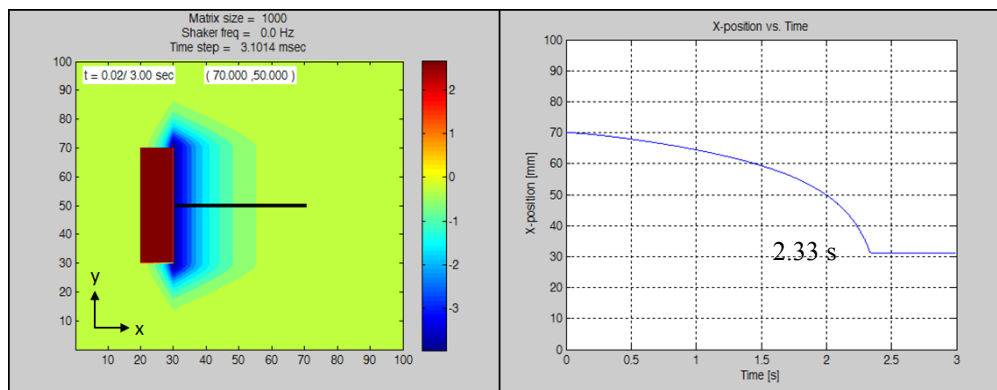
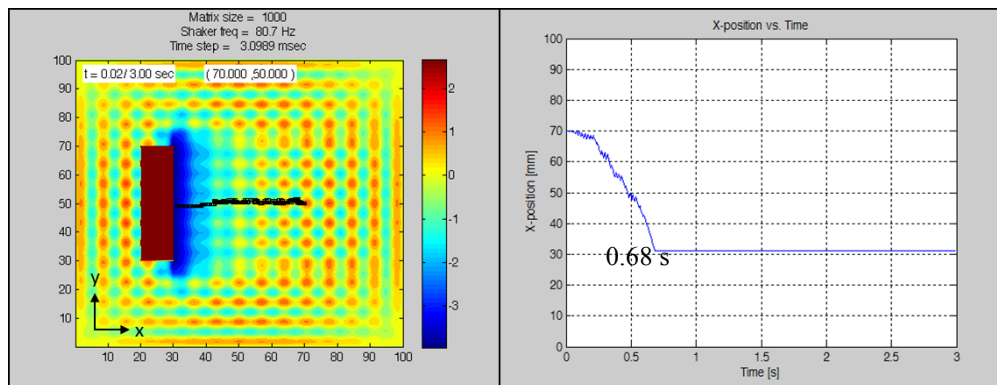


Figure 2.8: Comparison of k values. Theoretical and experimental values are compared.



(a) Part motion without Faraday waves



(b) Part motion with Faraday waves

Figure 2.9: Simulated motion of a part ($1000 \times 1000 \times 100 \mu\text{m}^3$) at air-water interface. The initial position of a part is (70, 50) mm and vertical agitation with 80 Hz / 1.4 g is applied. Color indicates the surface level.

2.7 Conclusion

A novel fluidic self-assembly using air-water interface is developed. Four parameters (horizontal and vertical spacing, frequency, acceleration) are selected by screening test and optimized through design of experiment (DOE) method with effect analysis. Surface Faraday waves are introduced to achieve more selective assembly by one-to-one part-to-binding site rearrangement. In addition, 100 % assembly is demonstrated by applying Faraday waves.

CHAPTER 3. MECHANICS AND SCALING OF SELF-ASSEMBLY OF THIN PARTS AT AIR-WATER INTERFACE

3.1 Introduction

In Chapter 2, we introduced a novel FSA at the air–water interface and demonstrated high yield using specific surface Faraday waves, which achieves a selective assembly to programmed binding sites from an excess part supply. It was accomplished for a small range of part sizes and substrate designs. In this chapter, we present a comprehensive model and experimental support that extends the applicability of the assembly method to a wide range of part sizes and designs. Guided by analysis, we also alter the assembly mechanism to include time-dependent parametric changes in the substrate tilting angle.

3.2 Part size scaling

Assembly tests for various part sizes (1×1 , 3×3 and 5×5 mm² parts with 100 μm thickness) on corresponding templates show that a larger part needs a smaller substrate tilting angle α . This is because large parts need a less steep meniscus near the substrate to approach. In addition, a smaller substrate tilting angle helps to increase the capillary torque. The capillary torque will be discussed in the next section using the proposed assembly model.

The meniscus convexity change in response to the substrate tilting angle α (Figure 3.1) is experimentally studied. In addition, the effect of substrate tilting angle on part approach is demonstrated and discussed using 3×3 mm² parts with different substrate tilting angles α (40°, 56°).

The behavior of meniscus convexity is described using θ^* in Figure 3.1. This relationship is known as Young’s equation and establishes the basic mechanism of a refractive tilting-plate technique for measurement of dynamic contact angles [33]. The meniscus becomes flat at a critical angle α_c , which is the critical condition for parts to approach the substrate. For substrate tilting angles larger than α_c , the parts do not approach the substrate and there is no assembly. The shape of the meniscus changes when the plate tilts at different angles. This is a consequence of Young’s equation, which states that the contact angle θ remains constant. From Figure 3.1, the meniscus convexity θ^* is defined by Equation (3.1) where α is the plate tilting angle and θ is the contact angle between the substrate and water:

$$\theta^* = \theta + 90^\circ - \alpha \quad (3.1)$$

The meniscus convexity changes with respect to the substrate tilting angle α . Equation (3.1) indicates that the meniscus convexity θ^* can be manipulated by controlling the substrate tilting angle α as shown in Figure 3.1.

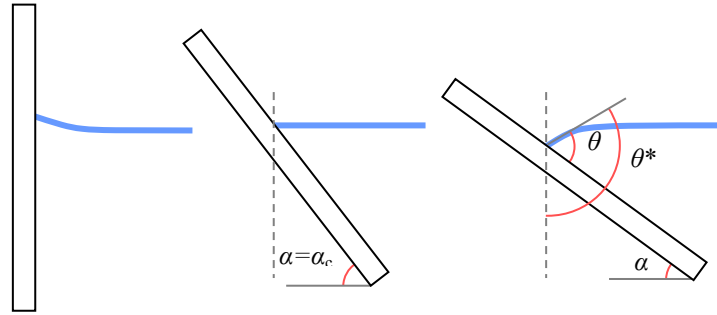


Figure 3.1: Behavior of meniscus convexity at various substrate tilting angles. The shape of the meniscus changes depending on the substrate tilting angle.

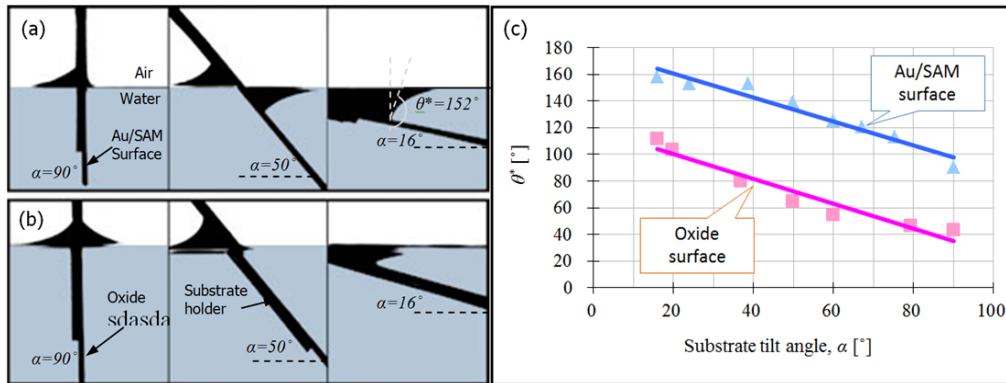


Figure 3.2: The behavior of meniscus convexity θ^* at various substrate tilting angles. (a) Experimental result of meniscus convexity response to substrate tilting angle for the Au/SAM surface. (b) Experimental result of meniscus convexity response to substrate tilting angle for the oxide surface. (c) Image analysis result for (a) and (b). The slope near the substrate has a linear relationship with the substrate tilting angle α and keeps the constant difference between hydrophobic (Au/SAM) and hydrophilic (oxide) surfaces.

Figure 3.2 shows the experimental result of meniscus convexity for Au/SAM and oxide surfaces at eight different tilting angles from 16° to 90°. For each angle, meniscus convexity values are obtained through image processing. The Au/SAM surface has a larger θ^* than that of the oxide surface due to its lower surface wettability.

When the substrate tilting angle α decreases, the meniscus convexity changes, which increases θ^* . Thus, θ^* for Au/SAM and oxide surfaces maintain a constant difference of 62° in the range of α from 10° to 90°. Although it seems to be more advantageous to have a larger θ^* for the part approach because it forms a steeper slope, there is an upper limit on θ^* . A steep slope near the substrate prevents the part approach because the part keeps aligned with the water surface as

shown in Figure 3.3.

A smoother change of the slope is required for a larger part. Figure 3.3 shows test results for two α values. While larger θ^* (steeper slope) is obtained at α of 40° , the part approaches the substrate at α of 56° , which is because of smoother meniscus curvature.

Thus we can experimentally obtain the maximum α for each part size in Table 3.1 and the capillary torques can be calculated based on the developed model described in the next section. The substrate tilting angle should be larger than the minimum α values to form line contact. The surface tension induced torque per unit area decreases as part size increases. The results in Table 3.1 indicate that the torque per unit area for assembly lies between 0.048 and 0.071 $\mu\text{N/m}$.

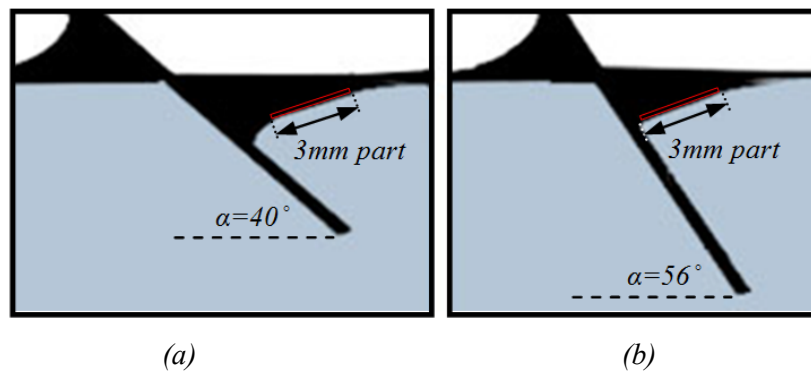


Figure 3.3: Part approaching the substrate. The part size is $3000 \times 3000 \times 100 \mu\text{m}^3$. (a) Abrupt change of meniscus slope prevents the part approach. (b) Low convexity helps part approach.

Table 3.1: Single angle assembly test result. The substrate tilting angle should be larger than the minimum α values to form line contact. The surface tension induced torque per area decreases as part size increases. The torque and torque per area are calculated based on the capillary torque model. This result indicates that the critical torque per unit area for successful assembly is between 0.048 and 0.071 $\mu\text{N/m}$.

Part size, $L \times L$ [mm^2]	Part volume [mm^3]	Minimum α [$^\circ$]	Torque, T [μNm]	T per unit area [$\mu\text{N/m}$]	Assembly
1×1	0.1	< 10	> 0.07	> 0.071	Yes
3×3	0.9	48.2	0.43	0.048	No
5×5	2.5	72.1	0.72	0.022	No

3.3 Assembly model

In FSA, the parts go through three steps before successful assembly (Figure 3.4). Parts at the air-water interface approach the substrate and make line contact if the meniscus is smooth enough for parts to approach in step (a). As the substrate is pulled up, the meniscus convexity changes from downward to upward due to surface tension of the water and hydrophilic property of the binding site. During transition from (b) to (c) in Figure 3.4, the part at the substrate-water interface rotates by an angle α , which induces the capillary torque. Thus the capillary torque between parts and binding site plays a decisive role in the assembly process.

The ratio of body forces to surface tension forces can be expressed using the dimensionless bond number $Bo = \rho a L_c^2 / \gamma$ with ρ being the density of water, a the acceleration which is gravity, L_c the characteristic length scale and γ the surface tension of the water. The bond numbers for different angles with different parts are less than 1, thus the surface tension dominates during the transition from Figure 3.4(b) to (c) and the gravitational force is neglected.

For the part on the binding site, if the capillary torque during transition from Figure 3.4(b) to (c) is not large enough to overcome the gravitational force due to an upward bending meniscus near the substrate, the part will be repelled away, which results in assembly failure.

To calculate the capillary torque between the part and binding site at the assembly step shown in Figure 3.4(b), the geometry including the part at the air-water interface and binding site is depicted in Figure 3.5. The system has three phases (S : solid, L : liquid, V : vapor) and three interfaces (SL : solid-liquid, SV : solid-vapor, LV : liquid-vapor) which result in the total energy W_{TOT} . For equations (3.2)-(3.6), surface tensions for both part and binding sites are the same ($\gamma_{SL1} = \gamma_{SL2} = \gamma$) and part size and binding site size are $L_1 \times L_1$ and $L_2 \times L_2$, respectively, where $L_1 \approx L_2 \approx L$. The energy between oxide and air, W_{SV} can be ignored because the entire oxide area is covered by liquid.

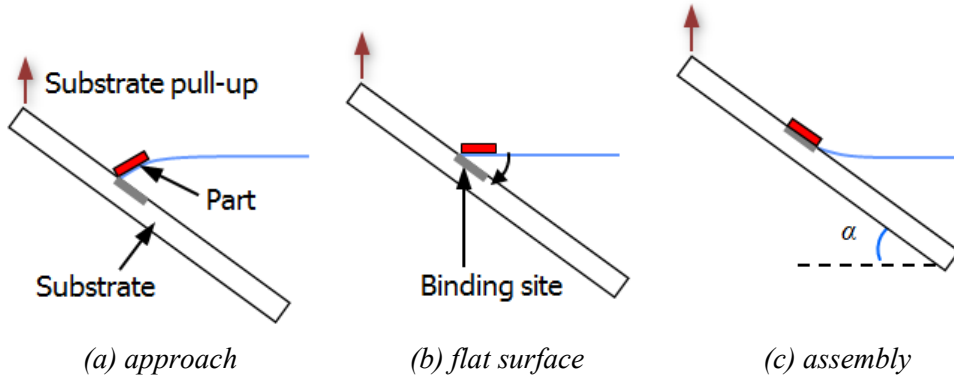
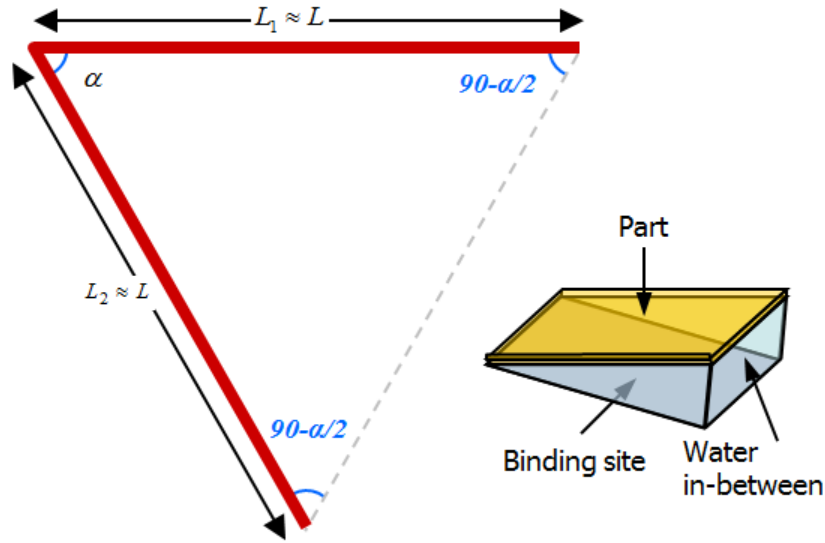


Figure 3.4: For successful assembly, the parts go through three steps: approach, flat surface and assembly.



γ_{SL1} : oxide side of the part – water interface

γ_{SL2} : binding site - water interface

γ_{LV} : air - water interface (modeled as a triangular shape)

Figure 3.5: Diagram for the simplified capillary torque model. Horizontal and inclined solid lines indicate the bottom oxide side of the part floating at the air-water interface and the oxide binding site under the water, respectively.

Although parts can assemble on Au/SAM area (Figure 2.6(b)), they have relatively small capillary forces due to low wettability. Thus these parts can be easily repelled away with the help of the Faraday waves and one-on-one part-to-site registration can be achieved (Figure 2.6(c)).

$$W_{SL} = \gamma_{SL1}L_1^2 + \gamma_{SL2}L_2^2 \approx 2\gamma_{SL}L^2 \quad (3.2)$$

$$W_{SV} \approx 0 \quad (3.3)$$

$$W_{LV} = 2\gamma_{LV}\frac{1}{2}L_1L_2\sin\alpha \approx \gamma_{LV}L^2\sin\alpha \quad (3.4)$$

$$W_{TOT} = W_{SL} + W_{SV} + W_{LV} \approx 2\gamma_{SL}L^2 + \gamma_{LV}L^2\sin\alpha \quad (3.5)$$

Therefore, the torque T acting on the part can be expressed as a function of substrate tilting angle α after differentiating W_{TOT} with respect to α .

$$T = -\frac{dW_{TOT}}{d\alpha} = -\gamma_{LV}L^2\cos\alpha \quad (3.6)$$

Based on this model, part size scaling is analyzed in single angle assembly and feedback assembly,

which uses substrate tilting angle modification to increase the capillary torque after forming line contact to overcome the size limit of single angle assembly.

3.4 Single angle assembly

Due to decrease of the torque per unit area with increase of part size as shown in Table 3.1, large parts are repelled and result in no assembly. Through an additional experiment and equation (6) with $1 \times 1 \text{ mm}^2$ parts for different substrate tilting angles α , we determine the critical torque per unit area for successful assembly. In this experiment, $1 \times 1 \text{ mm}^2$ parts are assembled at various substrate tilting angles α up to 24.1° , which indicates the minimum torque per unit area is $0.071 \text{ } \mu\text{N/m}$. Compared with this value, 3×3 and $5 \times 5 \text{ mm}^2$ parts have 0.048 and $0.022 \text{ } \mu\text{N/m}$ respectively. These smaller torques per unit area cause them to be repelled by the upward meniscus during pull-up and prevent them from assembly although the parts approach the substrate and make line contact at a certain angle of $\alpha = \alpha_1$ (Figure 3.3(a) and (b)). The torque per unit area should be greater than the critical value.

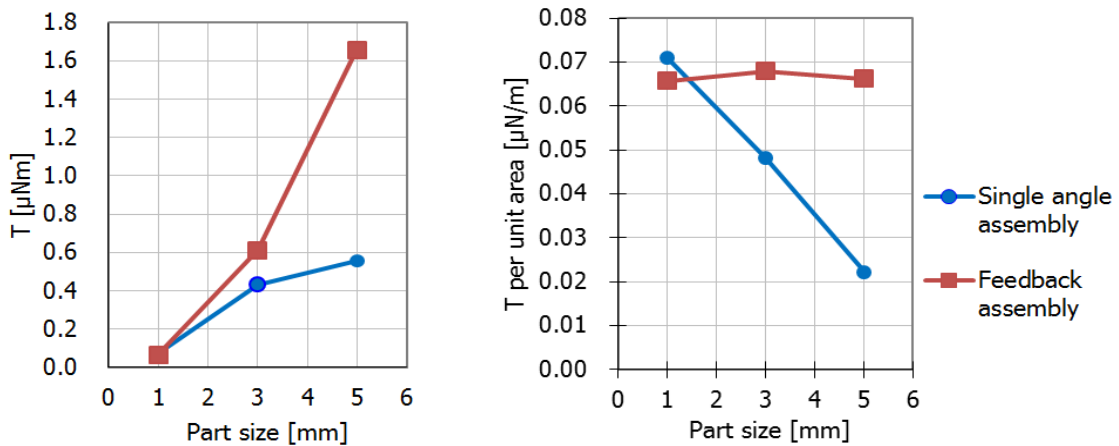


Figure 3.6: Analysis of the capillary torque vs. part size (1×1 , 3×3 and $5 \times 5 \text{ mm}^2$ parts with $100 \text{ } \mu\text{m}$ thickness) in single angle assembly feedback assembly (see Table 3.2).

Based on this analysis and Figure 3.6, the maximum part size for assembly is predicted to be around $2 \times 2 \text{ mm}^2$ at $\alpha = \alpha_1 \approx 25^\circ$. There is zero assembly for 3×3 and $5 \times 5 \text{ mm}^2$ parts.

However, 3×3 and $5 \times 5 \text{ mm}^2$ parts can be assembled using feedback assembly at two different substrate tilting angles, α_1 for a part approaching the substrate and α_2 for increasing the capillary torque. This method is discussed in the next section.

3.5 Feedback assembly for large parts

The maximum assemblable part size using single angle assembly is around $2 \times 2 \text{ mm}^2$. However, we can change the substrate tilting angle α to increase the capillary torque keeping initial line contact. Once the part makes line contact at $\alpha = \alpha_1$, it tends to be pinned due to the capillary force in the contact region. This pinning effect enables us to change the substrate tilting angle to a different value, $\alpha = \alpha_2 < \alpha_1$ maintaining line contact. Thus, a larger capillary torque can be achieved by decreasing α for large parts as shown in Figure 3.7.

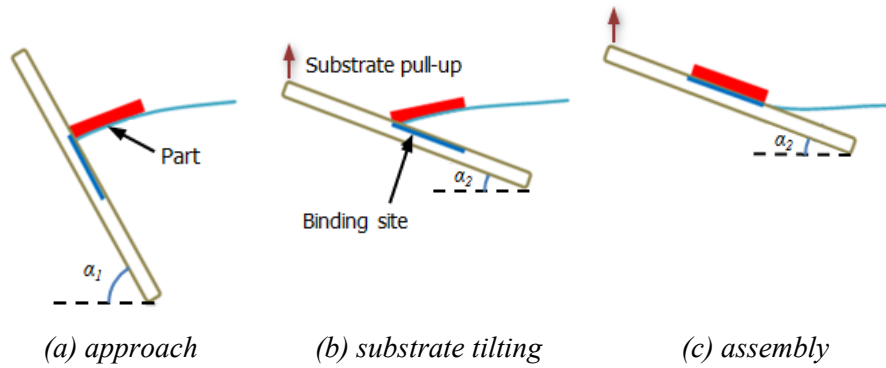


Figure 3.7: Schematic of feedback assembly. A part forms line contact at α_1 . The critical capillary torque is obtained at α_2 and the part is assembled by pulling up the substrate.

Table 3.2: Feedback assembly test result. The substrate tilting angles are changed from Table 3.1 after forming line contact. The surface tension induced torque per unit area for each part should be larger than its critical value ($0.066 \text{ } \mu\text{N/m}$) for assembly. The torque and torque per unit area are calculated based on the model at the maximum substrate tilting angle.

Part size, $L \times L$ [mm^2]	Part volume [mm^3]	α_1 [$^\circ$]	α_2 [$^\circ$]	Torque, T [$\mu\text{N/m}$]	T per unit area [$\mu\text{N/m}$]	Assembly
1×1	0.1	10	24.1	0.07	0.066	Yes
3×3	0.9	48.2	19.2	0.61	0.068	Yes
5×5	2.5	72.1	23.0	1.66	0.066	Yes

As shown in Table 3.2, once $3 \times 3 \text{ mm}^2$ parts approach the substrate at $\alpha_1 = 48.2^\circ$ and form line contact, the substrate is tilted down to $\alpha_2 = 19.2^\circ$ maintaining the line contact. Thus the capillary torque per unit area reaches the critical value at $\alpha = \alpha_2$ and successful assembly is achieved.

Through the same procedure, the minimum substrate tilting angles α_2 for different part sizes are experimentally determined and corresponding capillary torques are calculated. Table 3.2 shows the experimental and calculated results. It is observed that parts with different dimensions have the same capillary torques per unit area when they can be assembled.

3.6 Conclusions

The mechanics is analyzed using a capillary torque model and verified using 1×1 , 3×3 and 5×5 mm² parts. The minimum torque per unit area is experimentally determined for various part sizes. The results indicate there is a limit on the lateral size of the parts that can be assembled when we use just one substrate tilting angle. Based on our analysis, we also propose a novel method that is capable of assembling parts of higher lateral dimensions using parametric changes in substrate tilting angle.

CHAPTER 4. ORIENTATION CONTROLLED PARALLEL ASSEMBLY USING MAGNETIC FIELD

4.1 Introduction

In Chapter 2 and Chapter 3, we introduced fluidic self-assembly (FSA) at an air–water interface and demonstrated high yield using surface Faraday waves [27, 28], which achieves a selective assembly to preprogrammed sites. We also presented a comprehensive model and experimental support that extends the applicability of the assembly method to a wide range (1 to 5 mm) of part sizes and designs. In these methods, the parts are assembled in four possible orientations (0° , 90° , 180° , 270°) due to their square shape.

FSA in unique orientation is important for maximal area efficiency in circuit and component design and improving functional diversification and function densification (More-than-Moore [5]). This chapter presents a novel FSA method that assembled thin silicon parts ($2000 \times 2000 \times 100$, $4000 \times 4000 \times 100 \mu\text{m}^3$), which is vital for many applications in miniaturized platforms but problematic for today’s pick-and-place robots, in unique orientation. The parts are assembled in preprogrammed hydrophilic binding sites on a substrate with self-alignment and unique orientation assisted by a magnetic field.

Experiments and analysis are presented with an emphasis on the combined effect of controlled surface waves and magnetic force. For various gap values between a magnet and Ni patterned parts, magnetic force distributions are generated using Monte-Carlo simulation and employed to predict assembly yield. An analysis of these distributions shows that a decline in yield following the probability density function can be expected with degrading conditions. The experimentally determined critical magnetic force is in good agreement with a derived value from a model of competing forces acting on a part. A general set of design guidelines is also presented from the developed model and experimental data.

4.2 Assembly process

The novel orientation-specific FSA system is basically the same with the one in Chapter 2 except magnets and ferromagnetic Ni patterns. The FSA system is illustrated in Figure 4.1 consists of a water container on a linear electromagnetic vertical vibration table (Brüel & Kjør Type 4809), a dip coater (KSV Dip Coater) with an affixed substrate and parts floating at an air-water interface. The acceleration uniformity over the vibration table is $\pm 10 \text{ mg}$ or 0.72% as measured using a laser vibrometer (Polytec OFV-534 laser unit and OFV-2500 vibrometer controller) when driven at $80 \text{ Hz}/1.5 \text{ g}$ ($1 \text{ g} = 9.8 \text{ m/s}^2$)

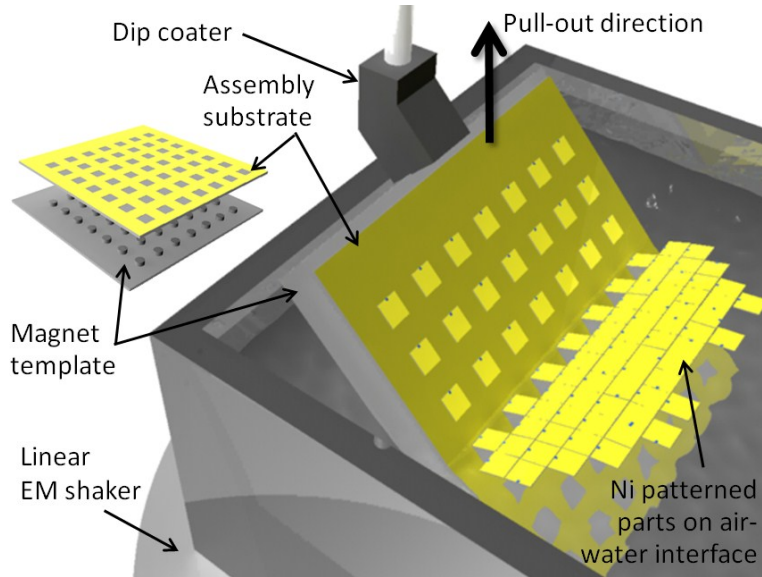


Figure 4.1: The experimental setup for orientation-specific assembly. The system consists of a water container, linear electromagnetic vibration table, dip coater, substrate, magnets and parts floating at the air-water interface.

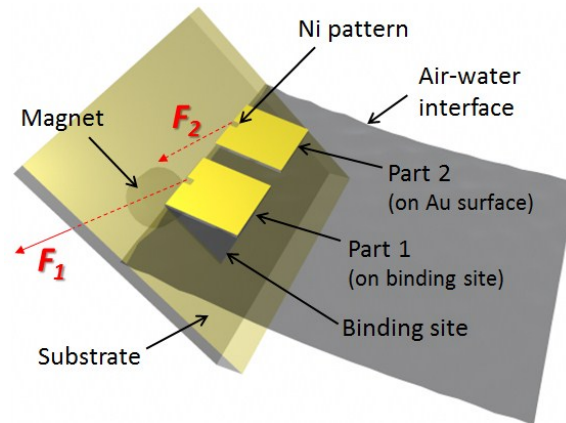


Figure 4.2: Schematic of two parts on a substrate for simulation of magnetic forces. F_1 and F_2 indicate the force on a part on a binding site and on its neighboring part, respectively. Part 2 should be repelled.

The substrate is tilted at a 45° angle with the water surface and vertically pulled up by the dip coater. This angle is set to easily repel parts on non-binding sites during pull-up. If the substrate tilting angle is too steep, assembly becomes difficult because the gravitation force on parts increases. Conversely, if the angle is too small, repelling parts is not easy. 45° is selected considering assembly and repelling. During substrate pull-up, the parts approach the substrate due to the meniscus formed by the hydrophobic (SAM: self-assembled monolayer-coated Au) and hydrophilic (Si oxide) patterns on the substrate (Figure 4.3 (a)). The parts are uniquely oriented

by the magnetic field of a rare-earth neodymium iron boron (NeFeB, Grade N40) magnet beneath each binding site. Accurate magnet-binding site alignment was achieved using photolithographically patterned “magnet templates”. The magnets are placed in the 100 μm deep trenches on the template. Then the magnet template is aligned with the assembly substrate. Surface waves are applied to prevent multiple parts from approaching one site and to achieve one-to-one part-to-site registration in proper orientation. Then the parts are assembled (Figure 4.3(a) to (d)) by pulling up the substrate. For successful assembly, the force on Part 1 should exceed the critical value while the force on Part 2 (Figure 4.2) should be minimized to repel the part during the substrate pull-up.

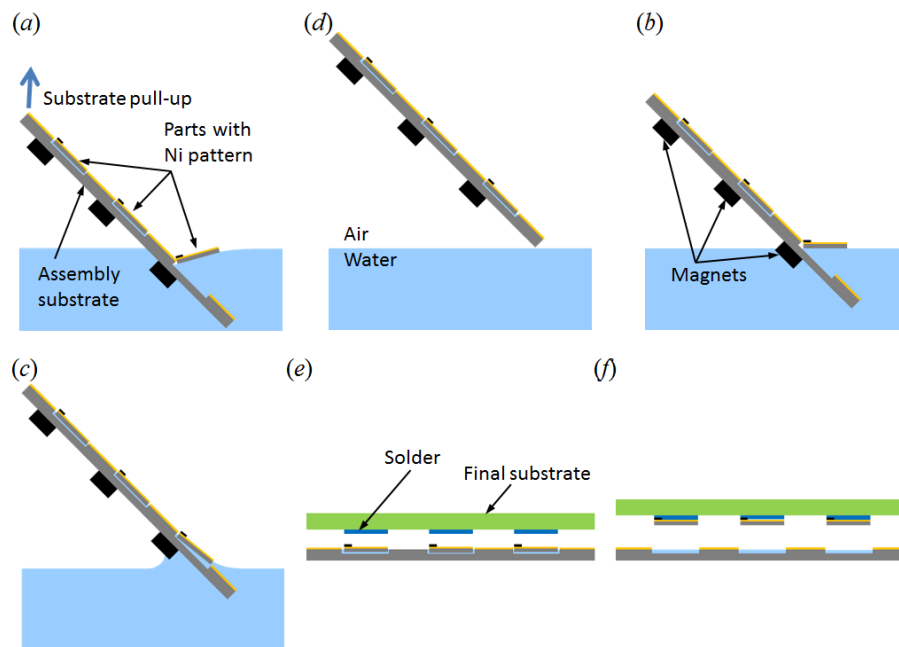


Figure 4.3: Full process flow for orientation-specific assembly. (a) Parts approach the substrate driven by the downward meniscus and magnetic field and (b-d) are assembled by substrate pull-up. (e) Parts are attached to a final substrate. (f) The process is completed by removing assembled parts from the assembly substrate.

The parts at the air-water interface approach the substrate Ni-patterned side first due to the magnetic field and make a line contact in step (a). As the substrate is pulled up at a constant speed of 0.61 mm/s, the meniscus curvature changes from convex to concave due to surface tension of the water and the hydrophilic property of the binding site. During transition from (b) to (d) in Figure 4.3, the part at the substrate-water interface is attracted towards the assembly substrate by

capillary action and magnetic force. Once the assembly is done, the parts are attached to a final destination substrate or device (e) and released from the assembly substrate (f).

All experimental data in this paper is acquired using the assembly system in Figure 4.1. However, the proposed assembly system can be modified for a roll-to-roll process (Figure 4.4). The parts are released from a tape and approach the binding sites for assembly. The continuous flexible substrate is fed by a roller which prints the binding sites.

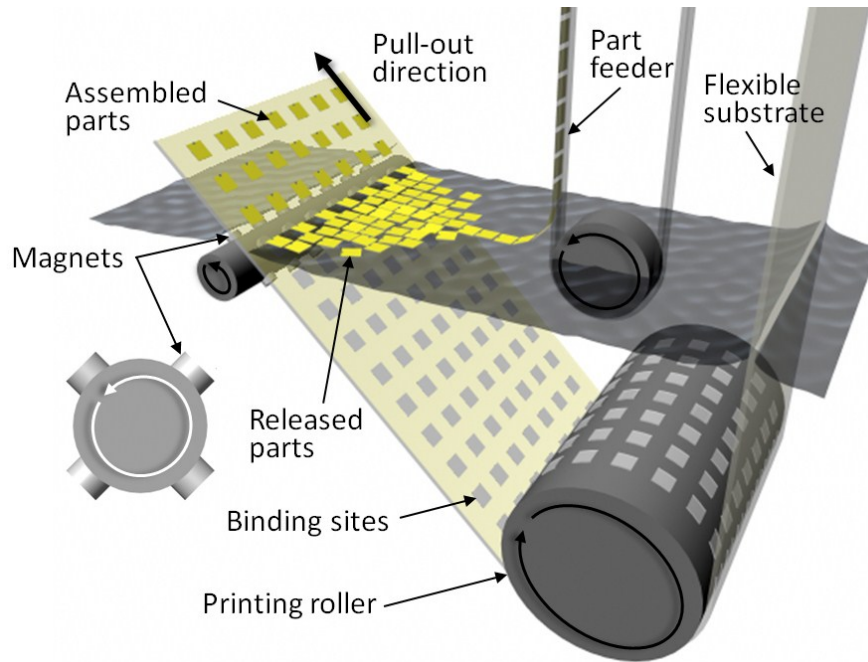


Figure 4.4: The proposed FSA system can be modified for roll-to-roll process with a flexible substrate. Instead of a magnet template, a roller with magnets attached attracts and assembles the released parts.

4.3 Fabrication

The 2 mm sized parts with thick magnetic Ni patterns are fabricated from an SOI wafer by a two-mask photolithography process: The SOI wafer is first coated with Cr/Au (10/100 nm) thin film by electron beam evaporation. The wafer is then spin coated with 12 μm thick AZ4620 photoresist and patterned by standard photolithography to define the exposed areas of square windows (200×200 , $400 \times 400 \mu\text{m}^2$). A 10 μm thick Ni film is coated on the exposed Au areas by electroplating. After the photoresist removal process, the wafer is coated with 12 μm thick AZ4620 again and a second mask is used to define the boundary gaps for DRIE. After the DRIE, the parts are released from the wafer by HF. The parts are collected and rinsed in acetone and

oxidized by H_2O_2 to create the hydrophilic property on the silicon side. The silicon oxide layer on the substrate and parts serves as a passivation layer and ion absorption is minimized using deionized water. The Au coated side is treated with SAM that renders the surface hydrophobic. The SAM formed from thiols on gold is stable for days to weeks [32] while the assembly process takes a few minutes or less. Thus, high wettability contrast is maintained until the assembly is completed. Regarding the viability of commercial parts, SAM attaches only on Au surfaces (electrodes). The other areas are coated with a passivation layer (usually oxide or nitride), which protects the circuit from chemical attack throughout the SAM attachment process.

4.4 The effect of Faraday waves

Standing wave patterns in a layer of liquid enclosed by a vibrating container are known as Faraday waves. In our FSA system, the surface Faraday waves are generated by use of a vertical electromagnetic shaker driven at 80 Hz/1.5 g. Typical yield loss in FSA is due to lack of control of one-on-one part-to-site registration. In our method, the parts are restricted to a surface layer and hence many are available for assembly. We avoid multiple parts approaching the same site and guarantee high yield by use of surface waves.

When parts approach the substrate, it is possible that none or only wrongly oriented parts occupy a binding site due to the stochastic approach shown in Figure 4.5. Figure 4.5(a) and (b) show how the Faraday waves fix the parts that are wrongly oriented at 90° and 180° within 1.5 s on average. Figure 4.5(c) and (d) show how the Faraday waves help the parts registration after the approach. Correctly registered parts experience a stronger magnetic force and thus are less likely to be repelled while subjected to Faraday waves. After achieving the proper arrangement of parts with unique orientation (Figure 4.5(d)), the substrate can be pulled up for assembly.

When parts are distributed at the air-water interface with no external field applied, they attract each other due to their matching sidewall wettability as shown in Figure 4.6(a). No specific pattern in angular distribution is observed in Figure 4.6(a) and (b). There are four groups with almost the same counts in Figure 4.6(c), which indicates no preferred angular distribution. Our assembly system with downward meniscus near the assembly substrate, magnetic field and Faraday waves modifies the part angle distribution (Figure 4.6(d)). Figure 4.6(e) and (f) show the increased number of parts oriented toward the substrate (-90°) near the assembly substrate under the magnetic field and Faraday waves. Once one-to-one part-to-binding site registration is achieved, the parts are assembled with high yield by substrate pull-up.

The assembly is processed row-by-row while the substrate is pulled up through the air-water interface. A virtual 100 % yield is achievable if more than 20 s of Faraday waves are applied for each row. Assembly speed is increased if the FSA system is equipped with visual feedback

control to apply Faraday waves until one-to-one part-to-site registration is achieved. Figure 4.7 shows the orientation-specific assembly with 2D integration density of 40 %. The gap between magnets and parts is set at 0.87 mm. On average, 8 s of surface waves (80 Hz/1.5 g) are applied for each row and repeatable high yield assembly of 81 parts is achieved in 70 s. In comparison, today's pick-and-place machines with 6 to 20 robots assemble 1.7 components per second (cps) per robotic arm. The assembly speed of the proposed system is 1.2 cps.

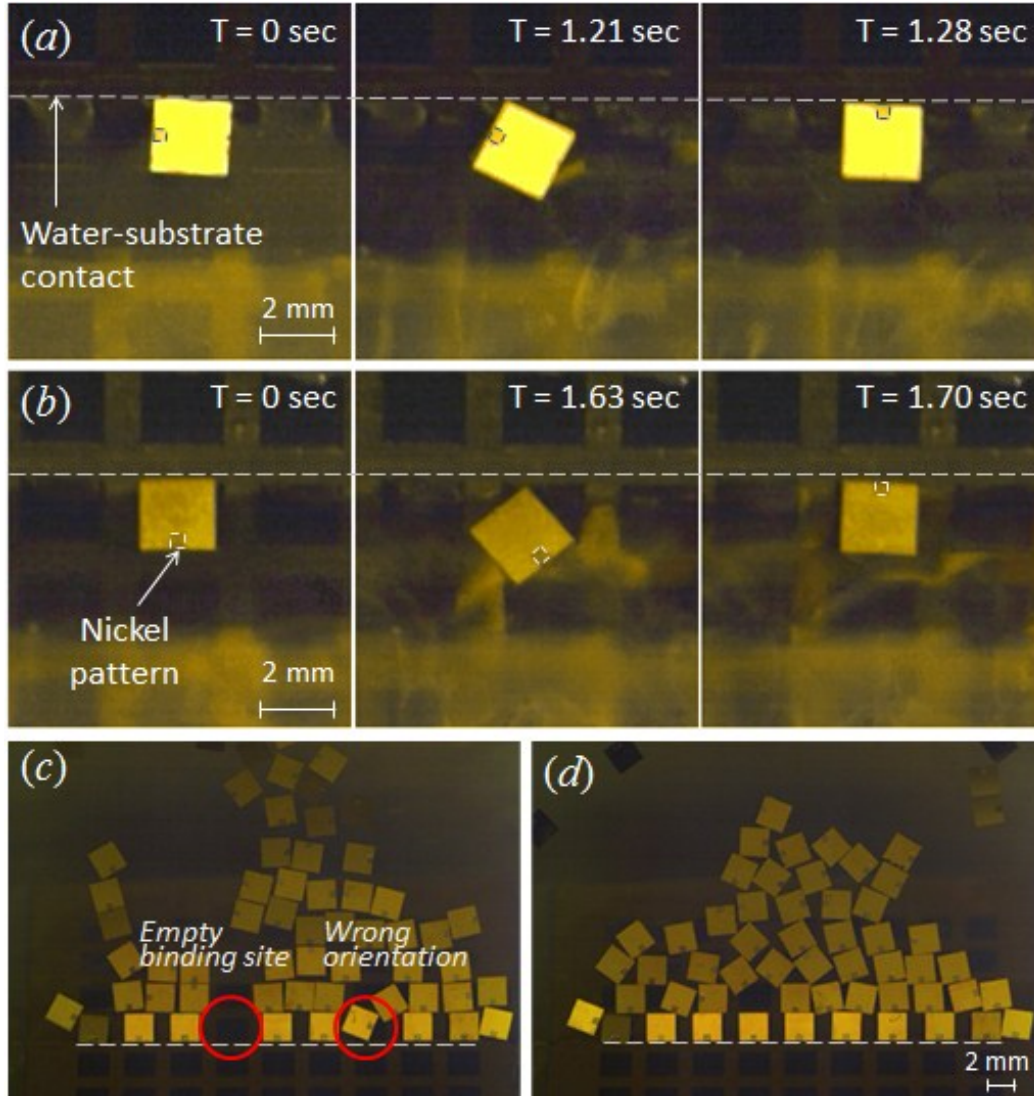


Figure 4.5: Part ($2000 \times 2000 \times 100 \mu\text{m}^3$) rearrangement by surface Faraday waves (top view). Dark squares are hydrophilic binding sites and gold regions are hydrophobic surfaces. (a) 90° correction. (b) 180° correction. (c) One binding site is empty and the other one is approached by two parts. (d) Surface Faraday waves (80 Hz, 1.5 g) are applied, resulting in a rearrangement of the parts.

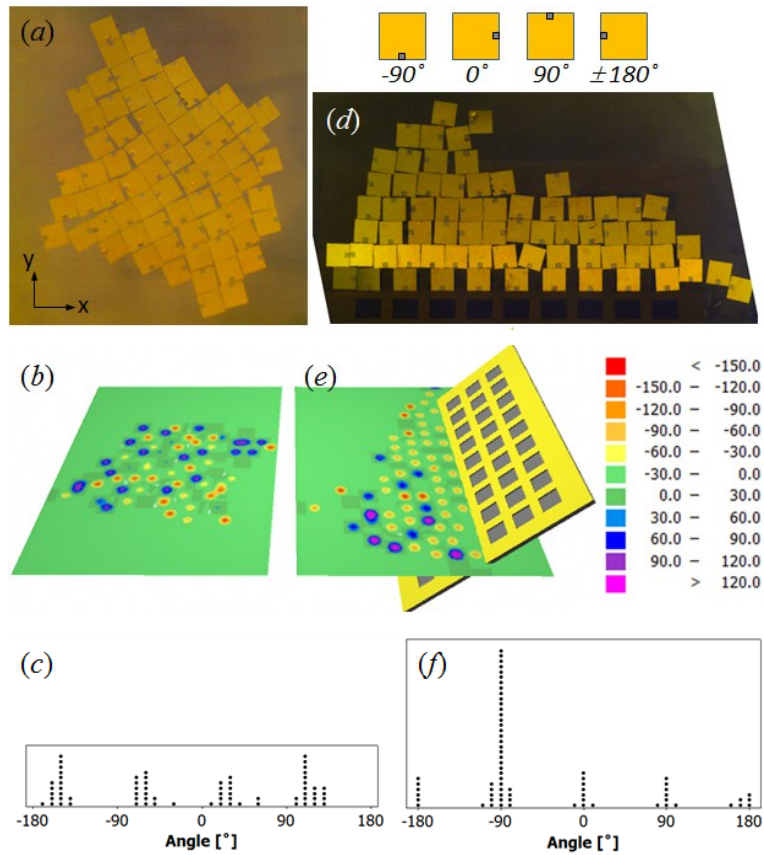


Figure 4.6: Part angle distribution. (a-c) before agitation, (d-f) after agitation in a magnetic field. A peak with high density of parts oriented at -90° is observed after agitation.

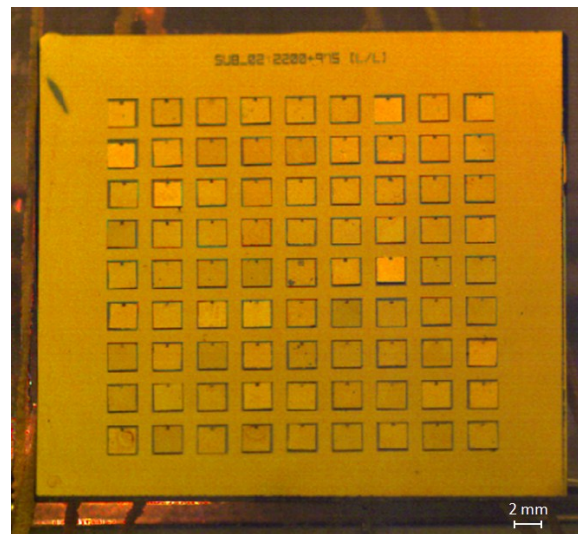


Figure 4.7: Assembly result with unique orientation. High yield (100 %) is achieved using a visual check of one-on-one part-to-site registration for each row before substrate pull-up.

4.5 The effect of magnetic field

The experiments in Figure 4.6 and Figure 4.7 indicate that assembly yield increases with a larger magnetic force F_m . We hypothesize that a critical magnetic force F_{mc} exists that guarantees successful assembly. Due to stochastic variations in a practical setup, the actual magnetic force F_m is not a unique value but exhibits a distribution. We derive this distribution by taking into account the variations in the setup parameters and show that the results are consistent with our experimental observations, leading to a concise stochastic model for assembly yield.

To determine experimentally an estimate of the critical magnetic force F_{mc} for successful assembly, various gaps between a magnet and a Ni-patterned part are tested, as shown in Figure 4.8. For this experiment, parts with 200 μm Ni pattern and magnets with diameter of 1/16" are used. Microscope slides with different thicknesses are used as a spacer to control the gap. Each condition is repeated 30 times for statistical yield analysis.

In repeated experiments, uncontrollable and inevitable variations from measurement in gap, misalignment between components, substrate tilting angle and angle between a substrate and a part produce different assembly yields. The assembly process with higher magnetic force becomes more robust against the inevitable process variations. Therefore, higher yield is observed at higher magnetic force and yield is saturated around 20 μN . Table 4.1 shows tested gap values with corresponding experimental yields.

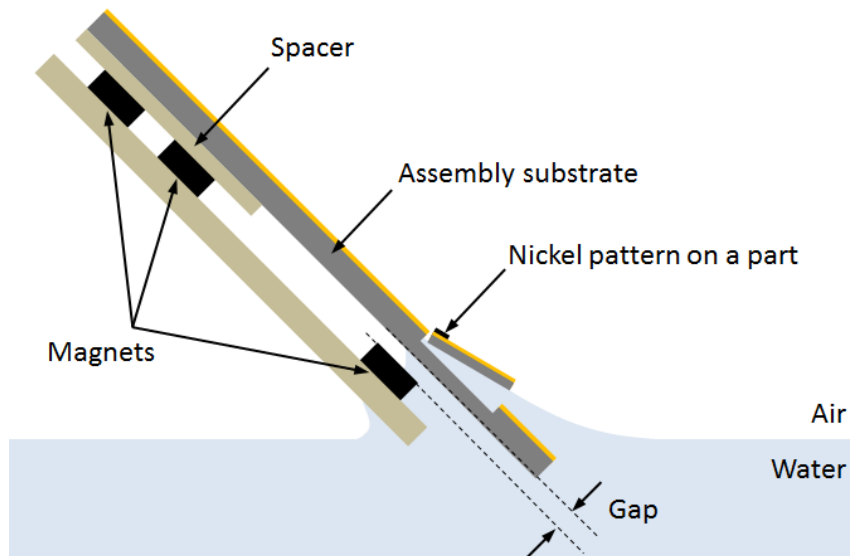


Figure 4.8: Experimental setup to determine the critical magnetic force F_{mc} . The magnetic force acting on the part can be controlled via the gap size.

Table 4.1: Assembly results for different gaps and simulated magnetic force F_m (average, average ± 3 sigma) for the square patterned substrate. Yields are predicted using Monte-Carlo simulation ($N = 4000$) and F_m distribution. Critical magnetic force F_{mc} for successful assembly is estimated to be $6.4 \mu\text{N}$ based on the method of least squares.

Gap [mm]	Assembly yield [%]		F_m [μN]	
	Experiment	Predicted	Simulation	
0.87	100	(30/30)	100	20.3 (12.7-27.9)
1.07	90	(27/30)	100	10.6 (6.5-14.6)
1.19	67	(20/30)	78	7.2 (4.2-10.1)
1.24	37	(11/30)	34	6.1 (3.4-8.7)
1.33	0	(0/30)	0	4.4 (2.3-6.4)

The distribution of the gap is simulated using the Monte-Carlo method (sample size $N = 4000$), which is a stochastic technique based on the use of random numbers and probability distributions to study a system. Errors caused from measurement (nominal gap size: $0.87 - 1.33$ mm, 3 sigma = $120 \mu\text{m}$, from test), magnet-substrate alignment (nominal alignment $0 \mu\text{m}$, 3 sigma = $100 \mu\text{m}$, from test) and part-binding site alignment (nominal lateral dimensions: binding site 2.2 mm, part 2 mm, 3 sigma = $100 \mu\text{m}$, from dimensional mismatch) are considered in the simulation. For each gap value, five points (average, $\pm 1, 3$ sigma) are selected to simulate magnetic forces using COMSOL MultiphysicsTM. The magnetic forces with the other gap values are computed using linear interpolation and then average and range (± 3 sigma) are calculated. Finally, predicted yields are calculated from simulated magnetic forces and their distributions (Table 4.1).

Figure 4.9 shows the distributions of the simulated magnetic forces. By placing a vertical line as a critical magnetic force candidate, the expected assembly yield can be derived by calculating the area on the right side of the line for each distribution. For example, if the vertical line is located at $6.4 \mu\text{N}$, 1.33 mm gap ($F_m = 4.4 \mu\text{N}$) has almost 0 % yield and 1.19 mm ($F_m = 7.2 \mu\text{N}$) gap has 36 % yield. By adjusting the vertical line position, the critical magnetic force can be determined by comparing predicted yields with experimental ones.

The least squares method (LSM) is employed to estimate the critical magnetic force by fitting experimentally obtained data with the graph of predicted yield. As a result, the critical value of the magnetic force F_{mc} is estimated to be $6.4 \mu\text{N}$, at which minimum root-mean-square (RMS) error between experimental and calculated yields is observed. The experimental and predicted yields are presented in Table 4.1 and Figure 4.10. The RMS and maximum errors between

experimental and predicted yields are 11 % and 17 %, respectively. Although only 6.4 μN is necessary for assembly, the assembly process is so sensitive to inevitable process variations that it fails to have repeatability for this force, leading to a yield of only 50 %. The assembly system becomes more robust against the process variations as higher magnetic force is applied and thus higher yield and repeatability are achievable. The analysis of distributions indicates a magnetic force of 20 μN is desired for robustness and repeatable assembly yield near 100 %.

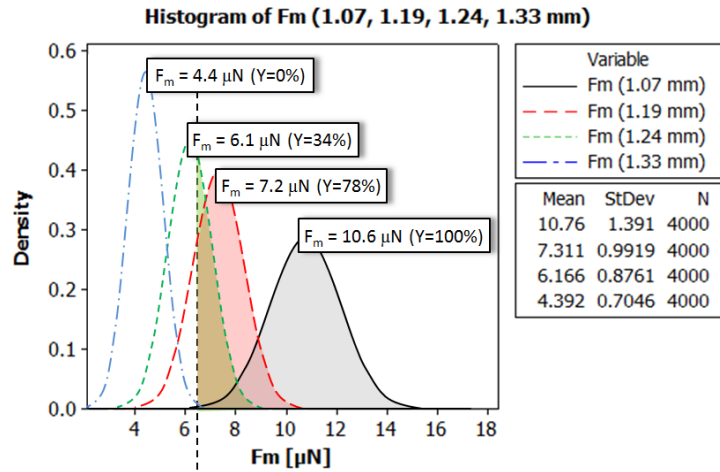


Figure 4.9: Distributions of the magnetic forces, F_m with different gaps. F_m distribution is the result of Monte-Carlo simulation considering accumulated error from magnet-substrate alignment, part position and measurement error. The colored areas indicate the assembly yield Y . The critical magnetic force, F_{mc} is found to be 6.4 μN .

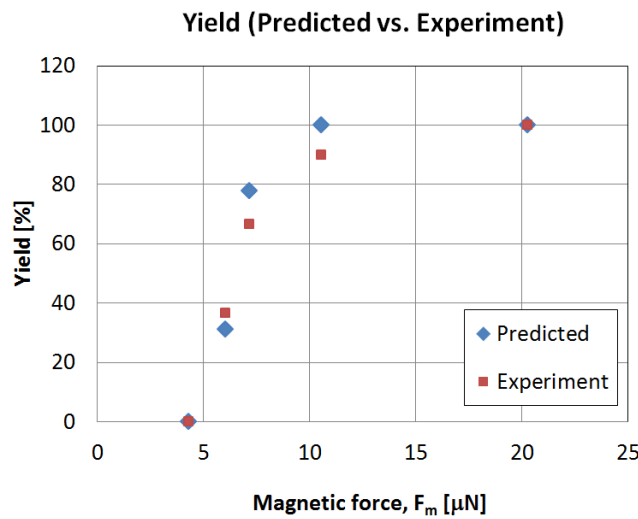


Figure 4.10: Comparison of predicted and experimental yield under the estimated critical magnetic force $F_{mc} = 6.4 \mu\text{N}$. The graph shows 11 % RMS error and 17 % maximum error.

4.6 Assembly model

The experimental results clarify how the magnetic force determines the assembly result. Here, we present an analytical model for critical magnetic force. Competing forces on a part are first described, and the effects of substrate design on the shape of the meniscus which changes the repelling force are studied. Finally, the model is verified by comparing model-based and experimental critical magnetic forces.

Competing forces on a part in contact with a binding site are analyzed using the diagram illustrated in Figure 4.11. First, the gravitational and magnetic forces in Figure 4.11 are expressed in equations (4.1) and (4.2). The *gravitational* force acts as a *repelling* force F_{rg} which is a function of mass of the part and the contact angle θ . The *magnetic* force F_{am} is determined by substrate tilting angle α and the contact angle θ . F_{am} attracts a part counter to F_{rg} .

$$F_{rg} = F_g \cos(90^\circ - \alpha + \theta) \quad (4.1)$$

$$F_{am} = F_m \sin\phi = F_m \sin(90^\circ - \theta) \quad (4.2)$$

In addition, there is a capillary force between a part and a binding site. Although this force attracts parts, its strength is found to be in the tens of nN throughout our experimental configurations (orders of magnitudes smaller than other components), allowing it to be safely ignored.

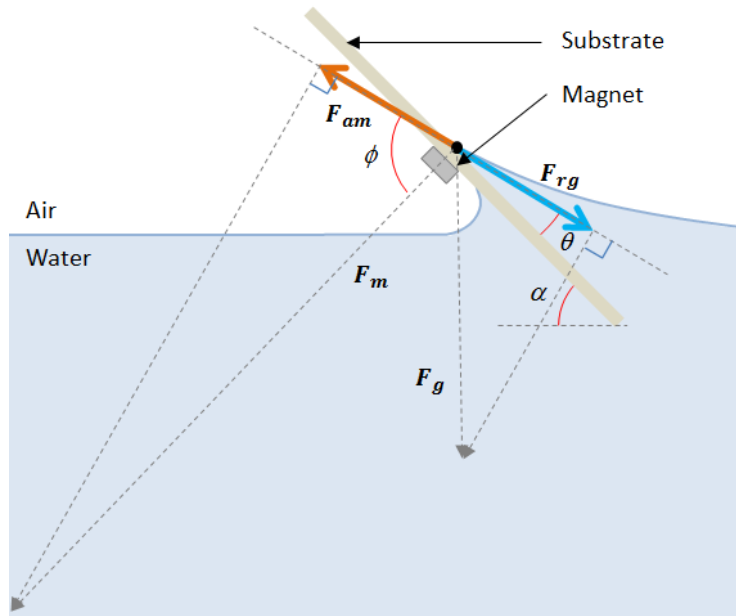


Figure 4.11: Competing forces on a part during substrate pull-up. The magnetic force should be greater than the repelling force caused by gravity and the slope of meniscus.

Therefore, the net force F_{net} on a part is expressed by equation (4.3). For successful assembly, F_{net} should be positive throughout the assembly process in Figure 4.3(a) to (c) where θ changes from α to 0° .

$$F_{net} = F_{am} - F_{rg} \quad (4.3)$$

4.6.1 Shape of meniscus

The shape of the meniscus without part can be expressed by equation (4.4) [34] by assuming an infinite container of liquid in contact with an infinite stripe patterned substrate. Here, ρ denotes the water density, γ the surface tension, g the gravitational acceleration, $\theta^* = 90 - \alpha + \theta$, and x the distance from the substrate.

$$u(x) = \sqrt{\frac{\gamma}{\rho g}} \cot \theta^* \cdot \exp\left(-\sqrt{\frac{\rho g}{\gamma}} x\right) \quad (4.4)$$

The menisci in Figure 4.12 are obtained from equation (4.4) and tests for each substrate design (stripe, square) are compared. A clear difference in the shapes is observed. Figure 4.12(a) shows two different shapes of menisci for a square and a stripe patterned substrate. The hydrophobic (SAM coated-Au) area next to hydrophilic binding sites pushes water away and shapes a more curved meniscus. Thus, equation (4.4) needs to be modified for a finite stripe or a square binding site based on the measured curvature of meniscus.

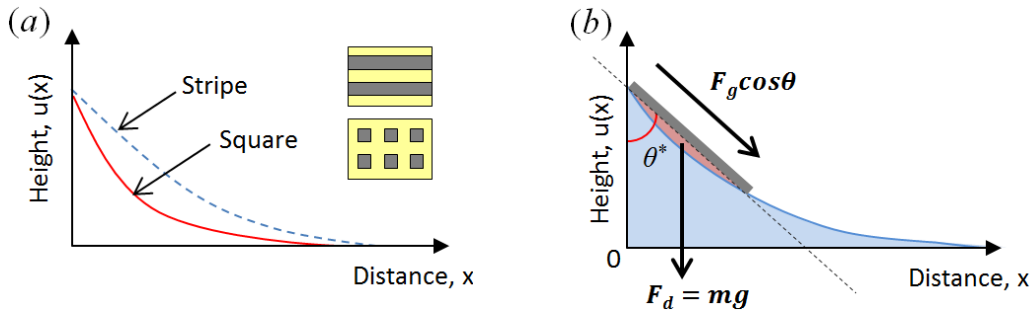


Figure 4.12: The effect of the shapes of the menisci on repelling force. (a) A square patterned substrate creates a more curved meniscus. (b) The hydrophilic bottom surface of a part induces repelling force.

When a part is in contact with a binding site, the hydrophilic bottom surface of the part pulls additional water underneath it (Figure 4.12(b)). Increased potential energy of the water acting on the bottom surface of the part induces a downward force F_d and its cosine component ($F_{rd} = F_d \cdot \cos \theta^*$) repels the part, so it is subtracted in equation (4.3):

$$F_{net} = F_{am} - F_{rg} - F_{rd} \quad (4.5)$$

Equation (4.3) and (4.5) describes the net force on a correctly registered part without Faraday waves. Faraday waves are applied before substrate pull-up. Thus the application of Faraday waves is a separate process from substrate pull-up and does not determine whether the parts are assembled or not. A part on a meniscus with a greater curvature pulls more water and generates a greater downward force F_{rd} on it. As a result, a square patterned substrate needs a stronger magnetic force than a stripe patterned one. This prediction is verified experimentally; the critical magnetic force for a square patterned substrate is $6.6 \mu\text{N}$, which is higher than $3.8 \mu\text{N}$ for a stripe patterned one. Here, the same method is applied to derive the critical magnetic force for the stripe patterned substrate. Two gap values are tested and yields are obtained from 30 replicate runs of experiments as shown in Table 4.2. The critical magnetic force for the stripe patterned substrate is derived to be $3.8 \mu\text{N}$ through the distribution and yield analysis.

Table 4.2: Assembly results for different gaps and simulated magnetic force F_m for the stripe patterned substrate. Critical magnetic force F_{mc} is estimated to be $3.8 \mu\text{N}$.

Gap [mm]	Assembly yield [%]			F_m [μN] (Simulation)
	Experiment		Predicted	
1.35	56.6	(17/30)	55.9	3.7 (1.7–5.7)
1.40	26.7	(8/30)	25.2	3.2 (1.4–5.0)

4.7 Model verification

For the verification of the developed model, two factors are considered: (i) substrate design (stripe and square) and (ii) part size (2, 4 mm). Four experimental tests are performed and compared with a model-based prediction.

First, 2 mm parts are tested. The critical forces for a square and a stripe patterned substrate are calculated based on the developed model. The plots in Figure 4.13 present model-based F_{net} for different magnetic forces over θ^* range through the assembly process (from 90° to 45°).

For a square patterned substrate with $F_m = 0 \mu\text{N}$, the net force F_{net} is below zero over all θ^* (Figure 4.13(a)), which indicates that a part in contact with a binding site is immediately repelled upon substrate pull-up. F_{net} becomes positive over all possible θ^* at $F_m > 6.4 \mu\text{N}$, which is the threshold magnetic force for assembly. It is only 2.4 % below the experimental result ($6.6 \mu\text{N}$). A stripe patterned substrate (Figure 4.13(b)) has a critical magnetic force of $3.8 \mu\text{N}$ (calculated with

equation (4) and (5), which is 3.3 % above the experimental value (3.6 μN). 3.3 % is the cumulative error from three forces ($F_{net} = F_{am} - F_{rg} - F_{rd}$). Thus, F_{rd} should have an error of less than 3.3 %.

4 mm parts are investigated in the same manner. Critical forces for different substrate designs are experimentally determined from the magnetic force distribution and yield analysis. They are compared with model-based values and show errors of less than 3.9 % (Table 4.3). The result of the comparison is presented in Table 4.3. The predicted values show good agreement with the experimental data and reflect the effect of the part size as well as the substrate design.

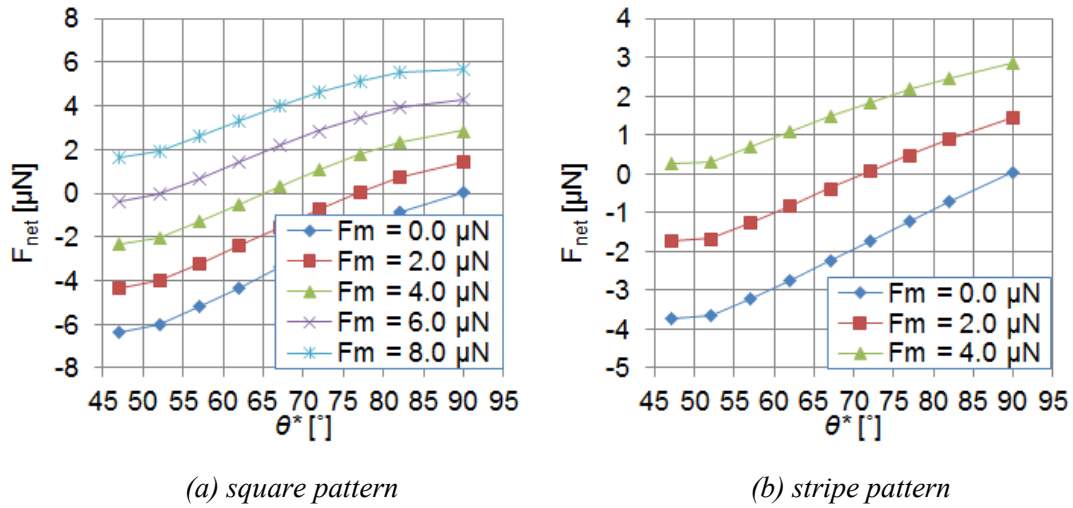


Figure 4.13: Net force change according to applied magnetic force on 2 mm sized parts with (a) a square patterned substrate and (b) a stripe patterned substrate.

Table 4.3: Result of comparison (model vs. experiment). Part size and substrate design are considered. Model predicts the critical magnetic forces with error less than 3.9 %.

Part size [mm]	Substrate design	Critical F_m [μN]		Error [%]
		Model	Experiment	
2	Stripe	6.4	6.6	2.4
	Square	3.8	3.6	3.3
4	Stripe	13.9	14.5	3.9
	Square	16.5	16.8	1.8

4.8 Design guidelines

Now we have a model for critical magnetic force for successful assembly. In this section, a guideline on how to choose the right design for a FSA system with a given part size (2 mm, 100 μm thick), gap (0.55 mm), substrate tilting angle (45°) and magnet strength (grade N40, cylindrical shape, thickness = radius = 1/32") is described. Critical design factors are determined via analysis of experiments and simulation data. They are then used to suggest guidelines for FSA system design.

4.8.1 Parameter selection

To investigate factors that affect the assembly result, magnet size, spacing between magnets and Ni pattern size on a part are selected (Table 4.4) as design parameters. Based on Table 4.4, assembly substrates with different inter-binding site spacing and 2 mm sized parts with 200 and 400 μm Ni patterns are fabricated. The experimental yields for the eight possible combinations are investigated using analysis of variance (ANOVA), which is a statistical method to assess the significance of each factor. The ANOVA test reveals that the magnet size and the Ni pattern size explain 89.6 % of the total variance and are selected as critical factors for further analysis.

Table 4.4: Design parameters and their contributions to assembly yield. Three design factors, each with two values, make eight combinations. Each run is repeated 30 times.

Parameter	Value		Contribution [%]
	Low	High	
Magnet size [mm]	1.59	3.18	74.8
Spacing [mm]	1.59	3.18	0.8
Ni pattern size [μm^2]	200×200	400×400	14.8

4.8.2 System design

Two critical parameters selected from the ANOVA test are used to provide guidelines for FSA system design. The magnetic forces on a part in contact with a binding site (Part 1) and its neighboring part (Part 2) on a SAM-coated Au surface are simulated using the magnet size and the Ni pattern size with COMSOL MultiphysicsTM software (Figure 4.2). The design point should be selected in order to assemble only Part 1.

Table 4.5: Simulated magnetic forces on a part on a binding site (Part 1) and on a neighboring part (Part 2). Experimental assembly yields are also presented.

Magnet size [mm] (diameter, thickness)	Ni pattern size [μm^2]	Magnetic force [μN] (Assembly yield)			
		Part 1		Part 2	
3.18, 1.59	200×200	137	(100 %)	24.0	(92 %)
	400×400	936	(100 %)	354.0	(100 %)
1.59, 0.79	200×200	96	(100 %)	0.0	(0 %)
	400×400	527	(100 %)	0.7	(0 %)
3.18, 1.59	300×300			179.5	
1.59, 0.79				0.4	

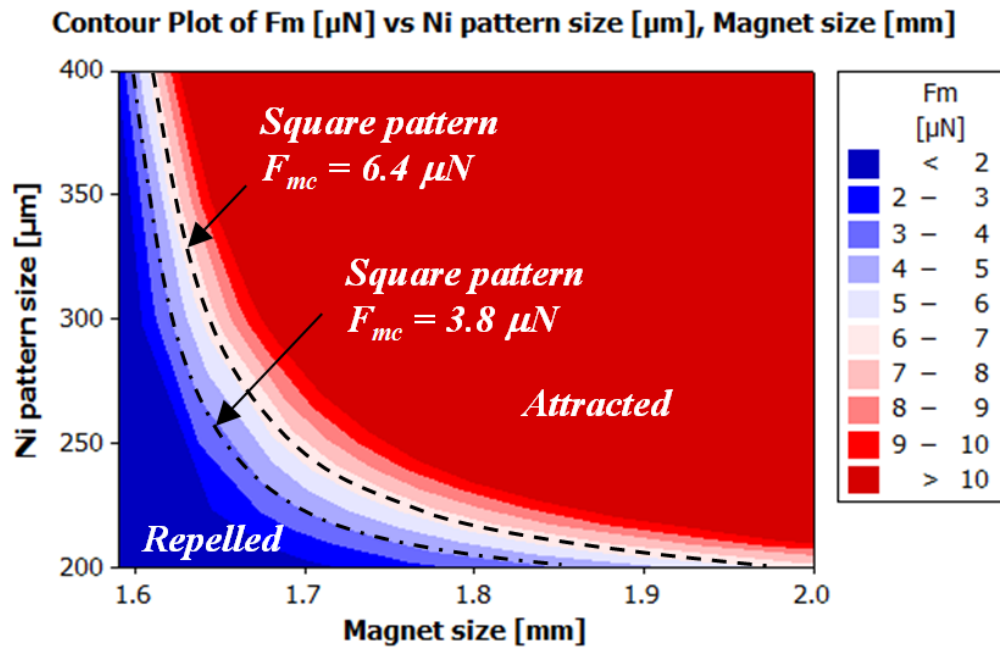


Figure 4.14: Contour plot of the simulated magnetic forces on Part 2. Part 2 with a magnetic force of less than the critical value will be repelled and result in successful assembly. Critical design conditions for a square patterned substrate and a stripe patterned one are also shown by dotted lines.

The simulated magnetic forces and assembly yields (Table 4.5) show successful selective assembly only when a smaller magnet (1.59 mm) is used. For a larger magnet (3.18 mm), Part 2 is also assembled on the SAM-coated Au surface regardless of the Ni pattern size.

From four assembly tests in Table 4.5 and two additional magnetic force simulations with the Ni pattern size of 300 μm , a guideline for the FSA system design is suggested using the plot of simulated magnetic forces on Part 2 (Figure 4.14).

Part 1 assembles on a binding site at every point in the plot owing to the strong magnetic forces (orders of magnitudes larger than the critical force). Thus, the plot for Part 1 is not presented. The FSA system should be carefully designed to repel Part 2. The design with 1.7 mm sized magnet and 350 μm Ni pattern (“Attracted” region) results in Part 1 on a binding site and/or Part 2 on a SAM-coated Au surface, which is an assembly failure. However, the design with 1.7 mm sized magnet and 200 μm Ni pattern (“Repelled” region) assemble only Part 1 on binding sites while repelling Part 2, which means successful selective assembly. In addition, the plot indicates that assembly yield is more sensitive to magnet size if the size of Ni pattern is 400 μm .

4.9 Conclusions

A novel orientation-specific FSA method using an air-water interface and a magnetic field is developed and analyzed. High yield assembly is demonstrated using $2000 \times 2000 \times 100 \mu\text{m}^3$ parts, which cannot be easily handled by pick-and-place machines but are crucial for 3D packaging and heterogeneous system integration. Magnetic fields and temporary Faraday waves are introduced to achieve selective assembly with unique orientation by part rearrangement.

A novel statistical strategy to derive critical magnetic force for assembly is described. Experimental results are statistically analyzed using Monte-Carlo simulation to estimate critical magnetic force. The simulation intentionally takes into account inevitable variations in process parameters and measurement uncertainty. The critical magnetic force is extracted from analysis of distributions of various magnetic forces and corresponding yields through the least squares method. The critical magnetic force is estimated to be 6.4 and 3.8 μN for a $2000 \times 2000 \times 100 \mu\text{m}^3$ part on a square patterned substrate and a stripe patterned one, respectively. However, an assembly system with critical magnetic force has a low yield and is vulnerable to process variations. A robust assembly system with highly repeatable yield near 100 % is achieved by increasing a magnetic force to 20 μN . Experimental yields are in good agreement with predicted ones over a wide range of magnetic forces. We also use a statistical strategy to study assembly yield using probability distributions. The probability density function explains the gradual decay in the yield as less favorable conditions are applied.

An analytical force model captures the competing forces on a part in the system to derive the

threshold for successful assembly. The critical forces are calculated and compared with the experimental ones. The model predicts the critical magnetic forces for 2 and 4 mm parts on a square patterned substrate and a stripe patterned one, which shows good agreement (error less than 3.9 %). Finally, based on the developed model and experimental data, a guideline of FSA system design is suggested to achieve selective assembly on a substrate.

CHAPTER 5. PARALLEL HETEROGENEOUS INTEGRATION

5.1 Introduction

Many research groups have developed self-assembly strategies [1, 2, 9-11, 18-22]. However, these assembly methods are not suited to assemble different parts simultaneously in unique orientation because of the inability of distinguishing desired parts from an unsorted collection of many different parts. Here, we present a novel FSA with unique angular orientation for heterogeneous integration of different-sized parts. The proposed FSA system selectively assembles appropriate parts at corresponding sites from a mixed collection of $2000 \times 2000 \times 100$ and $4000 \times 4000 \times 100 \mu\text{m}^3$ parts using a single pull-up process.

5.2 Assembly process

The novel FSA system for heterogeneous integration of and different-sized parts in Figure 5.1 is the same with the one in Chapter 4 except the dip coater is replaced with a stepper motor and gears for substrate pull-up. The FSA system consists of a water container on a linear electromagnetic shaker (Brüel & Kjær Type 4809), a stepper motor (Soyo, SY42STH38-0406A) with a controller (Phidgets, 1062), a substrate and two types of thin parts ($2000 \times 2000 \times 100$ and $4000 \times 4000 \times 100 \mu\text{m}^3$) with $10 \mu\text{m}$ thick Ni patterns floating at an air–water interface.

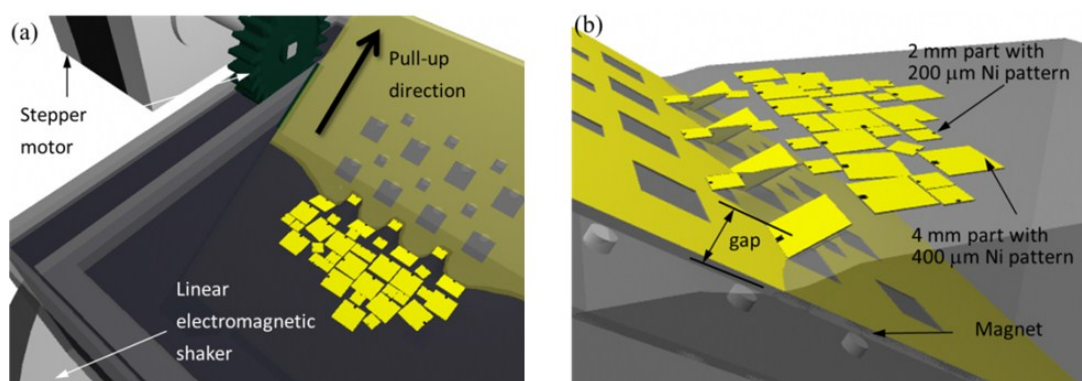


Figure 5.1: Heterogeneous assembly system with parts at air-water interface. (a) Assembly system consists of a water container on a linear electromagnetic shaker, and a stepper motor. (b) The magnetic force applied on a part, as a function of the size of the Ni pattern and the distance between the Ni pattern and a magnet, determines the size of the part to be assembled.

The substrate has preprogrammed hydrophilic binding sites and a SAM-coated hydrophobic Au area. The substrate is tilted at 45° with respect to the water surface. To attract Ni patterned parts in proper orientation, a cylindrical rare-earth neodymium iron boron (NeFeB, Grade N40, radius

= thickness = 1/32 inch) magnet is placed beneath each binding site. Accurate magnet-binding site alignment was achieved using photolithographically patterned “magnet templates”. Then the magnet template is placed under the substrate. The gap between a magnet and a part determines the magnitude of the magnetic force, which plays the most important role in the assembly of desired parts and disassembly of unwanted ones.

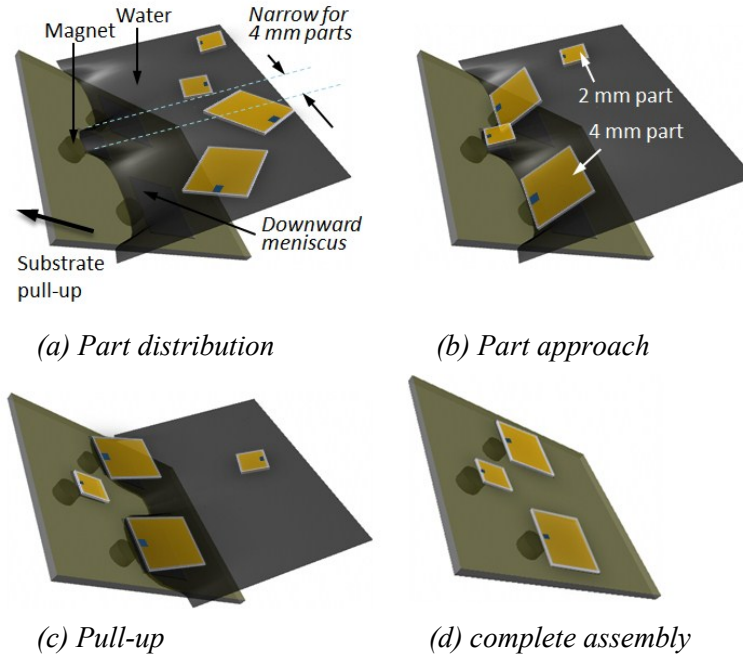


Figure 5.2: Assembly process for parallel heterogeneous assembly. Randomly distributed parts (2, 4 mm) at the air-water interface approach the binding sites with unique orientation and they are assembled by substrate pull-up.

The key to the parallel self-assembly of heterogeneous parts is the ability to differentiate the magnetic forces on different parts. For this reason, 2 mm parts are given a smaller Ni pattern ($200 \times 200 \times 10 \mu\text{m}^3$) than 4 mm parts ($400 \times 400 \times 10 \mu\text{m}^3$).

The hydrophilic binding sites and the hydrophobic background on the substrate create a curved meniscus along the substrate (Figure 5.2(a)). Randomly distributed heterogeneous (2, 4 mm) parts at the air-water interface approach the binding sites with unique orientation owing to the downward meniscus and the magnetic field (Figure 5.2 (b). If the magnetic force is strong enough to hold the parts during substrate pull-up, the parts are assembled (Figure 5.2 (c)).

5.3 Approach violations

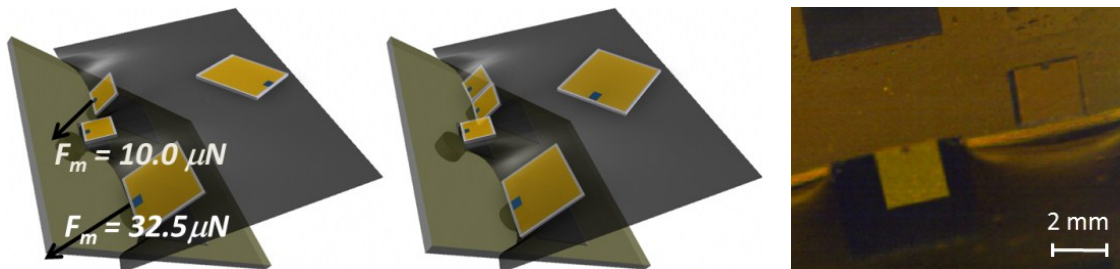
Differently sized parts need to be assembled on corresponding binding sites. However, the following three approach violations are observed due to the stochastic approach process. Temporary Faraday waves with different strengths fix these violations. Standing wave patterns in a layer of liquid enclosed by a vibrating container are known as Faraday waves.



(a) violation 1: 4 mm parts on 2 mm binding sites.



(b) violation 2: Parts in wrong orientation



(c) violation 3: 2 mm parts on 4 mm binding sites

Figure 5.3: Three approach violations in assembly process with magnetic forces determined from simulations. Correctly oriented 2 and 4 mm parts experience 10.0 and 32.5 μN , respectively. Weak magnetic force ($< 0.5 \mu\text{N}$) due to the increased gap (Ni pattern to magnet) makes the wrong parts easily repelled by weak Faraday waves. (a) 4 mm parts on 2 mm binding sites. (b) Parts in wrong orientation. (c) 2 mm parts on 4 mm binding sites.

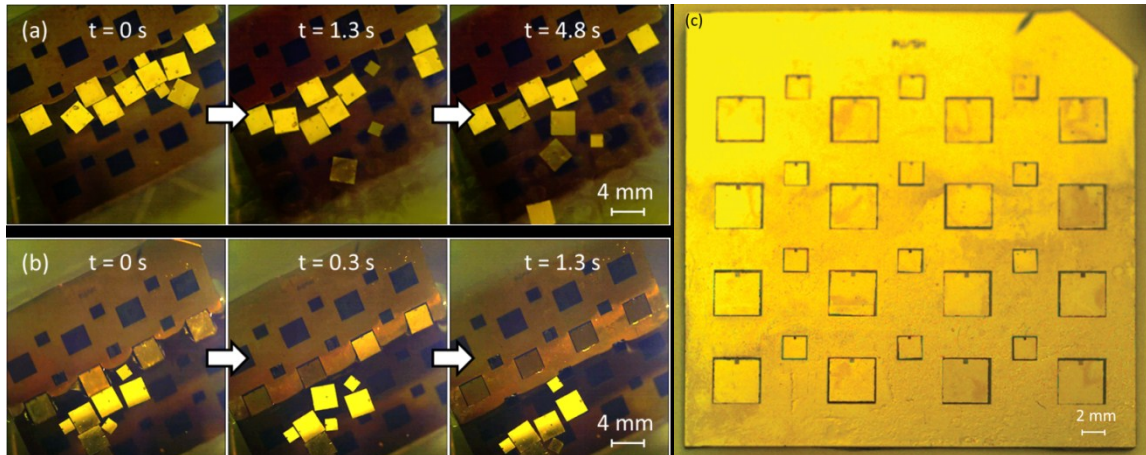


Figure 5.4: Faraday waves for one-to-one part-to-binding site registration. (a) Part rearrangement by Faraday waves. A 2 mm part on a 4 mm binding site is replaced with a 4 mm part after agitation. (b) Assembly is done by substrate pull-up. (c) Example of heterogeneous FSA (2 and 4 mm parts).

Approach violation 1: In general, 4 mm parts are easily attracted by the downward meniscus and magnetic fields. 4 mm parts, although not frequently observed, approach 2 mm binding sites (Figure 5.3(a)). The 4 mm parts make a point contact with the binding site to maximize the capillary contact area on the water surface. Weak magnetic force ($< 0.5 \mu\text{N}$) due to the increased gap (Ni pattern to magnet) makes the wrong parts easily repelled by weak Faraday waves (80 Hz/0.5 g). The strength of the waves is selected to keep in place correctly oriented 2 mm parts, which experience $10.0 \mu\text{N}$.

Approach violation 2: One or more wrongly oriented parts (90° or 180° , Figure 5.3(b)) are captured on binding sites. Such wrongly oriented parts experience weak magnetic forces ($< 0.5 \mu\text{N}$) and thus can be corrected using weak Faraday waves (80 Hz/0.5 g) which do not affect correctly oriented parts.

Approach violation 3: This occurs during assembly of 4 mm parts. One or two 2 mm parts are attracted to a 4 mm binding site (Figure 5.3(c)). The strength of agitation should be carefully selected to remove only 2 mm parts. Here, we utilize the difference between the magnetic forces on 2 and 4 mm parts. 2 mm parts are repelled by applying Faraday waves (80 Hz/1.7 g) whose strength is predicted to lie between 10.0 and $32.5 \mu\text{N}$. Then, 4 mm parts get another chance to approach (Figure 5.4(a)).

After achieving the desired part-to-binding site registration, the parts are assembled by substrate pull-up (Figure 5.4(b)). Figure 5.4(c) shows assembly results of heterogeneous FSA. The FSA system achieves the assembly speed of 0.7 components per second (cps) and the maximum

misalignment of $\pm 100 \mu\text{m}$ (delimited by the dimensions of binding sites and parts).

5.4 Selection of strength of Faraday waves

The magnetic forces on 2 and 4 mm parts decrease with increasing gap between a magnet and a Ni pattern (Figure 5.5(a)). The magnetic forces need to be larger than the minimum values to prevent disassembly of parts during substrate pull-up. These minimum magnetic forces are determined by finding the maximum gap that allows successful assembly. Simulated minimum magnetic forces for 2 and 4 mm parts are 6.4 and 16.5 μN , respectively. At a gap of 1.1 mm, the magnetic force on a 2 mm part (10.0 μN) is strong enough for assembly and sufficiently smaller than the magnetic force on a 4 mm part (32.5 μN). Thus, 2 mm parts on 4 mm binding sites (approach violation 3) can be selectively disassembled.

The assembly system and experiments include inevitable variations. The variations caused by measurement (nominal gap size: 0.87, 1.07, 1.19, 1.33 mm, 3 sigma = 120 μm , from test), magnet-substrate alignment (nominal alignment: 0 μm , 3 sigma = 100 μm , from test) and part-binding site alignment (nominal lateral dimensions: binding site 2.2/4.2 mm, part 2.0/4.0 mm, 3 sigma = 100 μm , from dimensional mismatch) are considered in Monte-Carlo simulations (N = 4000). They result in probability distributions of the magnetic forces (Figure 5.5(b)). Lower 3-sigma limits (m-3s) of 2 and 4 mm parts are higher than the minimum magnetic forces, so a gap of 1.1 mm ensures the assembly of both parts.

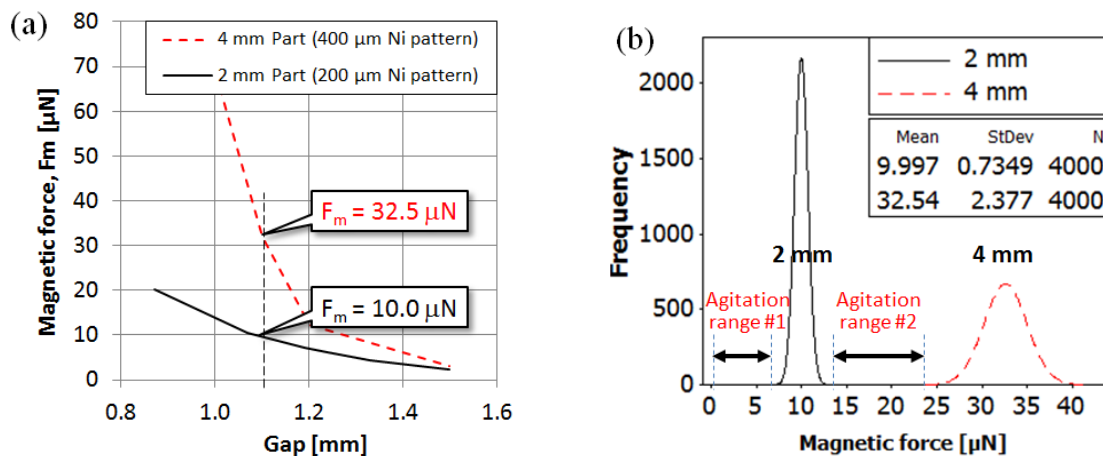


Figure 5.5: Determination of gap. (a) Suitable gap is determined to be 1.1 mm for stable assembly. (b) Two distinct distributions enable differentiation by part size.

The strength of the Faraday waves is adjusted according to the violation mode. The odd rows (2 mm) with approach violation 1 and 2 need weak Faraday waves (agitation range #1). The even

rows (4 mm) with approach violation 2 and 3 require the sequential increase of the strength of the Faraday waves. First, the weak Faraday waves (agitation range #1) correct the approach violation 2. Then the Faraday waves in agitation range #2 are necessary to correct the approach violation 3. In approach violation 3, the upper 3-sigma limit of 2 mm parts is 12.2 μN and the lower limit of 4 mm parts is 25.4 μN . Thus, the Faraday waves between 12.2 and 25.4 μN (agitation range #2) are necessary to repel 2 mm parts while keeping correctly oriented 4 mm parts. The robustness of the assembly system can be improved by increasing the distance between two distributions by changing the dimensions of Ni patterns, magnets, parts and the strength of the magnetic field.

5.5 Conclusions

A novel assembly method for 2D heterogeneous integration is presented and verified through experiments and analysis, including a correction strategy, employing Faraday waves, devised to rectify undesired part placements and orientations. 2 mm and 4 mm thin parts with 10 μm thick Ni patterns are selectively assembled with specific orientation in a row-by-row manner.

CHAPTER 6. SELF-ASSEMBLY OF THIN CIRCULAR PARTS

6.1 Introduction

Today's portable electronics (smartphone, tablet, digital camera, etc.) include digital and non-digital components to provide additional functions for increased performance. Non-digital components (e.g., RF/MEMS devices, sensors, actuators) interface with the physical world and play an equally important role in cost-effective and value-added systems. For functional densification, Moore's Law has ruled the down-scaling of digital components for the past decades. However, non-digital components do not scale at the same rate. Thus, functional diversification also known as a More-than-Moore technology gains significance to reach beyond the limit of the conventional More-Moore technology.

As described in Chapter 5, 3D integration provides higher performance, lower power consumption, and lower cost than 2D integration. 3D integration is already in use in some domains (cell phones and memory). Many research groups have developed self-assembly strategies [9-11, 18-22], which employ various driving forces. They, however, are not suited for orientation-specific assembly of thin disk-shaped parts. Rotating devices, MEMS oscillators, resonators, and optical components are often in disk shape and particularly difficult to assemble in a specific orientation because of their rotational symmetry.

Here, we demonstrate orientation-specific assembly of thin circular parts (diameter: 2 mm, thickness: 100 μm) and minimize the angular deviation through an analytical optimization of the magnetic field. The assembly of disk-shaped parts shows a three-fold higher assembly rate than square parts due to lower part-to-part interaction.

6.2 Assembly process

6.2.1 System setup

The FSA system in Figure 6.1(a) is basically the same with the system described in Chapter 5. The FSA system consists of a water container on a linear electromagnetic shaker (Brüel & Kjær Type 4809), thin circular parts floating at an air–water interface, the substrate with corresponding binding sites and a stepper motor (Soyo, SY42STH38-0406A) to pull up the substrate.

6.2.2 Assembly overview

Standing wave patterns in a layer of liquid enclosed by a vibrating container are known as Faraday waves. Faraday waves are generated using a vertical shaker (frequency: 80 Hz, acceleration amplitude: 1.5 g). Their purpose is to prevent multiple parts from approaching the same binding site, and thus ensures high yield.

Ni patterned circular parts randomly distributed at the air-water interface approach binding sites on an assembly substrate in unique orientation due to the magnetic fields and the downward meniscus (Figure 6.1 (b)). If the magnetic forces applied on the parts are strong enough to hold the parts at the binding sites during substrate pull-up, said parts will be assembled. Parts not on the binding sites experience less magnetic force due to the increased distances to the magnets. Thus, they are easily repelled by the Faraday waves. As the assembly for one row is completed, a water-substrate contact line slips down over a hydrophobic Au surface and pins to the next row. The slip-pin motion changes the shape of the meniscus from upward to downward and initiates the part approach process for a following row.

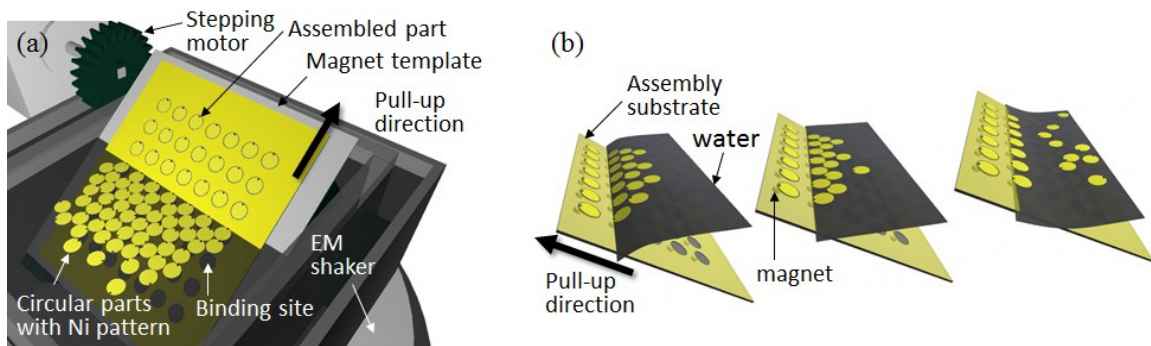


Figure 6.1: (a) Experimental setup. (b) Three steps for assembly; part approach, flat surface/registration and assembly.

6.3 Optimization of part rotation

6.3.1 Assembly performance

Today's pick-and-place machines (e.g., Assembléon's A-Series Hybrid) with 6 to 20 robotic arms assemble 1.7 components per second (cps) per robotic arm [35, 36]. The proposed FSA system assembles thin parts (100 μm thick) row-by-row. One-to-one part-to-site registration for each row is achieved using 20 s of Faraday waves. The application of Faraday waves can be minimized by employing visual feedback to check whether the desired registration is achieved. The FSA system with controlled Faraday waves assembles 90 parts in one minute (1.5 cps). The assembly rate can be further increased by expanding the horizontal dimension of an assembly substrate with more binding sites and floating parts.

Compared to our previous work with square parts [16], the assembly rate increases from 0.5 to 1.5 cps due to reduced part-to-part interactions. Parts at an air-water interface attract each other due to their matching sidewall wettability. The part-to-part interaction F_{pp} is determined using

two identical parts and two magnets (Figure 6.2). First, the maximum distance x_{max} at which Part 2 separates from Part 1 ($|F_{m2}| > |F_{m1} + F_{pp}|$) is experimentally determined. At $x = x_{max}$, the magnetic forces on Part 2 (F_{m1} and F_{m2} by two magnets m_1 and m_2) are simulated using COMSOL Multiphysics. Then, $F_{pp} = |F_{m2}| - |F_{m1}|$ is calculated. The part-to-part attraction forces are determined to be 3.6 and 1.4 μN for square and circular parts, respectively.

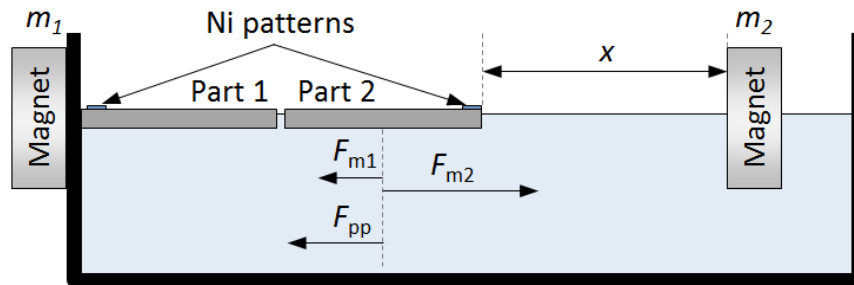


Figure 6.2: Test setup for determination of part-to-part interaction (attraction forces).

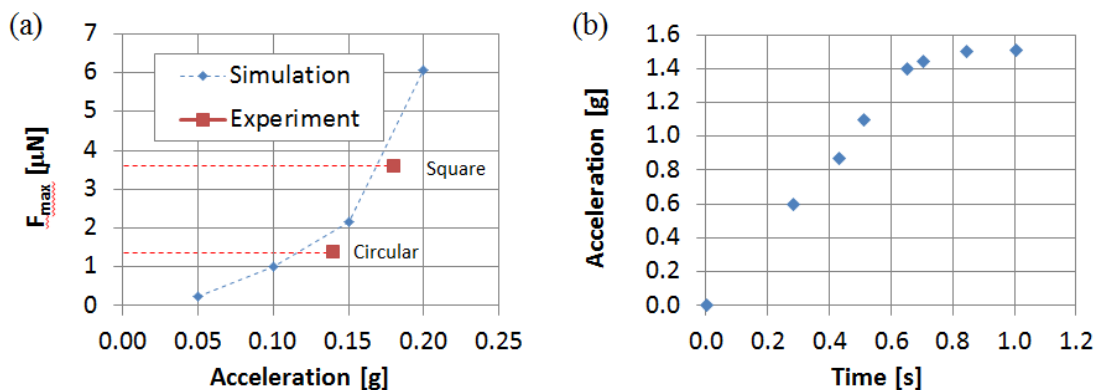


Figure 6.3: (a) Simulation and experimental results of the maximum force on a moving part on Faraday waves. Gravity and drag force are considered. (b) Transient response of the Faraday waves (80 Hz / 1.5 g).

Then, the minimum acceleration of Faraday waves to break part-to-part contact is determined through simulation using Matlab code (Figure 6.3(a)). The frequency is optimized for 1 mm parts [16] and still works for 2 mm parts. When Faraday waves are applied, the parts at the air-water interface are set in motion, making and breaking contact with other parts. The experimentally determined minimum accelerations for separation are 0.18 g (square) and 0.14 g (circular), which

are around 13 % higher than the simulation results (0.17 g (square), 0.12 g (circular)). Figure 6.3(b) shows the transient response of the Faraday waves. After applying an input signal, a desired g value (1.5 g) is observed at 0.8 s after a linear increase. Thus circular parts need less time for separation. In addition, wrongly oriented parts near the binding sites need to be corrected by Faraday waves before substrate pull-up [16]. The circular parts are more easily corrected due to their shape while the square parts need to be repelled before correction by 90° or 180° rotation.

As a result, for circular parts, the combined effect of the lower part-to-part interaction, the transient response of the Faraday waves, and the circular shape reduces agitation time for one-to-one part-to-site registration (13.5 to 4.7 s).

6.3.2 Part rotation in a binding site

NdFeB magnets are placed underneath every binding site. To maximize the force that attracts parts, the center of a magnet is aligned to the top of the circular binding site. However, test results in Figure 6.4 show a wide range of rotation angles of assembled parts. The angles are measured by placing lines from the Ni pattern to the center of each part on the image. A measured standard deviation and range are 25.5° and $\pm 40^\circ$. The leftmost and rightmost parts rotate CCW and CW, respectively (Figure 6.4 (a)). Three distinct groups are observed (Figure 6.4 (b)). For analysis, the magnetic field is simulated in the following section.

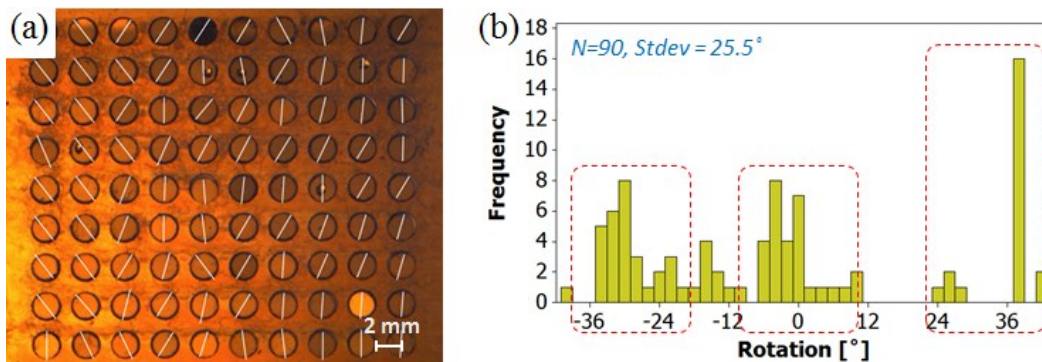


Figure 6.4: Assembly results before shifting magnets. (a) Parts are generally oriented upward but have wide deviation. (b) The distribution of orientations shows three distinct groups.

6.3.3 Optimization

Magnetic fields are simulated using COMSOL Multiphysics™ to analyze their effects on part rotation (Figure 6 5). Two surfaces in parallel with the y -axis (left and right side in Figure 6 5(a)) are set as repeating boundaries and the others are set as open boundaries.

A thin Ni pattern ($400 \times 400 \times 5 \mu\text{m}^3$), a ferromagnetic material, aligns along magnetic flux lines.

The magnets are axially magnetized and have poles on their top and bottom faces. Hence, the z -directional component of the magnetic field dominates the part approach process (Figure 6.1(b)) by attracting the Ni pattern more effectively than the in-plane (x - y) components.

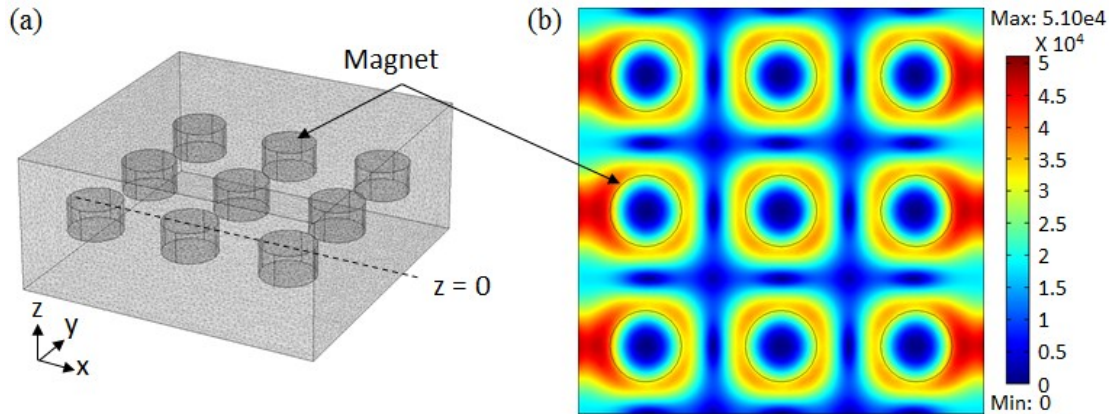


Figure 6.5: Simulation of the in-plane magnetic fields [A/m]. (a) The top surface of the magnets are set at $z = 0$. (b) In-plane (x - y) components of magnetic fields at $z = 0.5$ mm where assembly occurs.

In contrast, the in-plane magnetic field dominates rotation of parts after assembly. A Ni pattern is attracted and held at the center of a magnet throughout the assembly process. However, the process is easily disturbed by the inevitable variations (magnet/binding site alignment, gap between a Ni pattern and a magnet, and non-uniform surface properties). Once a Ni pattern is dislocated from the center of a magnet, the in-plane magnetic field gradient causes a force, which causes the circular parts assembled in a $70 \mu\text{m}$ deep binding site to rotate.

The in-plane magnetic forces on the Ni patterns before and after shifting of the magnets are simulated at various rotation angles (Figure 6.6). Before shifting the magnets, the minimum force is observed near 40° , where the Ni pattern experiences the highest in-plane magnetic flux density (Figure 6.6(a)), corresponding to the experimental maximum rotation angle. The plot of the magnetic fields indicates that part rotation can be minimized if a Ni pattern experiences the maximum in-plane magnetic field at rotation angle of 0° . After shifting the magnets upwards by 0.8 mm in the y direction (Figure 6.6 (b)), a simulated magnetic force at 20° has a component that acts as restoring force. The tendency of the parts in the leftmost and rightmost columns to rotate outwards can also be minimized by shifting the magnets upwards. Another assembly experiment is performed with the shifted magnets (Figure 6.6), verifying the simulations by reducing the angular deviation from 25.5° to 3.7° , as shown in Figure 6.7.

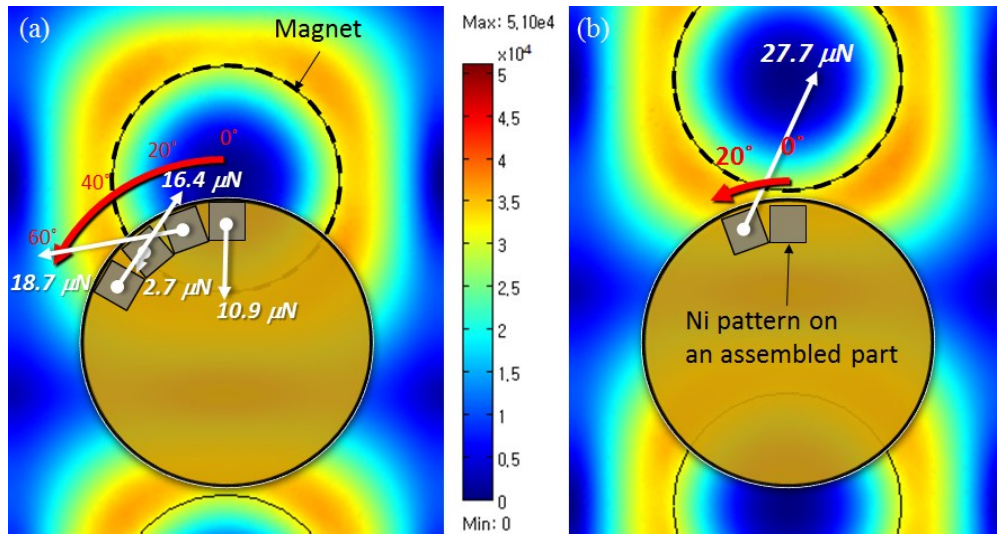


Figure 6.6: Minimization of part rotation by shifting magnets by 0.8 mm. In-plane magnetic field and magnetic forces (a) before and (b) after shifting magnets.

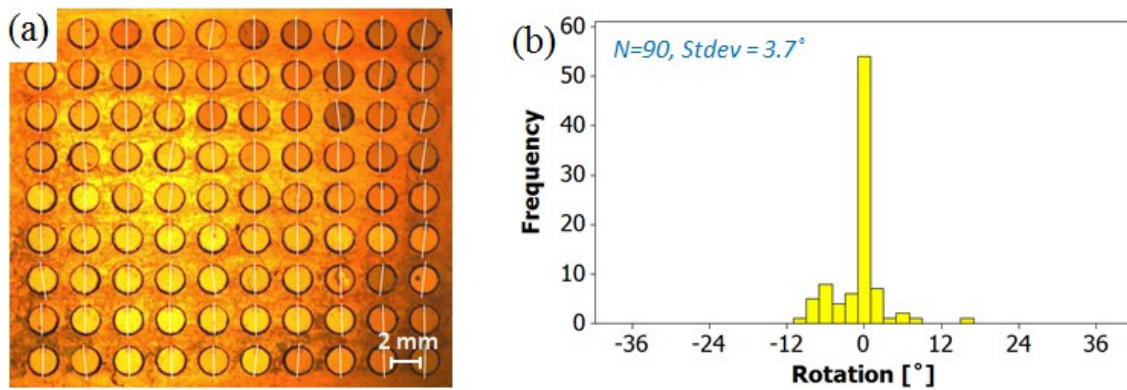


Figure 6.7: Assembly results after shifting magnets. (a) Orientation-specific assembly of 90 parts with less deviation. (b) Distribution has a standard deviation of 3.7°

6.4 Conclusions

Orientation-specific self-assembly of Ni patterned thin, circular parts using magnetic fields is demonstrated and optimized. The angular deviation is improved from 25.5° to 3.7° by shifting the position of the magnet template.

The proposed FSA system achieves an assembly rate of 1.5 components per second, which is comparable to that of today's pick-and-place assembly robots. The experimental result shows that less interaction between parts increases the assembly rate.

CHAPTER 7. EFFECT OF VISCOSITY

7.1 Introduction

Due to the increasing demand for cost-effective and value-added systems with small form factors, miniaturization for functional densification is being done with smaller and thinner parts. However, thin parts with low aspect ratios are particularly fragile when exposed to high accelerations and point forces in the assembly process.

Self-assembled structures in nature have inspired modern research in engineered self-assembly at the nano-to-millimeter scale [1, 2] to replace traditional manufacturing methods. Industry and research groups have developed self-assembly strategies [1, 2, 9-11, 18-22]. For example, Alien Technology (Morgan Hill, CA) has commercialized fluidic self-assembly (FSA) to assemble radio frequency (RF) chips across large plastic substrates based on shape matching [37, 38]. Throughout Chapter 2 to Chapter 4, our FSA method was improved to assemble thin parts in unique orientations by adding a Ni pattern on parts and magnets underneath each binding site.

The detailed motion of objects suspended in fluids with different viscosities has been extensively studied by many groups [39]. For FSA, velocity change of moving parts [38] and the effect of viscosity are briefly mentioned in [37, 40]. However, to our knowledge, detailed studies of the effect of viscosity on self-assembly processes or yields have not been undertaken. Here, we investigate in detail the effects of viscosity on the assembly processes, assembly speed, and yield of our FSA using a newly derived modeling equation, experimental results and analysis.

7.2 Fluidic self-assembly strategy

7.2.1 FSA system setup

The same orientation-specific FSA system described in Chapter 4 is used for experiments (Figure 7.1). The substrate is tilted at a 45° angle with the water surface and pulled up by the stepper motor at a speed of 0.415 mm/s. Accurate magnet-binding site alignment is achieved using a photolithographically patterned “magnet template”. Then the magnet template is placed under the substrate.

7.2.2 Assembly process

A 2 mm sized Si part has a hydrophobic surface (SAM -coated Au) and a hydrophilic Si oxide surface. To utilize the interfacial capillary force between a part and a hydrophilic Si oxide binding site, the Si oxide side should face down. To orient all the parts in the same direction, the face-orienting process in [41] is used. After 1.5 min shaking of a container with parts at an air-water interface at 300 rpm, all floating parts have their hydrophilic Si oxide surfaces facing downwards (the only stable state on an agitated water surface).

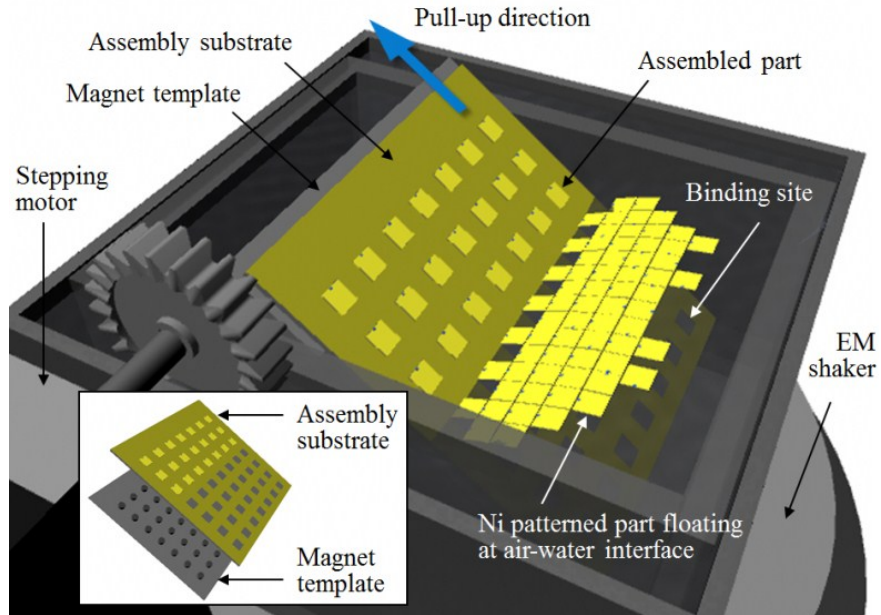


Figure 7.1: The experimental setup consists of a water container, a linear electromagnetic vibration table, a stepper motor, an assembly substrate, magnets and parts floating at the air-water interface.

The assembly proceeds row-by-row as the substrate is pulled up through an air-water interface. Most parts approach the binding sites with the orientation due to a magnetic field. Wrongly oriented parts are corrected by Faraday waves and the parts are assembled by substrate pull-up. In the assembly, two major processes, approach and rotation, are affected by the viscosity of the liquid medium (water).

7.2.2.1 Approach

Standing wave patterns in a layer of liquid enclosed by a vibrating container are known as Faraday waves. In our FSA system, the Faraday waves are generated using a vertical electromagnetic shaker driven at 80 Hz/1.5 g. The Faraday waves are applied to prevent multiple parts from approaching one binding site.

The parts at the air-water interface approach the substrate in unique orientation due to the presence of downward menisci, and magnetic fields (Figure 7.2(a)). The magnetic fields of rare-earth neodymium iron boron (NeFeB, Grade N40) magnets help the part to approach Ni-patterned side first. The motion of the parts is affected by the viscosity.

7.2.2.2 Registration

Although the Faraday waves and the magnetic field help the parts to approach the binding sites, a binding site can be empty, or be occupied by wrongly oriented parts due to the stochastic property

of the approach process. Faraday waves rearrange the wrongly oriented parts at 90° or/and 180° and achieve one-to-one part-to-site registration. The rotational motion of the parts at the air-water interface depends on the viscosity of water that affects the viscous resistance (i.e., drag force).

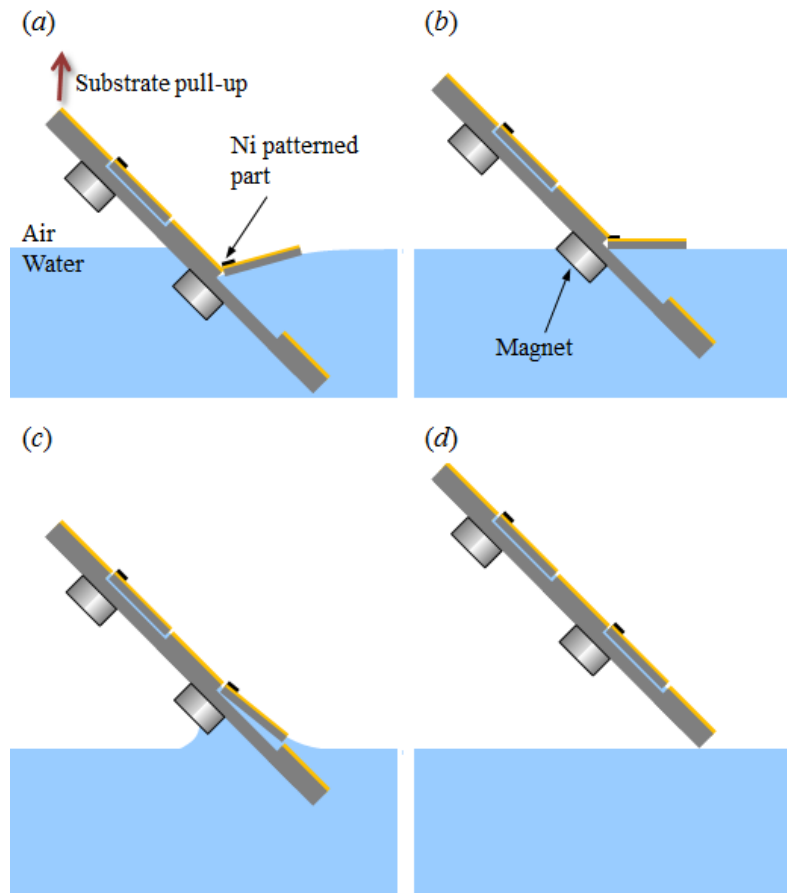


Figure 7.2: Full assembly process flow. (a) Parts approach the substrate driven by downward meniscus and magnetic field and (b-d) are assembled by substrate pull-up.

7.2.2.3 Pull-up

Once the one-to-one part-to-site registration is achieved, the parts are assembled by substrate pull-up (Figure 7.2(b) to (d)). If the magnetic forces on the parts are strong enough to hold the parts, said parts are captured in the trenches. Although the contact angle between a tilted assembly substrate and water (i.e., the shape of meniscus) is determined by pull-up speed and viscosity [29], the shape of the meniscus is time-independent for small pull-out speed [30] and the assembly is dominated by magnetic force. Therefore, we assume the pull-up process is quasi-static and viscosity-independent.

As the assembly for one row is completed, a water-substrate contact line slips down over a hydrophobic SAM-coated Au surface and pins to the next row, which changes the shape of the meniscus from upward to downward and initiates a part approach process for the next row.

7.3 Effect of viscosity

In this section, the two major viscosity-dependent assembly process steps, approach and registration (90°, 180° rotation), are described. These steps are based on the motion of the parts on a water surface, which is affected by fluid viscosity.

The viscosity of water is known to decrease rapidly with increasing temperatures [42]. Three temperatures that vary the viscosity of water over a wide range (0.9548 to 0.4665 mPa·s) are selected for tests (Table 7.1). Then, the viscosity dependence of approach time, 90°/180° rotation time, assembly speed and yield are analyzed. The temperature is controlled within ± 2 °C using a resistive heating tape (HTS/Amptek Co., ASR-051-020D).

Table 7.1: Selected viscosities. The viscosity of water decreases to approximately half, as temperature increases from 22 to 60 °C. The temperature is controlled by a heating tape.

Temperature [°C]	Viscosity [mPa·s]
22 (room temp.)	0.9548
40	0.6592
60	0.4665

7.3.1 Approach

The motion of Ni patterned parts at an air-water interface is affected by drag forces, also known as viscous resistance. A part with a ferromagnetic Ni pattern is accelerated along the magnetic field. Therefore, a drag constant and magnetic force for each viscosity should be determined to describe the motion of the part in the FSA system.

In this section, the equation of a moving part is derived. Then, a drag constant and magnetic force on the moving part are experimentally and analytically determined. Finally, the effect of viscosity of water on approach time is analyzed.

7.3.1.1 Forces on a part

Unlike the standard surface friction, a drag force (i.e., viscous resistance) is velocity-dependent. The Reynolds number ($Re = \rho VL/\mu$, where ρ , V , L , μ are the density, mean velocity, characteristic length, and dynamic viscosity of a fluid, respectively) is a dimensionless number that presents the

ratio of inertia forces to viscous forces [43, 44]. At a low velocity where there is no turbulence (i.e., low Reynolds number, $Re < 1$, calculated $Re \approx 0.2$), a drag force F_d on the part at the air-water interface is approximately proportional to velocity and can be expressed using Stokes' drag equation (6.1), where b is the linear drag constant and v is the velocity of a part. The moving part experiences a drag force in opposite direction of velocity. According to the equation for Stokes' drag, a drag constant b for a spherical part moving slowly through a viscous fluid can be approximated by $6\pi\eta r$ (η : fluid viscosity, r : radius). However, since the part has a thin square shape and floats at a fluid interface, we design an experiment to determine b (Figure 7.3(a)).

$$F_d = -bv \quad (6.1)$$

If the forces on a moving part are magnetic force (F_m) and drag force (F_d), the motion of the part with mass m can be described by equation (6.2) (Newton's second law of motion). The magnetic force F_m is not constant but inversely proportional to the square of the distance from the magnet and proportional to the volume of the Ni pattern.

$$m \frac{dv}{dt} = F_m + F_d = F_m - bv \quad (6.2)$$

Equation (6.3) is derived from equation (6.2) and presents exponential change in the velocity of a moving part over time with an initial velocity v_i . Two unknown parameters, a linear drag constant b and magnetic force F_m , are experimentally determined in the following two sections.

$$v(t) = \frac{F_m}{b} - \left(\frac{F_m}{b} - v_i \right) e^{-\alpha t} \quad (\alpha = b/m) \quad (6.3)$$

7.3.1.2 Drag constant

A drag constant b is experimentally estimated using the setup in Figure 7.3(a). A part is released on a leveled water surface with a non-zero initial velocity v_i . For the setup in Figure 7.3(a), equation (6.3) is simplified into equation (6.4) and the drag constant b can be determined by observing the exponential decrease in velocity over time.

$$v(t) = v_i e^{-\alpha t} \quad (6.4)$$

The drag constant b at 22°C is determined to be 1.88×10^{-6} N/(m/s) through fitting equation (6.4) to the observed data (Figure 7.4) using a known initial velocity v_i and mass m . At low Reynolds number Re (where viscosity dominates fluid flow), a drag force is proportional to the viscosity of water. Thus, the drag constants at 40 and 60 °C (Table 7.2) are calculated using temperature-dependent viscosities.

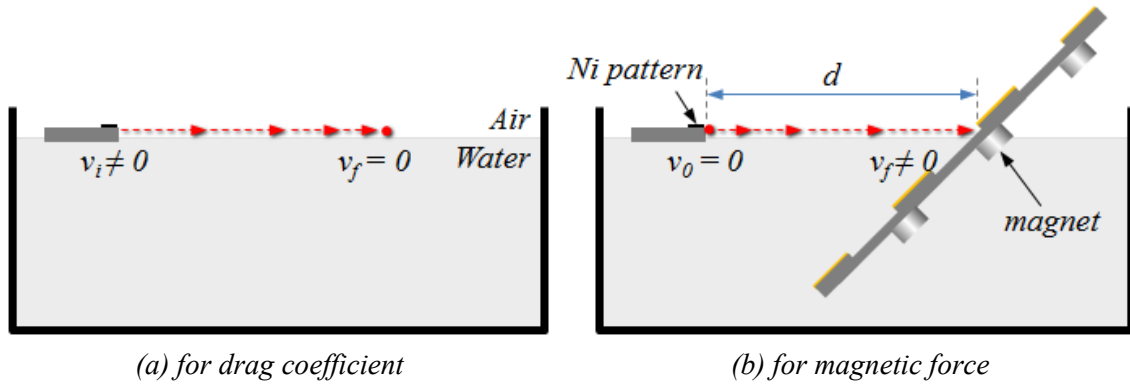


Figure 7.3: Experimental setup to evaluate (a) a drag coefficient and (b) acceleration along the magnetic field ($d = 22$ mm).

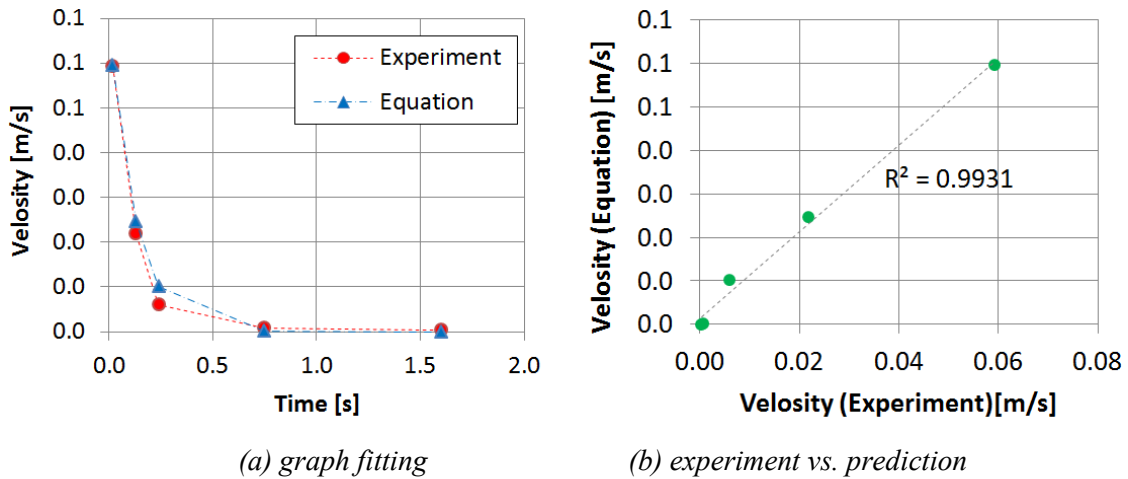


Figure 7.4: Extraction of a drag constant through graph fitting at 22°C . The equation with a drag constant $b = 1.88 \times 10^{-6}$ N/(m/s) fits the exponentially decreasing velocity.

Table 7.2: Drag coefficients of water at different viscosities. The drag coefficients at 0.6592 and 0.4665 mPa·s are calculated using the experimentally obtained result at 0.9548 mPa·s.

Viscosity [mPa·s]	Drag coefficient, b [N/(m/s)]
0.9548	$1.88\text{e-}6$
0.6592	$1.28\text{e-}6$
0.4665	$9.18\text{e-}7$

7.3.1.3 Magnetic force and approach time

In addition to the drag constant b , the magnetic force F_m needs to be determined to describe the detailed motion of a part in an approach process in a magnetic field. The magnets in the FSA system attract Ni patterned parts in the specific orientation as well as accelerate them.

Now, we use the setup in Figure 7.3(b). A part with a zero initial velocity v_i begins to move towards a binding site by the magnetic field. With $v_i = 0$, the equation (6.3) becomes equation (6.5), which describes the accelerated motion of a part. Equation (6.6), which describes travel distance at time t , is derived from equation (6.5).

$$v(t) = \frac{F_m}{b} (1 - e^{-\alpha t}) \quad (6.5)$$

$$d(t) = \frac{F_m}{b} \left(t + \frac{1}{\alpha} e^{-\alpha t} \right) - \frac{F_m}{b} \frac{1}{\alpha} \quad (6.6)$$

In the experiments, F_m is not constant but increases as the Ni patterned part approaches the binding sites. Thus, for comparison, effective magnetic forces $F_{m,eff}$ at different viscosities are experimentally determined using equation (6.6) with known travel distance ($d = 22$ mm), the viscosity-dependent drag constant b and measured approach time. Table 7.3 shows the approach time (experiment) and viscosity-independent $F_{m,eff}$ (calculated using experiment). Figure 7.5 and Figure 7.6 clearly show linear dependence of approach time on fluid viscosity. Increased viscosity decreases the speed of moving parts.

Table 7.3: Approach time ($d = 22$ mm) at different viscosities. Effective magnetic force $F_{m,eff}$ is calculated to be $4.63 \mu\text{N}$ at all viscosities. For statistical analysis, all experiments are repeated 30 times.

Viscosity [mPa·s]	Approach time [s]	Effective magnetic force, $F_{m,eff}$ [μN]
0.9548	9.44	4.62
0.6592	6.59	4.63
0.4665	5.40	4.63

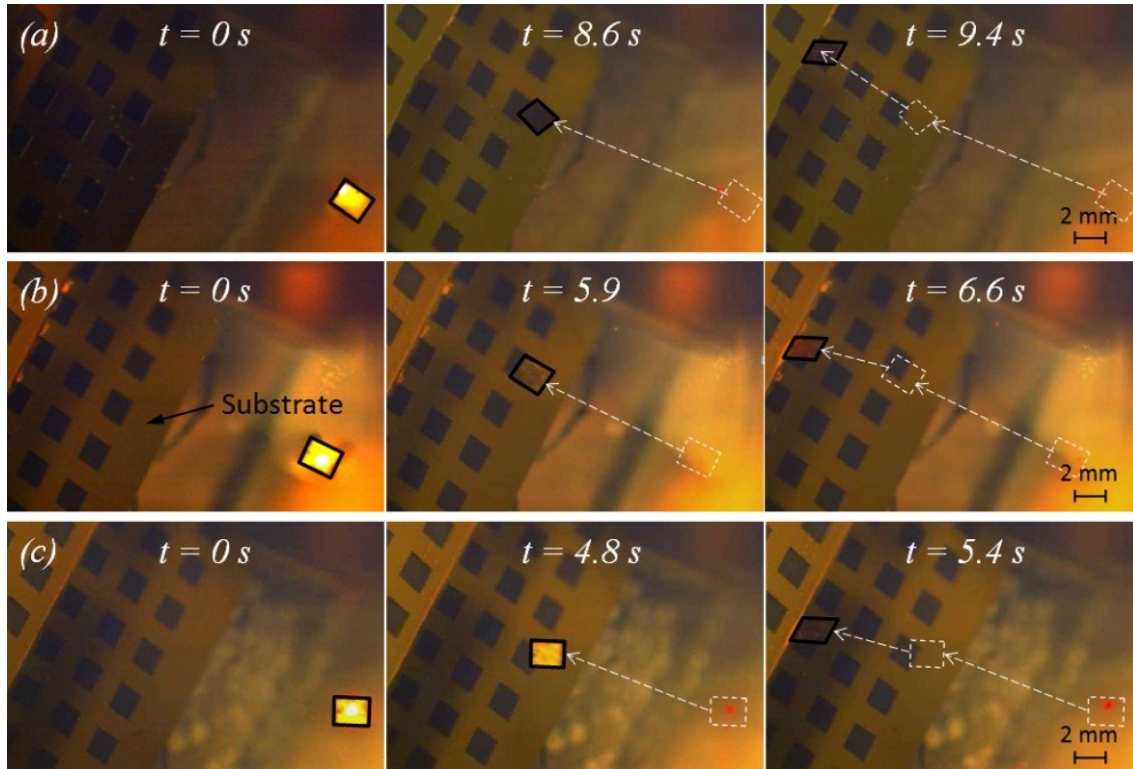


Figure 7.5: Part approach at different viscosities. Parts ($2000 \times 2000 \times 100 \mu\text{m}^3$) are highlighted by solid lines. The parts are accelerated towards the substrate by the magnetic field. The initial velocity of a part is 0. (a) $0.9557 \text{ mPa}\cdot\text{s}$, (b) $0.6531 \text{ mPa}\cdot\text{s}$ and (c) $0.4668 \text{ mPa}\cdot\text{s}$.

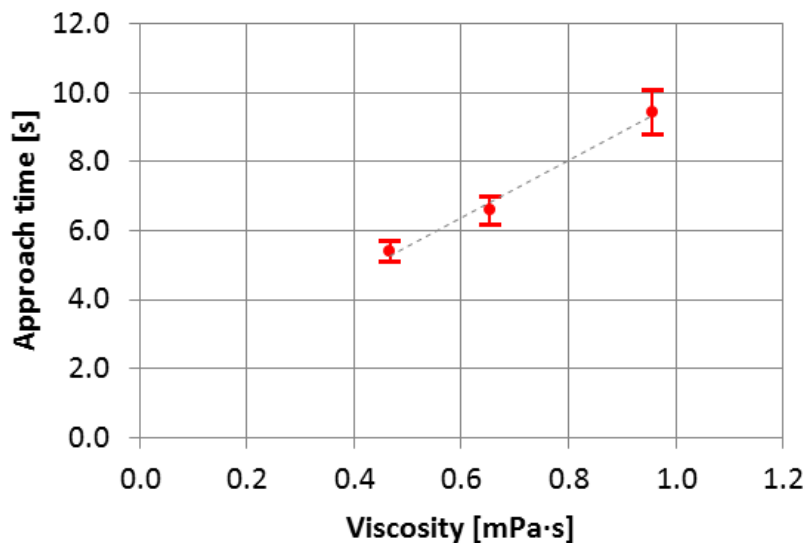


Figure 7.6: Approach time vs. viscosity. The approach time increases proportionally to the viscosity. 95 % confidence intervals are indicated.

7.3.1.4 Rearrangement (90° or 180° rotation)

The parts are expected to approach the substrate with the correct angular orientation due to the magnetic field. However, that is not always the case due to the stochastic properties of the part movement. One-to-one part-to-binding site registration with unique orientation is necessary to achieve high yield.

In order to achieve the desired registration, wrongly oriented (90°, 180°) parts on binding sites should be rearranged. These parts experience weaker magnetic forces due to the increased distance between Ni patterns to magnets. Thus, the parts can be rearranged by temporary Faraday waves.

In the previous section, the linear relationship between the viscosity and approach time is described. The rotation of a part (90°, 180°) also occurs on the water surface, so we can hypothesize a similar linear relationship in the rearrangement process. However, only 90° rotations show a linear relationship with a change in viscosity, while 180° rotations do not. Table 7.4 and Figure 7.7 summarize the experimental results. Parts rotating 180° have higher velocity than 90° because Faraday waves accelerate the parts [45]. The viscosity dependence of 90° and 180° rotations is detailed in the following sections.

Table 7.4: Summary of experimental results. 90° rotation time shows a clear linear dependence on viscosity while 180° rotation time does not. For statistical analysis, all experiments are repeated 30 times.

Water viscosity [mPa·s]	Part angle [°]	Travel distance [mm]	Rotation time [s]	Travel velocity [m/s]
0.9548		4.7	0.68	6.84
0.6592	90	5.8	0.52	11.16
0.4665		5.1	0.30	16.64
0.9548		16.8	1.98	8.46
0.6592	180	30.8	2.27	13.57
0.4665		44.0	2.15	20.48

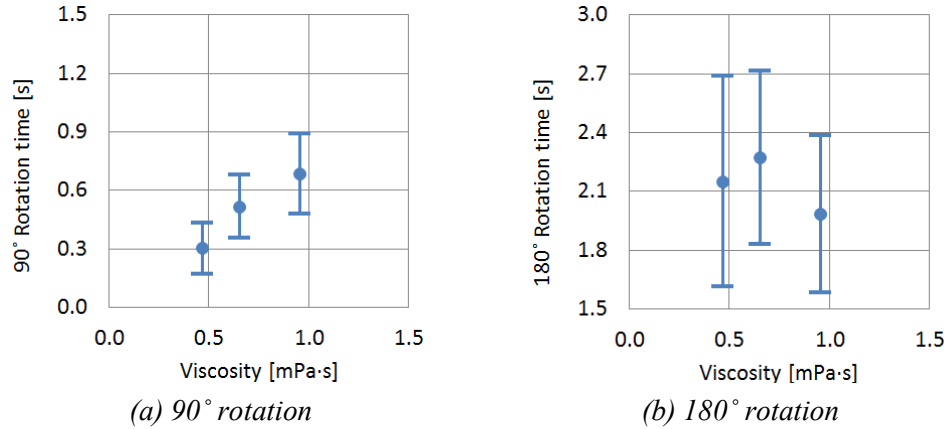


Figure 7.7: Rotation time vs. the viscosity of water. (a) 90° rotation and (b) 180° rotation. The 95% confidence intervals for the means are presented. 30 data are used at each viscosity.

7.3.1.5 90° rotation

The 90° rotation time shows a strong linear relationship with viscosity (Figure 7.7(a)). Thus, we hypothesize that the linear relationship is primarily due to the viscosity-dependent travel velocity. To verify the assumption, we intentionally select three experimental results (one from each viscosity) that have similar travel distances (Figure 7.8(a)). The analysis in Table 7.5 reveals a linear relationship between the travel velocity and the viscosity. Therefore, it is concluded that fluid viscosity dominates 90° rotation time.

The magnetic force on the parts rotating 90° is not strong enough to assemble the parts but still strong enough to hold the part. So, the parts are bounded to the substrate and rotate near their corresponding binding sites. Thus, the parts have smaller travel distances with a narrow deviation.

7.3.1.6 180° rotation

In contrast with 90°, 180° rotation time does not have a clear relationship with the fluid viscosity (Figure 7.7(b)). The 180° rotation times at different viscosities are similar (1.98 to 2.27 s, Table 7.4) over the wide range of travel distance (16.8 to 44.0 mm). For analysis, three data at each viscosity, which have similar rotation time near 2.2 s, are selected.

Analysis results in Figure 7.8(b-d) and Table 7.5 indicate that lower viscosity increases both travel distance and velocity in 180° rotation. Thus, 180° rotation time becomes less sensitive to the viscosity.

The increased travel distances, compared to 90° rotation, are mainly due to reduced magnetic forces, which are too weak to hold the part. The parts escape from the immediate vicinity of the binding sites as soon as Faraday waves are applied, and randomly travel around. While traveling, if a part experiences a magnetic force strong enough to attract it, it then approaches the binding

site. Thus, 180° rotation is usually completed after traveling a longer distance and its uncertainty produces a wider deviation than that of 90° rotation.

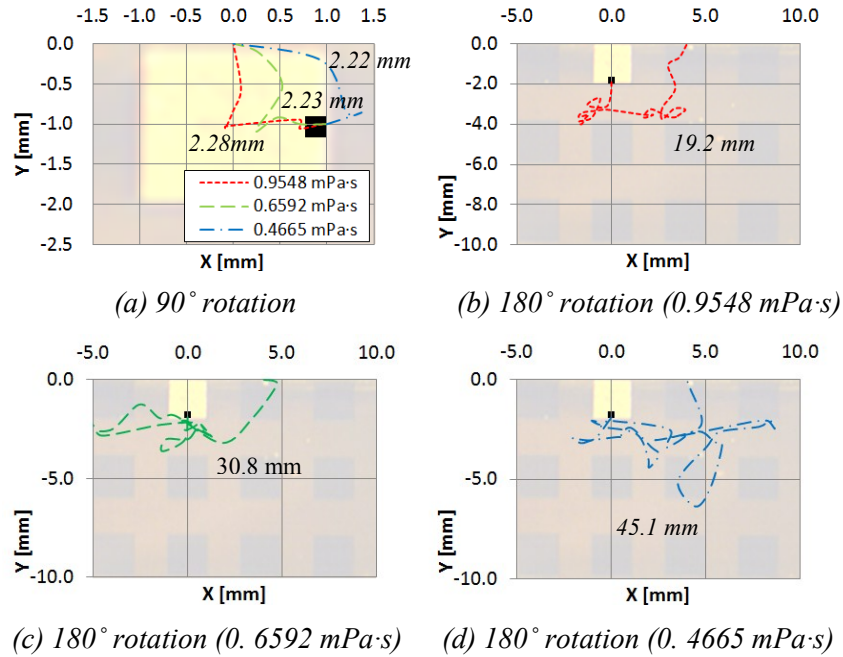


Figure 7.8: Trajectories of Ni patterns on wrongly oriented parts ($2000 \times 2000 \times 100 \mu\text{m}^3$) at air-water interface. Ni patterned parts in background shows their initial orientation. (a) 90° rotation. (b-d) 180° rotation.

Table 7.5: Selected results from each viscosity. 90° rotation time shows a clear dependence on the viscosity of water while 180° rotation time does not.

Water viscosity [mPa·s]	Part angle [°]	Travel distance [mm]	Rotation time [s]	Travel velocity [m/s]
0.9548		2.3	0.33	6.91
0.6592	90	2.2	0.20	11.15
0.4665		2.2	0.13	17.08
0.9548		19.2	2.27	8.45
0.6592	180	30.8	2.27	13.54
0.4665		45.1	2.15	20.96

7.3.2 Assembly yield and speed

The combined effect of approach and rearrangement process determines assembly yield and speed. The assembly proceeds row-by-row as the substrate is pulled up through an air-water interface. Virtually 100 % yield is achievable when employing visual feedback to achieve one-to-one part-to-binding site registration before substrate pull-up. In the following section, the effect of viscosity on assembly performance (yield and speed) with and without feedback is studied.

7.3.2.1 Yield without feedback

In this test, Faraday wave (80 Hz, 1.5 g) are applied for 7 s at each row. The 7 s application of Faraday waves is selected because the test results (rate constant in Table 7.6) with and without feedback control are similar at room temperature. The effect of feedback control is analyzed by comparing assembly speeds at lower viscosities in the following section. After applying 7 s of Faraday waves, the substrate is pulled up at a constant speed of 0.415 mm/s. Thus, the substrate-level assembly takes 109 s regardless of the fluid viscosity.

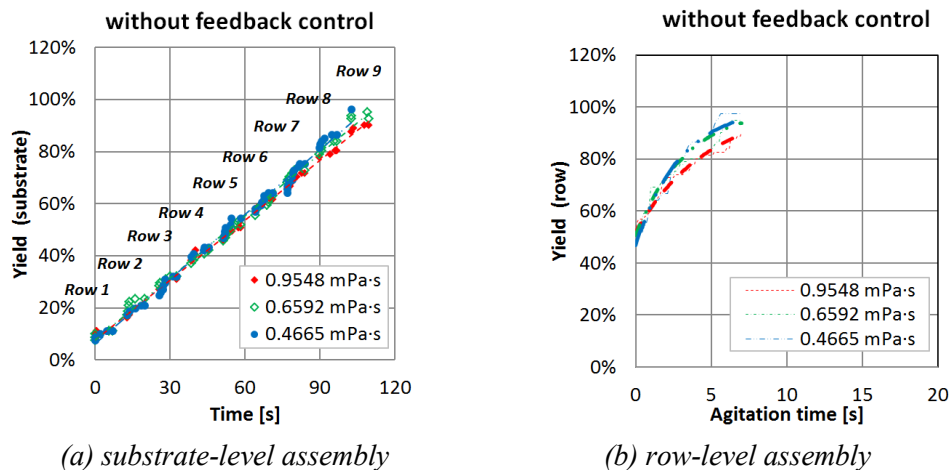


Figure 7.9: Assembly result without feedback. Higher yield is observed at lower viscosity. Row-level yield does not reach 100 % with 7 s of agitation. (a) substrate-level and (b) row-level yield.

The assembly substrate consist of 9×9 binding sites. Nine subgroups (Row 1 to 9) make a macroscopic linear increase in substrate-level yield over time (Figure 7.9(a)). At lower viscosity, parts approach and/or rotate at higher speed and increase chances for registration. As a result, higher yield is obtained at lower viscosity as shown in Table 7.6.

The average yield of nine subgroups delivers row-level yield in Figure 7.9(b). Due to the limited

agitation time (7 s), each row hardly achieves 100 % one-to-one part-to-binding site registration and does not reach 100 %. The row-level yield is modeled using the exponential equation (6.7) described in the next section.

7.3.2.2 Yield with feedback

For an assembly test with feedback, the Faraday waves (80 Hz, 1.5 g) are applied for each row until 100 % one-to-one part-to-binding site registration is visually observed. Then the substrate with 9×9 binding sites is pulled up at a constant speed of 0.415 mm/s until the assembly at the next row starts. The application of the Faraday waves and the substrate pull-up are repeated for each row.

Figure 7.10(a) shows high yield (100 %) assembly with feedback control. Like the assembly without feedback, higher assembly speed is obtained at lower viscosity. Nine subgroups (Rows 1 to 9) at each viscosity are averaged to describe how the yield increases over time (Figure 7.10(b)). For each row, the yield exponentially increases over time and reaches near 100 % at 20 s.

The row-level yield is successfully modeled using the exponential equation (6.7) where r is a rate constant that controls assembly rate and y_0 is initial yield at $t = 0$. Non-zero initial yield y_0 is observed due to the several parts that are already registered on the binding sites before applying the Faraday waves at $t = 0$. The slope of exponential curve (i.e., assembly speed) is dominated by the viscosity-dependent rate constant r . The rate constant r values at each viscosity are extracted by fitting the equation to experimental results (Table 7.6).

$$yield(t) = (1 - y_0)(1 - e^{-rt}) + y_0 \quad (6.7)$$

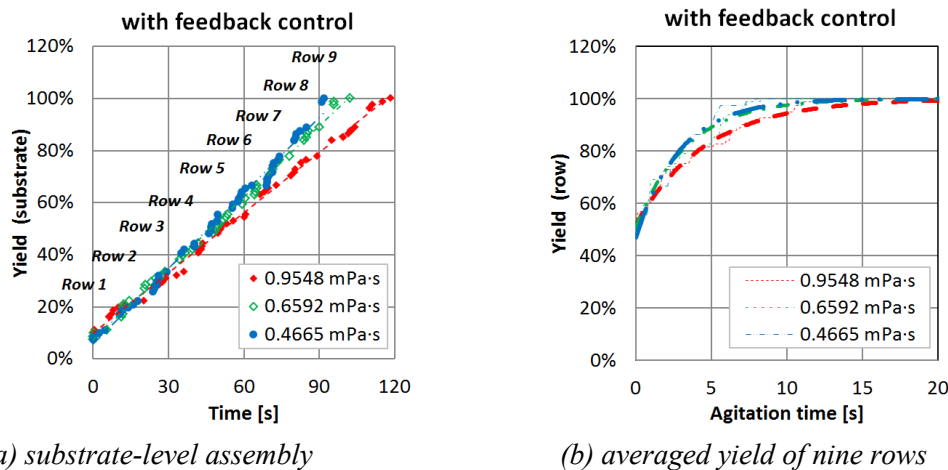


Figure 7.10: Assembly result with feedback. (a) substrate-level and (b) row-level yield. Higher yield is observed at lower viscosity. The row-level yield reach near 100 % with 20 s agitation.

Table 7.6: Summary of the effect of the viscosity on yield with and without feedback. Lower viscosity increases assembly yield as well as assembly speed. 100 % yield is achieved with feedback control.

Water viscosity [mPa·s]	Feedback	Yield [%]	Assembly speed [%/s]	Rate constant, r [1/s]
0.9548		90	0.78	0.21
0.6592	No	95	0.83	0.30
0.4665		98	0.85	0.34
0.6592		100	0.81	0.22
0.6592	Yes	100	0.93	0.30
0.4665		100	1.04	0.33

Figure 7.11 shows linear dependences of assembly speed on the viscosity both with and without feedback. The effect of feedback control becomes more significant as the fluid viscosity decreases. Decreased viscous resistance (i.e., increased travel velocity) reduces the approach time and the rearrangement time. Thus, assembly speed is significantly improved at lower viscosity with feedback control by applying Faraday waves for a time just enough to achieve proper registration.

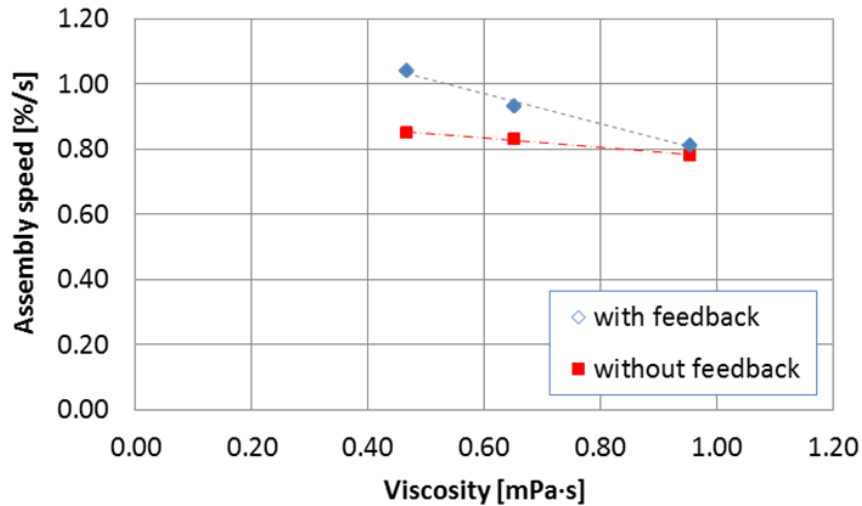


Figure 7.11: The dependence of assembly speed on the viscosity. The feedback control improves the assembly speed more effectively at lower viscosity.

7.4 Conclusion

Detailed studies on the effect of water viscosity (0.4665 to 0.9548 mPa·s) on fluidic self-assembly are conducted. The analysis results indicate drag force (i.e., viscous resistance) dominates part approach and registration process. As a result, it affects assembly speed, yield and the effect of feedback control.

Firstly, approach time is found to be dominated by viscous drag force, which is proportional to viscosity. Thus, the experiments show a linear relationship between viscosity and approach time.

Secondly, the registration process by 90° and 180° rotation is studied. The travel distances in 90° rotation do not change significantly due to the magnetic force, which is strong enough to hold the parts near the assembly substrate. Thus, 90° rotation occurs near the binding sites. The viscous resistance affects only the velocity and shows a linear relationship with the 90° rotation time. In contrast, the travel distance of 180° rotating parts increases with decreasing viscosity. The magnetic forces on these parts are too weak to hold the parts. Thus, the parts are not bounded to the assembly substrate and easily repelled away and travel around as Faraday waves are applied. The combined effect of travel distance and velocity makes the 180° rotation time less dependent on the viscosity.

Thirdly, a viscosity dependence of assembly speed is studied. Lower viscosity achieves higher assembly speed in both tests with and without feedback control. In the test without feedback control, higher assembly yield is achieved at lower viscosity. It is due to the increased velocity of the parts, which have more chances to approach the binding sites with the correct orientation. Row-level assembly speed is also described using an exponential equation. The equation indicates 20 s of agitation before substrate pull-up guarantees near 100 % high yields.

Finally, the effect of feedback control is experimentally proven. The assembly with feedback control includes Faraday waves for a time just enough to achieve one-to-one part-to-binding site registration for each row. 7 s of Faraday waves are applied in the assembly without feedback control. The improvement in assembly speed by feedback control becomes more obvious at lower viscosity due to the decreased approach time, the registration time and the efficient use of Faraday waves.

CHAPTER 8. 3D INTEGRATION USING SELF-ASSEMBLY

8.1 Introduction

CMOS scaling, prevailing growth driven by a continuous reduction in cost per function cannot be sustained by miniaturization (More-Moore technology) alone. Assembly and packaging area is increasingly undertaking this responsibility, and it is doing so based on the principles of densification of the functions. Functional enrichment (More-than-Moore technology) [4] focuses on 3D integration rather than transistor density alone.

3D integration has advantages (less power consumption, higher performance, smaller area, lower cost and stacking multiple parts from different fabrication processes) over 2D integration and enables the extension of Moore's law and the delivery of smarter and cheaper electronics. Thus, 3D integration gains importance and is in use in some domains (cell phones and memory). Thinner components are preferred to maximize the benefits of 3D integration. However, since pick-and-place assembly of thin low-aspect-ratio parts becomes slow and difficult due to high forces from abrupt, conventional pick-and-place becomes costly and self-assembly is preferred.

Here, we present the first proof-of-concept 3D FSA of 2 mm sized parts (100 μm thick) with experimental data as one example of More-than-Moore technologies. The proposed FSA system achieves 3D integration by assembling parts on top of previously assembled parts.

8.2 Assembly process

8.2.1 Overview of FSA with unique orientation

A 3D FSA system (Figure 8.1) consists of a water container on a linear electromagnetic shaker (Brüel & Kjær Type 4809), a stepper motor (Soyo, SY42STH38-0406A) with the controller (Phidgets, 1062), an assembly substrate, a magnet template and parts floating at an air-water interface.

The substrate has preprogrammed hydrophilic binding sites and a self-assembled monolayer (SAM)-coated hydrophobic Au area. The substrate is tilted at an angle of 45° relative to the water surface. Test electrodes are patterned on the substrate to measure the resistance of through-silicon vias (TSVs) (Figure 8.1(b)). To attract Ni patterned parts in proper orientation, rare-earth neodymium iron boron magnets (NeFeB, Grade N40, diameter = thickness = 1/16 inch) are placed beneath each binding site. A magnet template is patterned using lithography and deep reactive ion etching (DRIE). Magnets are placed in magnet-sized trenches. Accurate magnet-binding site alignment is achieved by aligning the magnet template with the assembly substrate.

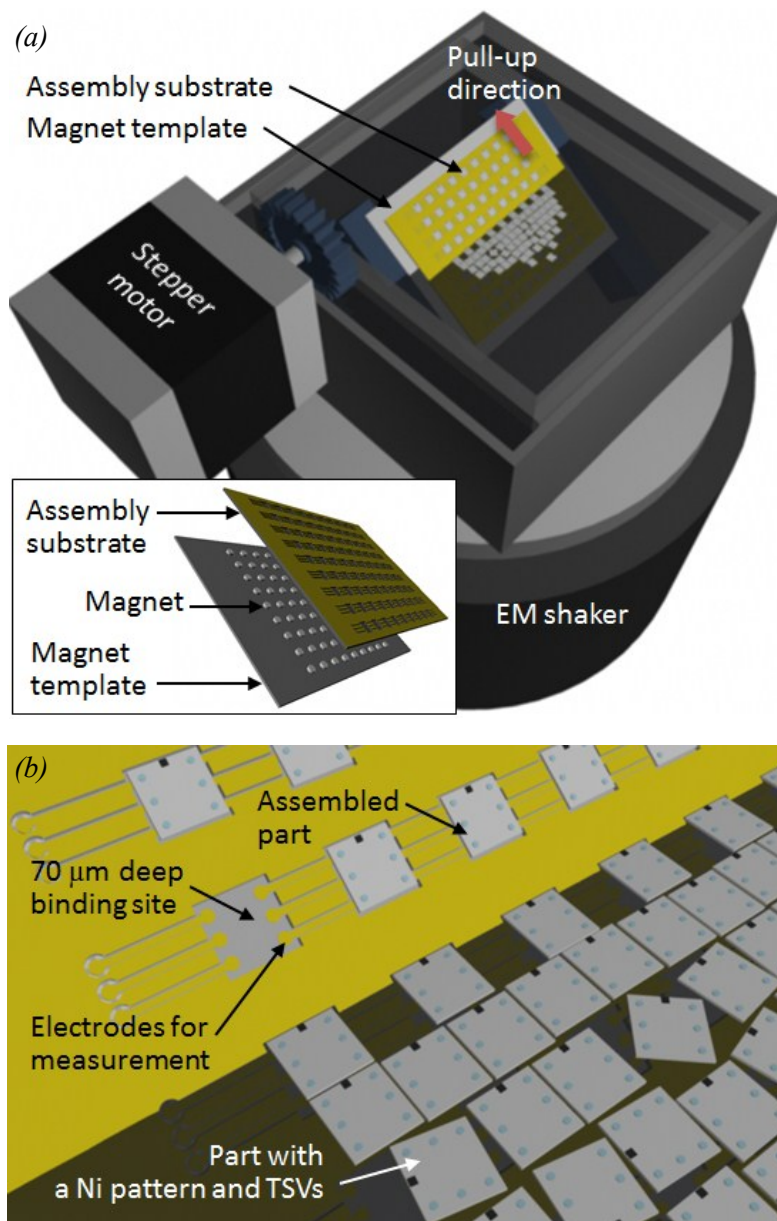


Figure 8.1: Assembly system. (a) Experimental setup for assembly consists of a water container on a linear electromagnetic shaker, a stepper motor with the controller, a substrate and parts floating at an air-water interface. (b) Design of parts and binding sites. Each part has six TSVs (diameter = 200 μm) and each binding site has six electrodes for electrical measurement.

Standing wave patterns in a layer of liquid enclosed by a vibrating container are known as Faraday waves [27, 28]. Typical yield loss in FSA is due to lack of control of one-on-one part-to-site registration. In the proposed FSA system, Faraday waves are generated by use of a vertical electromagnetic shaker driven at 80 Hz/1.5 g. We avoid multiple parts approaching the

same site and guarantee high yield by using the Faraday waves. Although most parts approach binding sites in proper orientation due to the magnetic field, it is possible that none, multiple or wrongly oriented parts occupy binding sites due to the stochastic character of the approach process. Faraday waves are applied to prevent multiple parts from approaching one site and to achieve one-to-one part-to-site registration in proper orientation as demonstrated in [17]. Correctly registered parts experience stronger magnetic force than wrongly oriented ones. Thus wrongly oriented or extra parts are selectively repelled by Faraday waves and other parts have a chance to approach the empty binding sites.

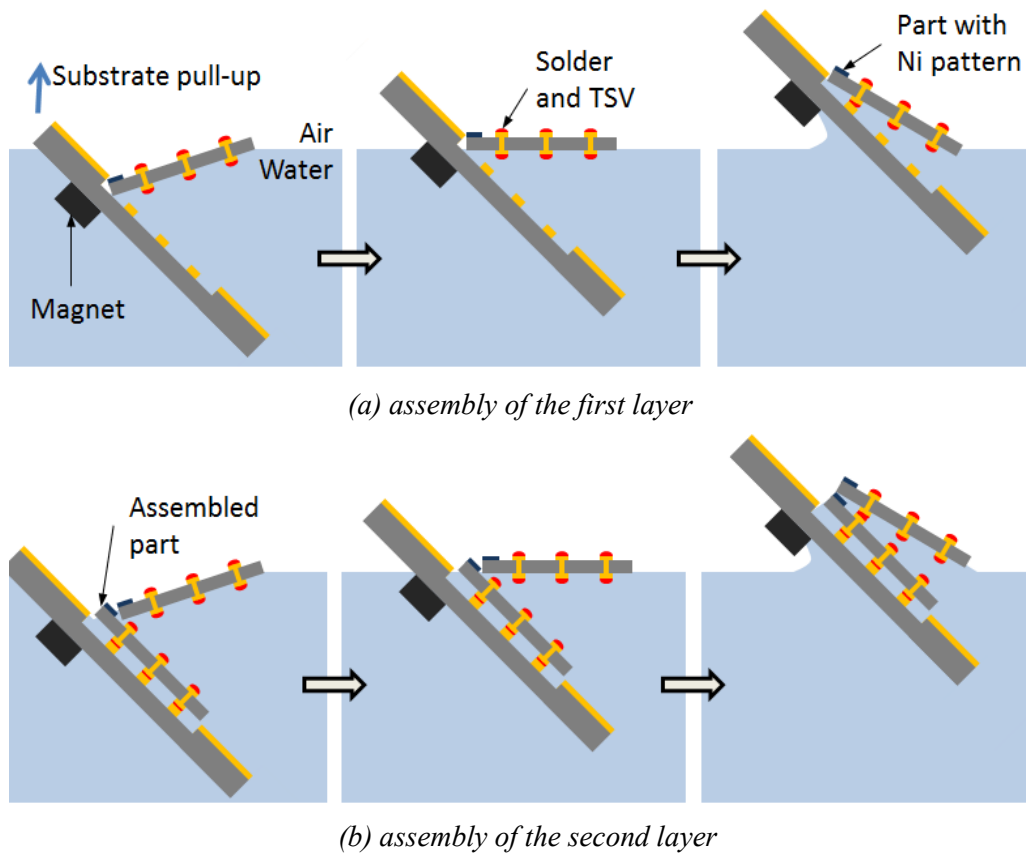


Figure 8.2: Assembly process. After assembly of each layer of parts, solder reflow process is needed for electrical and mechanical connection. 3D integration of multiple layers is achievable through a layer-by-layer assembly.

The correctly registered parts are assembled by substrate pull-up (Figure 8.2(a)). The parts are then mechanically and electrically connected to the binding sites by solder (In/Bi/Sn, 60°C) reflow at 65°C. The magnetic force and the capillary force between parts help part-to-part

alignment. 3D integration of multiple layers is achieved by repeating part assembly and solder reflow (Figure 8.2(b)) processes. Once the first layer of parts is fixed, repeated assembly and solder reflow process achieve 3D multi-layer integration. The maximum number of layers is limited by the magnetic field strength that prevents parts from being withdrawn during substrate pull up.

8.2.2 Fabrication

The fabrication process includes the assembly template fabrication and part fabrication. A combination of photolithography, deep reactive ion etching (DRIE) and metallization is used for the assembly template. As pictured in Figure 8.3(a), the process starts with DRIE through a photoresist mask on a Si wafer in order to form the assembly sites and the trenches connecting those assembly sites. The depth of the etched region is limited to 70 μm in a timed etch. After that, a metal layer of 10 nm Cr and 100 nm Au is deposited using electron beam evaporation. This metal layer is patterned for electrical interconnect by metal etching.

The fabrication process for parts is more complicated compared to the assembly template. Through silicon vias (TSV) are employed for electrical connection in the z-direction. An unconventional method is employed for that purpose. The fabrication process is divided into three steps; via formation, Ni pattern deposition and part release. A silicon-on-insulator (SOI) substrate with a device layer of 100 μm is used. The SOI wafer has a lightly doped p-type device layer (100 μm thick, 20,000 – 50,000 $\Omega\cdot\text{cm}$) and highly doped n-type handle wafer (500 μm thick, 0.001 – 0.005 $\Omega\cdot\text{cm}$) which enables seed layer-less electroplating [46].

Fabrication starts with a photolithography step where 6 TSV locations (diameter of 200 μm) are defined as illustrated in Figure 8.3(b). They are etched with DRIE until the oxide layer is reached. The oxide in openings is removed in HF in order to expose the underlying Si layer. Photoresist on the wafer surface is kept throughout the process. TSVs are fabricated by Au electroplating. A 100 nm Au layer is deposited onto the wafer as the seed layer with e-beam evaporation. A Cr adhesion layer is avoided in order to prevent a strong adhesion between TSV and the handle wafer. Metal layer deposited on the top surface is lifted off by removing the photoresist before electroplating. The highly doped handle wafer is used as the conducting medium for electroplating TSV onto Au layer in the hole.

TSV fabrication is followed by the Ni pattern deposition. A metal layer of 10 nm Cr and 100 nm Au is deposited as the seed layer using e-beam evaporation. The wafer is then spin-coated with 22 μm thick AZ 4620 photoresist and patterned by standard photolithography to define 200 \times 200 μm square windows. A 13 μm tall Ni layer is electroplated through the exposed Au areas. Cr/Au seed layer used in this process is later removed using the electroplated Ni layer as the mask. Part

boundaries are defined in another DRIE step through a photoresist mask. After that, the substrate is left in hydrofluoric acid (HF) in order to release parts from the handle wafer. The released parts are coated with a low-melting point solder (In/Bi/Sn, 60°C) by dip coating. Figure 8.4 shows a substrate and parts with solder bumps. Thickness of a part including solder bumps is about 120 μm .

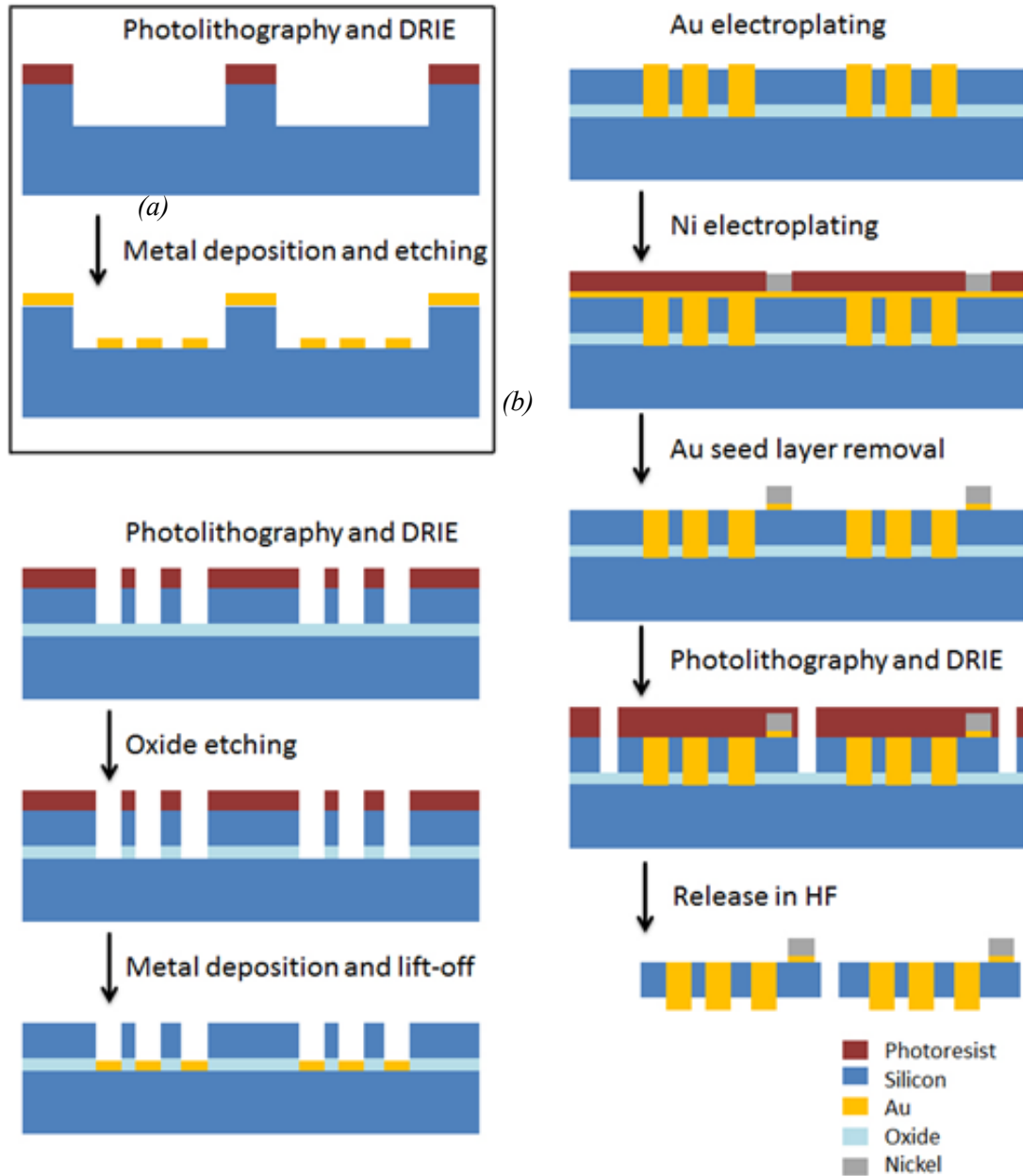


Figure 8.3: Fabrication process flow for (a) the assembly template and (b) parts.

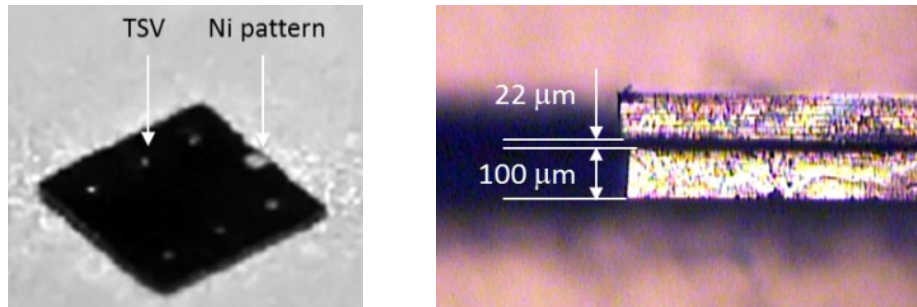


Figure 8.4: Part with gap between parts. (Left) 6 Au TSVs (diameter = $200\ \mu\text{m}$) and a Ni pattern ($200 \times 200 \times 13\ \mu\text{m}^3$) are patterned. (Right) Measured gap between parts is $22\ \mu\text{m}$. Part size is $2000 \times 2000 \times 100\ \mu\text{m}^3$.

8.3 Results

8.3.1 3D integration using self-assembly

8.3.1.1 The effect of the magnetic field

It is observed that 4 layers of parts are the maximum achievable limit by our experimental setup (substrate thickness: $430\ \mu\text{m} = 70\ \mu\text{m}$ deep binding site on $500\ \mu\text{m}$ thick Si wafer, magnet diameter/thickness: $1.56/0.78\ \text{mm}$ (grade N40), part size: $2000 \times 2000 \times 100\ \mu\text{m}^3$, Ni pattern size: $200 \times 200 \times 13\ \mu\text{m}^3$). Assembly fails if the gravitational force during pull-up is larger than the magnetic force.

Thus, we hypothesize that a critical magnetic force exists that guarantees successful assembly. In our FSA system, the magnetic force on a part is determined by the gap between a magnet and a Ni pattern. The minimum magnetic force is experimentally determined by assembly test at various gap values. The maximum gap that allows assembly is found to be $0.99\ \text{mm}$ and a corresponding magnetic force is simulated to be $6.6\ \mu\text{N}$ using COMSOL MultiphysicsTM. Near the threshold magnetic force of $6.6\ \mu\text{N}$, assembly becomes vulnerable to inevitable variations such as magnet-to-binding site alignment, part-to-part alignment, Ni pattern thickness and solder thickness. Thus, assembly becomes more reliable below a gap of $0.99\ \text{mm}$.

Figure 8.5 shows the decrease of the magnetic force with increasing gap between a magnet and a Ni pattern. The gap between parts after solder reflow is measured to be $22\ \mu\text{m}$. Thus, the maximum number of layers of parts with successful assembly is predicted to be 4 layers (total thickness $\approx 0.92\ \text{mm}$ including substrate). This limit can be extended by increasing the magnetic force (larger Ni pattern size, stronger magnetic field, thinner substrate, thinner parts, etc.).

8.3.1.2 Electrical tests

In the proposed FSA system, assembled parts need to be electrically and mechanically fixed through a solder reflow process. The solder bumps on the first layer go through a repeated reflow process as each additional layer is assembled. Thus, degradation of In/Bi/Sn solder over repeated reflow processes needs to be investigated. Resistance through a solder-coated TSV (diameter of $100\ \mu\text{m}$) is measured by repeating the reflow process at 65°C for 20 times. The measured resistance does not show any degradation. Mean and standard deviation are 0.08 and $0.003\ \Omega$, respectively.

Next, TSV resistance values are measured after assembling the 1st and 4th layers (Figure 8.6). Mean and standard deviation of resistance through 4 TSVs in series are measured to be 0.33 and $0.05\ \Omega$. Figure 8.7 shows the comparison between resistance values of single TSV and 4 TSVs in series. Resistance through 4 TSVs is almost 4 times of a single TSV resistance and has wider deviation. Statistical data from these experiments are limited because of low yield in the fabrication process for the parts (Ni patterns on Au film often peeled off during HF release etch). Assembly is limited to 2×2 binding sites due to lack of good parts.

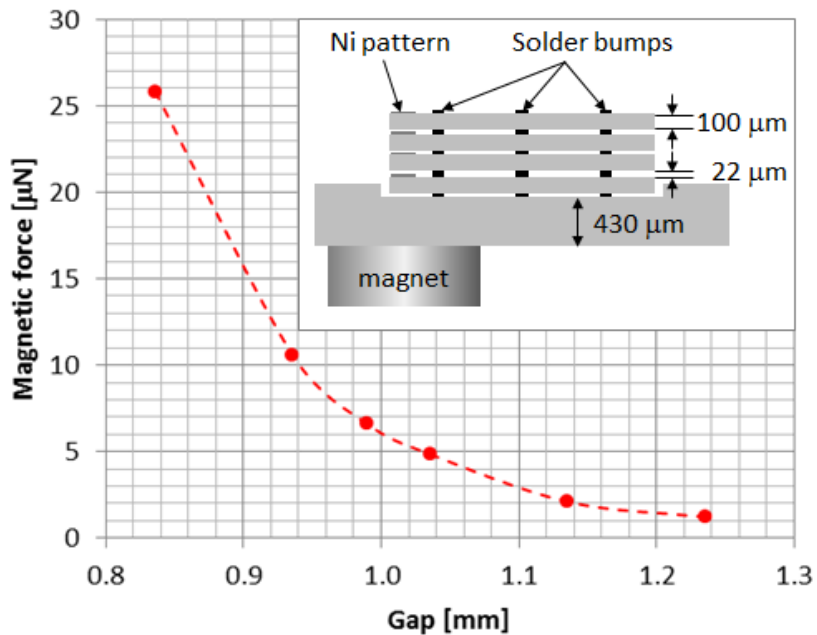


Figure 8.5: Simulated magnetic force decreases with increasing gap. The minimum magnetic force for successful assembly is $6.6\ \mu\text{N}$ (at $0.99\ \text{mm}$). $13\ \mu\text{m}$ thick Ni pattern is assumed. The total gap between a magnet and a Ni pattern on the 4th layer is $918\ \mu\text{m}$.

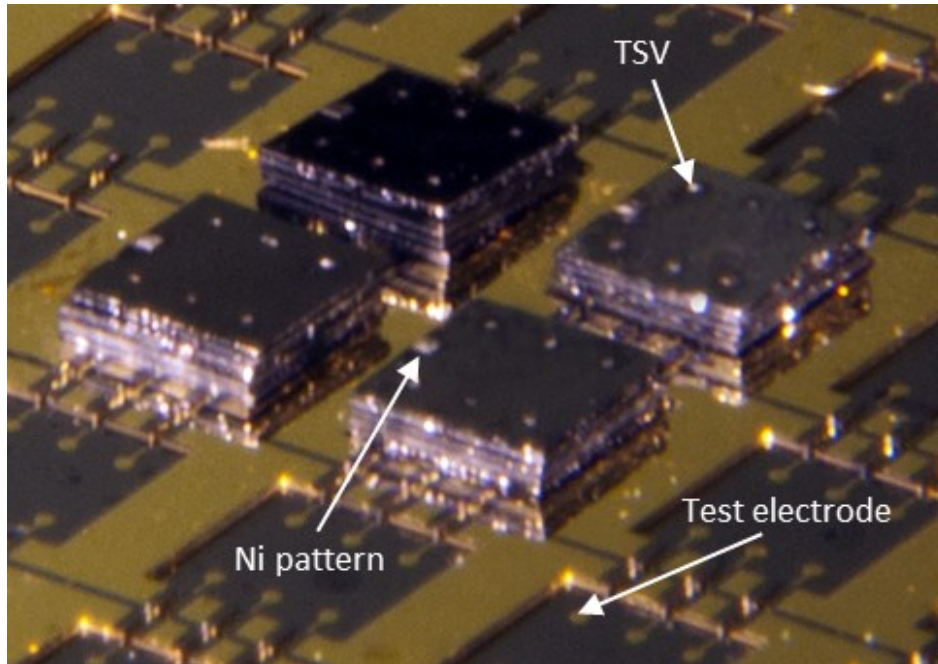


Figure 8.6: Assembly results. 4 layers of 2 mm sized parts are assembled on 2×2 binding sites.

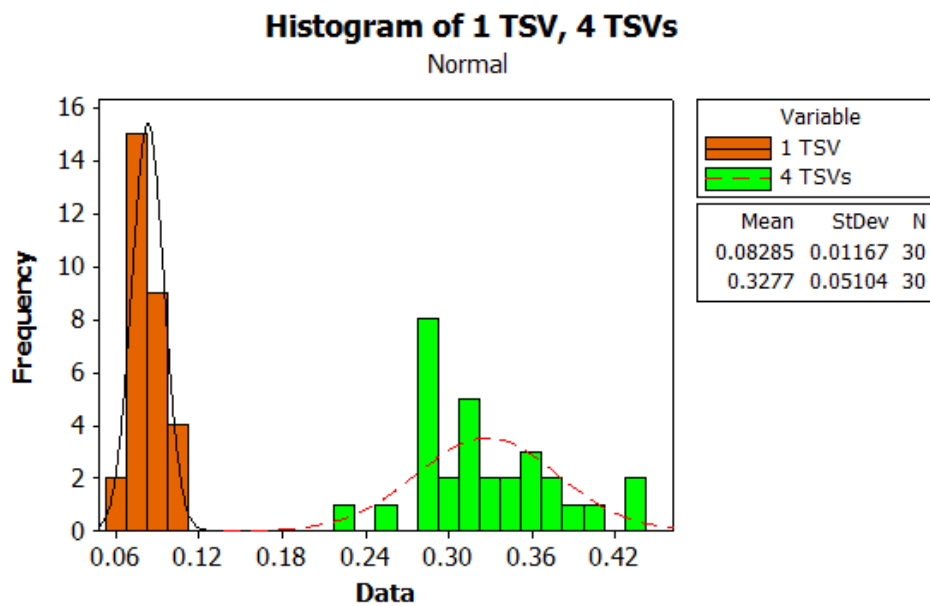


Figure 8.7: Distributions of measured resistance through (a) single TSV (Mean = 0.08Ω , StDev = 0.012Ω) and (b) 4 TSVs in series (Mean = 0.33Ω , StDev = 0.051Ω).

8.4 Conclusions

The first proof-of-concept 3D multi-layer integration using fluidic self-assembly of chip scale parts (100 μm thick) is demonstrated. 4 layers of parts are assembled through layer-by-layer assembly followed by a solder reflow process for electrical and mechanical bonding.

Thin parts with Au TSVs with diameter of 100 μm are successfully fabricated using electroplating without a seed layer. A Ni pattern on a part interacting with magnetic field guarantees assembly with unique orientation. The maximum number of layers that can be achieved using the proposed FSA system is determined by the competition between magnetic force and gravitational force on a part. For given conditions, a threshold magnetic force is experimentally established. Then, the limit of achievable number of layers is predicted using simulation and compared with experimental results. In/Bi/Sn solder shows no degradation over repeated reflow processes. Measured resistance through a single TSV and 4 TSVs in series are 0.08 and 0.33 Ω , respectively.

CHAPTER 9. 3D ORIGAMI

9.1 Introduction

To reach beyond the limit of conventional photolithographically patterned 2D structures, significant research efforts have been made on fabrication of 3D structures. Novel and modified microfabrication methods for 3D microstructures (such as holographic lithography [47], stereo-lithography [48], gray-scale lithography [49], 3D-LIGA [50] and stacking of 2D planar parts as describe in Chapter 8) have been developed.

Another major trend for the fabrication of 3D microstructures is based on self-assembly. 3D origami utilizes the self-folding of 2D planar thin parts or foils to achieve specific geometric shapes and desirable functionalities, e.g. drug delivery and highly efficient photovoltaic cells by entrapping the incident sunlight. The self-folding strategies are based on various actuations such as surface tension [51-54], electroactive polymer (EAP) [55, 56], electrostatic actuation [57], pneumatically actuated Parylene or polydimethylsiloxane (PDMS) structure [58], vacuum suction [59], magnetic dipoles [60], thermal expansion and shrinkage [61], shape-memory alloy and stress-driven actuation [62]. For small structures of nano-to-micro scales, surface tension of interfacial adhesion dominates the deformation and self-assembly [63]. Therefore, 3D self-assembly based on the capillary forces during solid-fluid interactions is regarded as a promising technique and water is the most common medium [53].

However, in these works, the final shapes of self-folding structures are determined by initial design due to a lack of control over the folding angle. In this chapter, as an extension of our FSA, we present a novel self-assembly of 3D structures by controlling the folding angle through the analysis of the magnetic field. As a proof of concept, millimeter-scale pyramid shaped 3D structures with different folding angles (90, 131°) are assembled.

9.2 Assembly overview

Assembly of 3D structures starts from 2D assembly followed by controlling the folding angle of assembled 2D thin parts. 2D assembly of solder-coated thin parts in unique orientation is achieved by fluidic self-assembly described in Chapter 4. The self-assembly system utilizes a magnetic field to control angular orientation of the parts. The magnetic field also folds the assembled thin parts and is manipulated to achieve desired 3D structures. Then, the parts are locked up after the solder reflow process. Here, we describe 2D and 3D assembly of a pyramid, and a model bus.

9.2.1 2D assembly

9.2.1.1 The effect of magnetic field

The magnetic field is a critical component in our assembly system. The magnetic field of rare-earth neodymium iron boron magnets (NeFeB, Grade N40, diameter = thickness = 1/16 inch) is simulated using COMSOL Multiphysics™ (Figure 9.1). The ferromagnetic Ni pattern on a part tends to align along the magnetic flux, thus the simulation results indicate that vertical components are more important in attracting Ni patterned parts on a curved meniscus. To maximize the attracting force, the magnet is aligned to the Ni pattern as shown in Figure 9.1(a).

When assembly is completed, the parts are kept in trenched binding sites by the magnetic field and capillary force between two hydrophilic Si oxide surfaces. Simulation results in Figure 9.1(b) indicate that planar components are negligible near the center of the magnet. Thus, the assembled parts are aligned along the vertical magnetic components again when the capillary force is diminished by water dry-out.

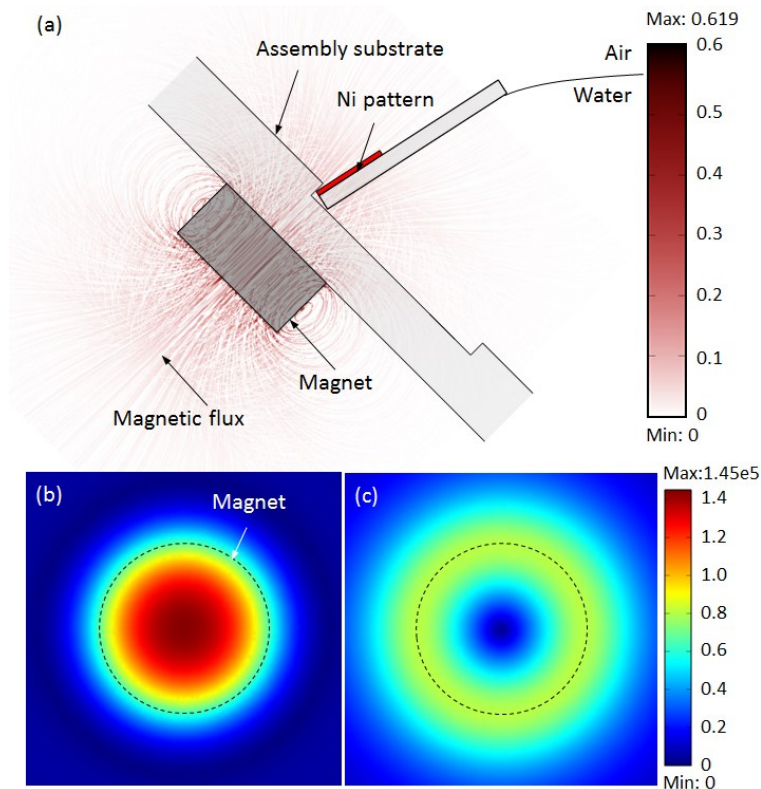


Figure 9.1: Magnetic field of a single magnet. (a) Magnetic flux and its density [T] (cross-sectional view), (b) vertical components (top view) and (c) horizontal components (top view) of magnetic field at the surface of an assembly substrate [A/m].

9.2.2 Fabrication

The assembly substrate and the parts with 12 μm thick Ni patterns (Figure 9.2) are fabricated as described in Chapter 4. The Ni patterns are coated with a low-melting point solder (In/Bi/Sn, 60°C) by dip coating.

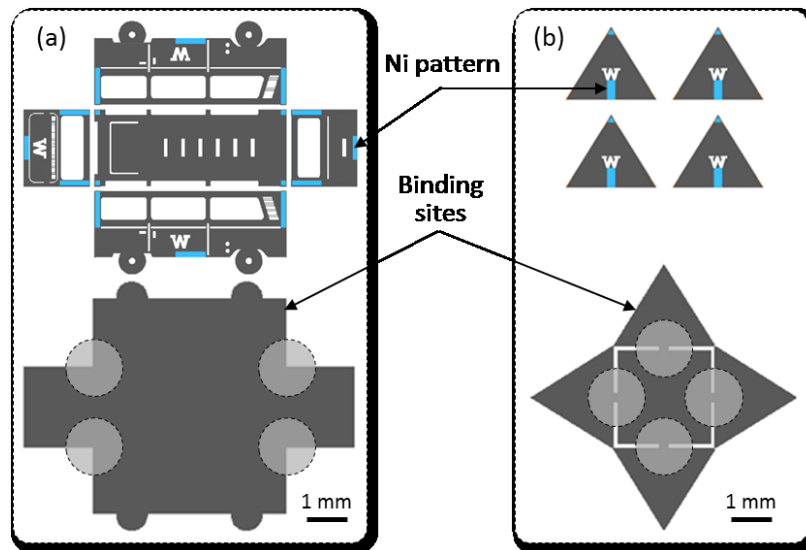


Figure 9.2: Design of binding sites and parts for the Pyramid. Dotted circles present magnets beneath an assembly substrate. (a) Bus shape. (b) Pyramid shape.

9.3 3D structures via self-folding

9.3.1 Self-folding

Self-assembled 3D structures are realized through self-folding by magnetic field. Figure 9.3 illustrates the self-folding with a folding angle of 90° . The 2D parts are held in trenched binding sites by a magnetic field and capillary force. Once the water between the parts and the binding sites is dried out, the magnetic field triggers spontaneous self-folding. The relative position of the magnet determines the folding angle. Polarized flat surfaces of the magnets have the strongest magnetic field at the center, which delimits the folding angle ($0 \leq \theta_f \leq 90^\circ$). Therefore, 3D structures with a folding angle below 90° can be assembled without any additional post-processing.

3D structures with a folding angle larger than 90° are realized by the horizontal shift of magnets (Figure 9.4). However, the bottom of the assembled parts should be pinned by a notch (or similar structures, e.g. triangular binding site for the pyramid shape, see Figure 9.5) to prevent the dislocation of the parts along the shifted magnet center.

Another solution to achieve a folding angle θ_f larger than 90° , instead of shifting magnets, is to use one or more additional magnets after the first self-folding. The simulation result in Figure 9.5 shows the distortion of the magnetic field by adding another magnet. Ni patterned parts are realigned along the deformed magnetic flux. The stationary magnet beneath the assembly substrate serves as a “magnetic hinge” to pin the parts. The magnet surface polarity determines whether to attract or repel the parts (Figure 9.5(b), (c)).

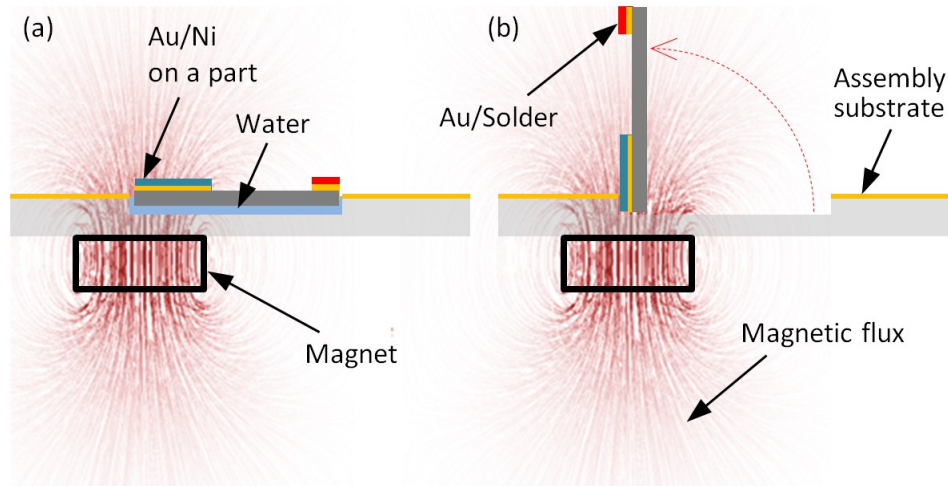


Figure 9.3: Self-folding by magnetic field. Simulated magnetic flux is shown. (a) An assembled part with the water in-between kept in a trenched binding site. (b) Self-folding after drying out of the water.

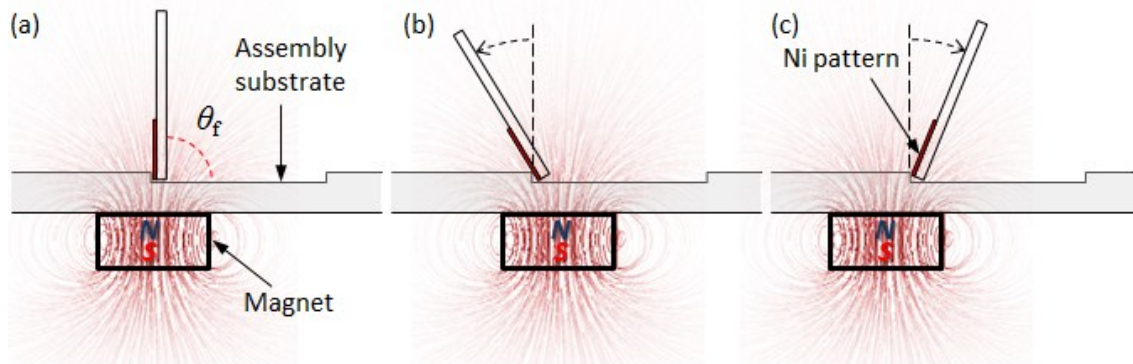


Figure 9.4: Folding angle control by shifting a magnet. To prevent the shift of the part with a magnet, the bottom of the part needs to be pinned by a notch. (a) A standing part (folding angle $\theta_f = 90^\circ$). (b) $\theta_f > 90^\circ$ and (c) $\theta_f < 90^\circ$ is achieved by horizontal shift of the magnet.

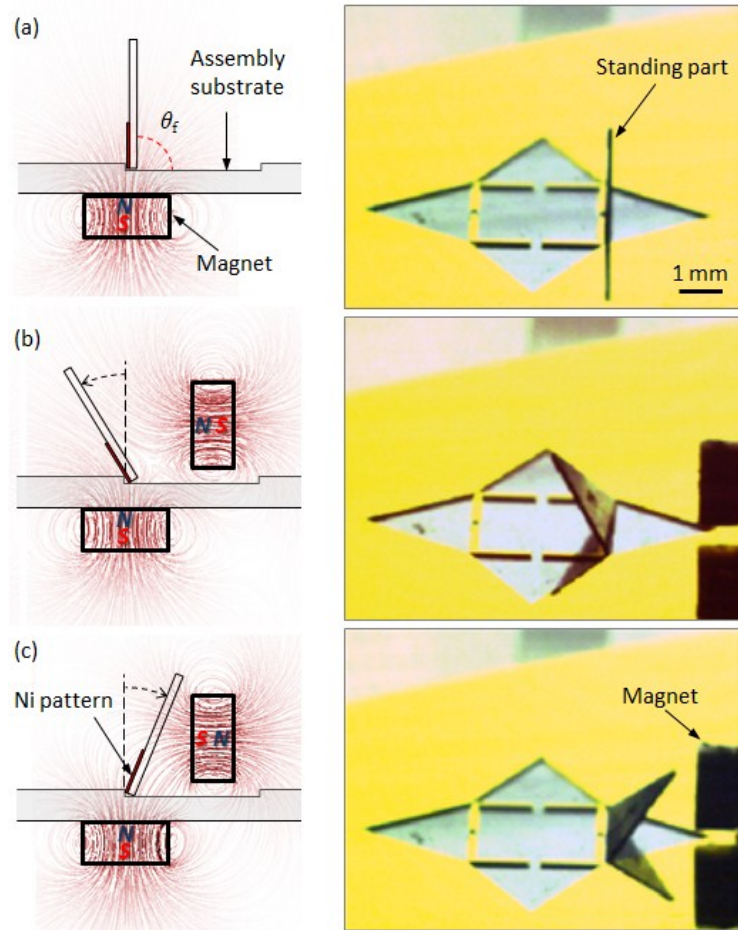


Figure 9.5: Folding angle control using additional magnet. The lower magnets, in combination with the notch in the substrate, act as a hinge to pin the parts. Simulated magnetic flux and test results. (a) A standing part (folding angle $\theta_f = 90^\circ$). (b) $\theta_f > 90^\circ$ and (c) $\theta_f < 90^\circ$ is achieved by additional magnets with opposite polarity.

9.3.2 The bus ($\theta_f = 90^\circ$) and pyramid ($\theta_f > 90^\circ$)

Two 3D structures are realized by self-assembly followed by self-folding. The folding angle is controlled for the pyramid shape (folding angle $\theta_f > 90^\circ$).

To build a self-assembled bus, first, orientation-specific 2D self-assembly of five solder-coated parts (Figure 9.2(a)) is achieved one-by-one by repeating the self-assembly process described in Chapter 4. Then, the parts self-fold at 90° due to the vertical component of the magnetic field (Figure 9.6(a)). Then, the parts are simply locked up after solder reflow at 65°C and released from the assembly substrate (Figure 9.6(b)).

A 3D pyramid has a folding angle larger than 90° , thus the origami process needs an additional

step to control the folding angle. Four triangular parts (Figure 9.2(b)) are self-assembled in 2D on an assembly substrate. After self-folding at 90° by the magnetic field (Figure 9.7(a)), a folding angle of 131° is achieved (Figure 9.7(c)) by either (1) shifting magnets beneath the assembly substrate (Figure 9.4) or (2) adding additional magnets (Figure 9.5). Then, the parts are locked up after solder reflow at 65°C and released (Figure 9.7(d)).

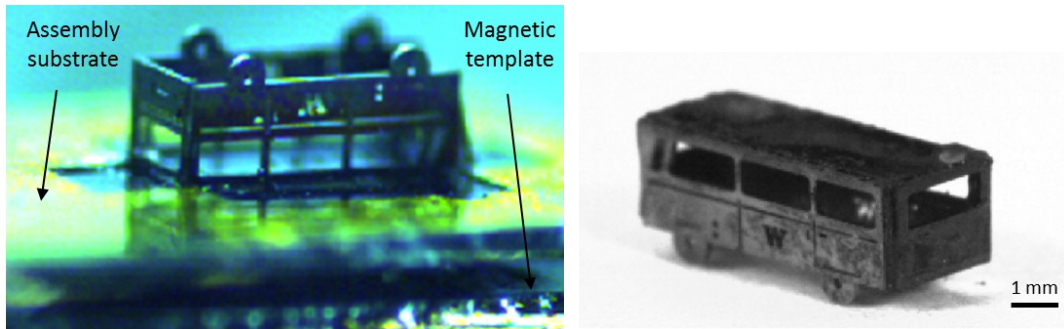


Figure 9.6: Assembly of the Bus by horizontal shift of magnets. (a) After self-folding ($\theta_f \approx 90^\circ$). (b) A released structure after solder reflow.

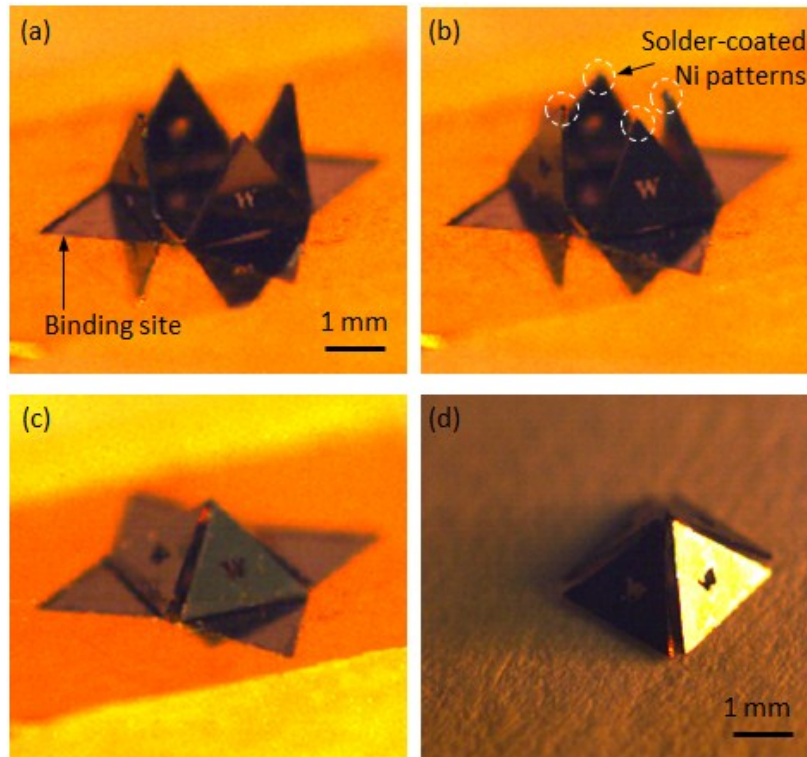


Figure 9.7: Assembly of the pyramid by horizontal shift of magnets. (a) After self-folding ($\theta_f \approx 90^\circ$). (b) Increased folding angle by shifting magnets. (c) The pyramid shape before solder reflow. (d) A released structure after solder reflow.

9.4 Conclusions

Based on the self-folding of a Ni patterned part, which tends to align along the magnetic flux, a novel self-assembly of 3D structures is developed and tested. Unlike other self-assembled 3D structures which have predefined final structures, the folding angle is controlled by changing magnetic field distribution and fixed by solder reflow. As a proof of concept, 3D self-assembly of a bus ($\theta_f = 90^\circ$) and a pyramid ($\theta_f > 90^\circ$) are demonstrated.

CHAPTER 10. CONCLUSIONS AND FUTURE WORK

10.1 Conclusions

The focus of this dissertation is self-assembly of chip-scale parts and its extensions. A novel 2D fluidic self-assembly (FSA) system is introduced and improved to carry out extended functions (control over the orientation of assembled parts, hetero-assembly, optimized assembly of circular parts). Throughout comprehensive modeling and systematic analysis, 3D assembly and 3D origami are realized.

The first FSA system in Figure 2.1 assembles thin square parts ($1000 \times 1000 \times 100$, $3000 \times 3000 \times 100$, $5000 \times 5000 \times 100 \mu\text{m}^3$) from an excess part supply at an air-water interface. System parameters (horizontal and vertical spacing, frequency, acceleration) are optimized and high yield is achieved by applying Faraday waves. The mechanics is analyzed and the maximum substrate tilting angles for each part size are experimentally determined and modeled using surface tension induced torque (capillary torque). The results indicate there is a limit on the lateral size of the parts that can be assembled when we use just one substrate tilting angle. Based on our analysis, we also propose a novel method that is capable of assembling parts of higher lateral dimensions using parametric changes in substrate tilting angle.

The FSA system is improved to assemble parts in unique orientation using a magnetic field and a Ni pattern on a part (Figure 4.1). Experimentally determined critical magnetic force is in good agreement with a derived value from a model of competing forces acting on a part. Based on the developed model and experimental data, a general set of design guidelines is also presented to achieve selective assembly on a substrate.

The orientation-specific FSA system is further improved to assemble different parts simultaneously with the ability of distinguishing desired parts from an unsorted collection of many different parts (Figure 5.1). We develop a statistical strategy to selectively assemble appropriate parts at corresponding sites using a single pull-up process. The key to the parallel self-assembly of heterogeneous parts is the combined effect of Faraday waves and differentiated magnetic forces on different parts. Two types of thin parts ($2000 \times 2000 \times 100$ and $4000 \times 4000 \times 100 \mu\text{m}^3$) assemble onto the same substrate through a one-step process.

The assembly of circular parts is evaluated and optimized. Rotating devices, MEMS oscillators, resonators, and optical components are often in disk shape and particularly difficult to assemble in a specific orientation because of their rotational symmetry. Thus, the assembly of thin circular parts in unique orientation is required. A wide range of rotation angles of assembled parts in trenched binding sites is significantly improved (from 25.5° to 3.7°) throughout the analysis of

in-plane magnetic fields (Figure 6.6, Figure 6.7) which cause rotational force after the parts are placed in the trenches. Compared with assembly of square parts, the assembly rate is increased three-fold due to reduced part-to-part interactions.

This dissertation also presents detailed studies on the effect of fluid viscosity (0.9548 – 0.4665 mPa·s) on assembly rate and yield using derived modeling equations, experimental results and analysis. Drag force (i.e. viscous resistance) dominates part approach and registration process. Lower viscosity achieves higher assembly rate in both tests with and without visual feedback control for application of Faraday waves. The improvement in assembly rate by feedback control becomes more obvious at lower viscosity due to the decreased approach time, the registration time and the efficient use of Faraday waves.

The 2D assembly is further extended into 3D assembly. The first proof-of-concept of 3D integration using self-assembly of chip-scale parts (100 μm thickness) is presented in Figure 8.6. 3D integration is achieved by assembling new parts over previously assembled parts. The maximum number of layers that can be achieved using the proposed FSA system is determined to be 4, limited by the competition between magnetic force and gravitational force on a part. In/Bi/Sn solder shows no degradation of electrical resistance over repeated reflow processes. Measured resistance through a single TSV and 4 TSVs in series are 0.08 and 0.33 Ω , respectively.

Inspired by the reaction of Ni patterned parts to a magnetic field, a novel self-assembly of 3D structures (or 3D origami) is presented. The parts placed in the trenches using our FSA system self-fold after water dry-out. Two methods to control folding angle of parts after self-folding are developed. As a proof of concept, 3D structures with different folding angles (a model bus and a pyramid) are assembled.

10.2 Future work

10.2.1 3D photovoltaic cell

One of the potential applications of 3D self-assembly is photovoltaic (PV) cells. Over 50 years, environmentally clean photovoltaic technology has been developed to get substantial amounts of the electrical energy without burning fossil fuels or creating nuclear fission reactions [64]. PV cells manufactured through industry processes have efficiencies less than 20 %, which indicates over 80 % loss occurs in PV cells. One of the major losses is due to reflection on the cell surface (normally, 30 % of incident sunlight is reflected). Thus, there have been various efforts to obtain high efficiency by increasing the absorbance or reuse of incident sunlight. Novel geometry (WAFFLE structure [65] or inverted pyramid) and surface treatment (nanotubes [66, 67], surface texturing [68]) have been developed as efforts to improve the absorption of light. However, they still reflect part of the incident light.

In addition, one of the significant portions of the cost is silicon wafers that need to be extensively purified to maintain reasonable performance. Reduced cell thickness significantly decreases the cost associated with the use of Si material [69, 70]. In [71], 14–20 μm thick cells are fabricated using SOI wafers or (111) Si wafers and assembled using self-assembly for cost reduction.

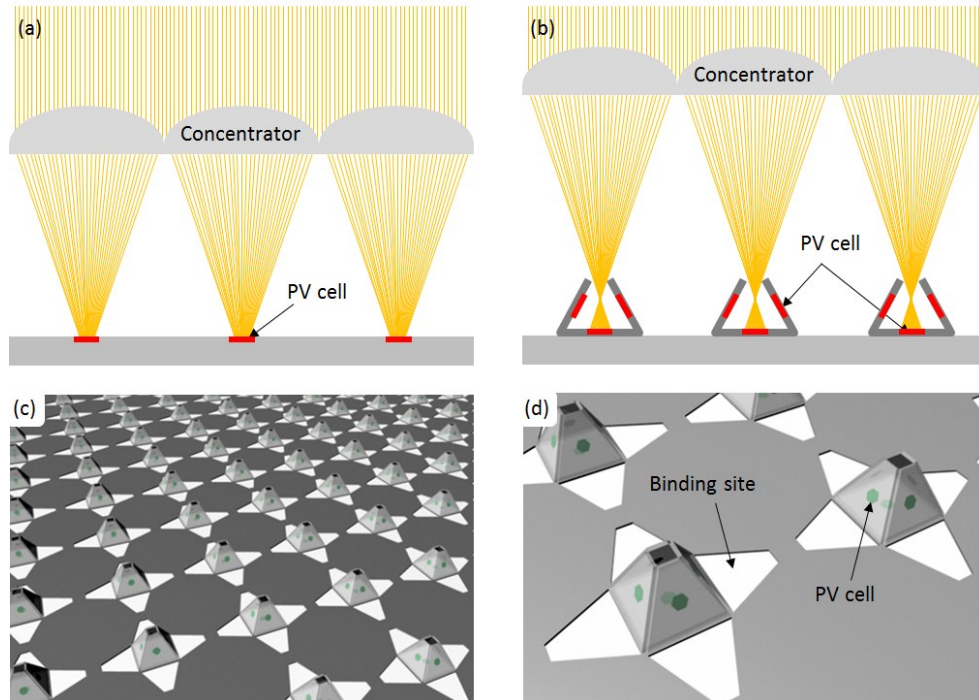


Figure 10.1: Concentrated photovoltaic (CPV) cells. (a) Conventional PV cells reflect the incident light. (b) Proposed PV cells trap the incident light inside the pyramid shaped structure. The PV cells on the tilted parts can be removed and used as mirrors. (c-d) PV cell array.

Here, we propose a novel cost-effective 3D concentrated photovoltaic (CPV) cell structure through 3D self-assembly of thin PV cells (Figure 10.1). Today's CPV cells use a concentrator with a pitch of a few millimeters [72] to collect sunlight over large areas and focus it onto a smaller area of PV cells, however, they still have efficiency loss due to the reflection. The proposed 3D PV cells trap the reflected light inside the 3D structure for reuse. The pyramid shaped PV cell may include 1–5 PV cells. Thus, the proposed CPV cells not only increase the usage of the incident sunlight but also increase the packing density. The usage of the incident light a can be expressed by the equation $a = 1 - r^n$ (a : light usage, r : reflection rate, n : number of reflection) and reaches 99 % after 4 reflections on PV cells.

To test the proposed CPV cells, we need to consider (i) fabrication of PV cells using Si wafers (or

commercially available PV cells can be used), (ii) interconnection between assembled parts and (iii) selection of proper solder considering the operational temperature of PV cells, which rises up to near 80°C (e.g. SANYO HIT Power 200, module temperature 75°C).

10.2.2 Self-disassembly using reusable smart and

In [73, 74], a research group at MIT developed a self-disassembling system that can transform an initial uniform assembly of identical modules into a programmed structure. Each module is a cube which measures 12 mm on each side. Each module is composed of a flex circuit, a brass frame, four electropermanent magnets, and an energy storage capacitor. The self-disassembly of modules is analogous to sculpting. From a large block of modules, the unnecessary modules are disassembled to realize a goal structure. Figure 10.2 shows a dog being formed through the self-disassembly of a block of 27 modules.

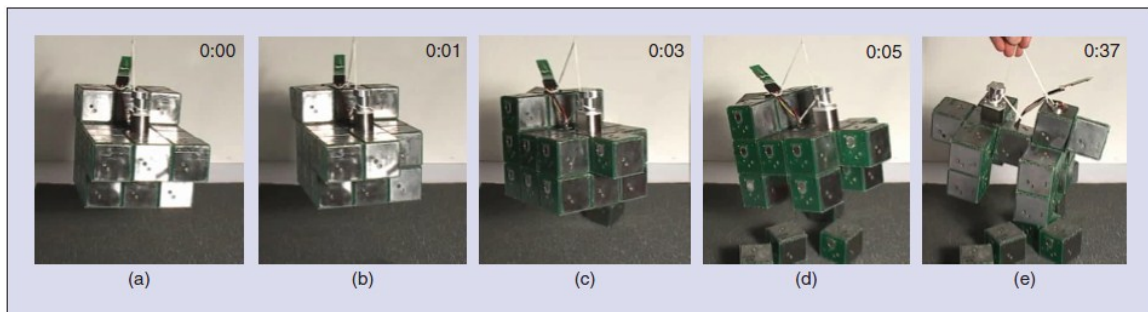


Figure 10.2: A dog-shaped structure can be self-disassembled from an initial configuration of 27 suspended modules. (Picture courtesy of Daniela Rus, Distributed Robotics Laboratory at MIT.)

In a similar manner, smaller structures in a micro-to-millimeter scale can be achieved. We can start with many small smart parts in a container. The surface of each part can be coated with a solder or patterned with shape-memory alloy. Then, a desired structure can be “written” in 2D or 3D using high intensity focused ultrasound (HIFU) or focused x-ray, depending on the material of the parts. A small focal spot size (μm to mm) and temperature for solder reflow or deformation of shape memory-alloy can be easily obtained. During the writing process, mechanical and electrical bonds among the parts near the focal spots are achieved. After the writing process, unnecessary parts are automatically removed.

10.2.3 3D printing

3D printing technology has a great potential that can transform not just science and technology, but also manufacturing and construction [75]. High flexibility in manufacturing geometry, materials opens up the possibility of new designs and new products and simplifies the process

planning and automation required in the flow from design. Scientists have developed 3D printing technology that can create home testing devices, surgical components, artificial bones, blood vessels, and even replacement organs [76, 77].

Unlike today's prevailing 3D printers which build up a goal structure model from bottom to top, a proposed 3D printing method achieves a goal structure by printing from top to bottom using solder reflow process to achieve electrical and mechanical bonding as described in Chapter 8 and Chapter 9. First, the top slice of a desired 3D structure is printed or written using focused ultrasound or focused x-ray from the bottom of an ultrasound- or x-ray-transparent container. Generated heat enables mechanical and electrical bonds among the parts. The holder, which is connected to the first written layer, is pulled up by the height of the parts. We need to shake the containers to fill the empty space below the first layer which is pulled up. Then, the second layer is written, while the first layer is cooled down. By repeating writing and pull-up/cooling, a desired 3D structure can be printed.

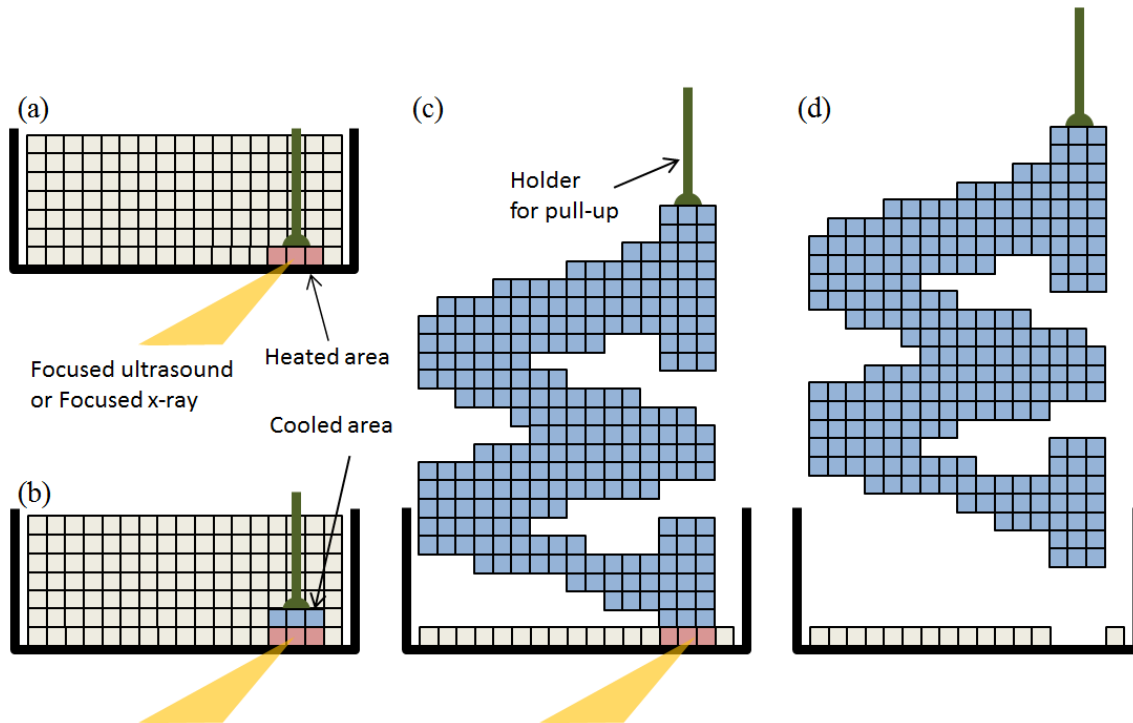


Figure 10.3: A 3D printing scheme for “W” shaped structure. (a) First layer writing. (b) Pull-up and cooling the first layer and second layer writing. (c) Final layer writing. (d) Completed structure.

REFERENCES

1. Philp, D. and J.F. Stoddart, *Self-Assembly in Natural and Unnatural Systems*. Angewandte Chemie International Edition in English, 1996. **35**(11): p. 1154-1196.
2. Choi, I.S., N. Bowden, and G.M. Whitesides, *Shape-Selective Recognition and Self-Assembly of mm-Scale Components*. Journal of the American Chemical Society, 1999. **121**(8): p. 1754-1755.
3. Zhirnov, V.V., R.K. Cavin, and G.I. Bourianoff. *New state variable device opportunities for beyond CMOS: A system perspective*. in *Integrated Circuit Design and Technology and Tutorial, 2008. ICICDT 2008. IEEE International Conference on*. 2008.
4. Kahng, A.B., *Scaling: More than Moore's law*. Design & Test of Computers, IEEE, 2010. **27**(3): p. 86-87.
5. Arden, W., et al., "*More-than-Moore*", in *International Technology Roadmap for Semiconductors*. 2010.
6. Bolanos, M.A. *3D Packaging Technology: Enabling the next wave of applications*. in *Electronic Manufacturing Technology Symposium (IEMT), 2010 34th IEEE/CPMT International*. 2010.
7. Ramadan, Q., Y.S. Uk, and K. Vaidyanathan, *Large scale microcomponents assembly using an external magnetic array*. Applied Physics Letters, 2007. **90**(172502).
8. Srinivasan, U., D. Liepmann, and R.T. Howe, *Microstructure to substrate self-assembly using capillary forces*. Journal of Microelectromechanical Systems, 2001. **10**(1): p. 17-24.
9. Stauth, S.A. and B.A. Parviz, *Self-assembled single-crystal silicon circuits on plastic*. Proceedings of the National Academy of Sciences of the United States of America, 2006. **103**: p. 13922-13927.
10. Knuesel, R.J. and H.O. Jacobs, *Self-assembly of microscopic chiplets at a liquid-liquid-solid interface forming a flexible segmented monocrystalline solar cell*. Proceedings of the National Academy of Sciences of America, 2010. **107**: p. 993-998.
11. Jacobs, H.O., et al., *Fabrication of a cylindrical display by patterned assembly*. Science, 2002. **296**: p. 323-325.
12. Shetye, S.B., I. Eskinazi, and D.P. Arnold, *Magnetic Self-Assembly of Millimeter-Scale Components With Angular Orientation*. Journal of Microelectromechanical Systems, 2010. **19**(3): p. 599-609.
13. Park, S. and K.F. Böhringer, *Fully Dry 2D and 3D Self-assembly with Interlocking Pin Fasteners*, in *The 14th International Conference on Solid-State Sensors, Actuators and Microsystems (Transducers'07)*. 2007: Lyon, France. p. 2079-2082.
14. Fang, J. and K.F. Böhringer, *Vertical and Horizontal Parallel Mounting of Micro Components on a Substrate with High Surface Coverage*, in *IEEE 19th International Conference on Micro Electro Mechanical Systems (MEMS '06)*. 2006. p. 250-253.
15. Hoo, J., R. Baskaran, and K.F. Böhringer, *Programmable batch assembly of microparts with 100%*

- yield, in *Transducers 2009*. 2009: Denver, CO, USA. p. 829 - 832.
16. Park, K.S., et al., *Mechanics and scaling of thin part assembly at a fluidic interface*. Journal of Micromechanics and Microengineering, 2011. **21**(2): p. 025002.
 17. Park, K.S., R. Baskaran, and K.F. Böhringer, *Orientation-specific self-assembly at air-water interface using magnetic field*, in *Transducers 2011*. 2011: Beijing, China.
 18. Zheng, W., P. Buhlmann, and H.O. Jacobs, *Sequential shape-and-solder-directed self-assembly of functional microsystems*. Proceedings of the National Academy of Sciences of America, 2004. **101**: p. 12814–12817.
 19. Zheng, W., J. Chung, and H.O. Jacobs, *Fluidic heterogeneous microsystems assembly and packaging*. Journal of Microelectromechanical Systems, 2006. **15**: p. 864–870.
 20. Tien, J., A. Terfort, and G.M. Whitesides, *Microfabrication through electrostatic self-assembly*. Langmuir, 1997. **13**: p. 5349-5355.
 21. Shetye, S.B., I. Eskinazi, and D.P. Arnold, *Self-assembly of millimeter-scale components using integrated micromagnets*. IEEE Transactions on Magnetics, 2008. **44**: p. 4293-4296.
 22. Ye, H., et al., *Integrating nanowires with substrates using directed assembly and nanoscale soldering*. IEEE Transactions on Nanotechnology 2006. **5**: p. 62–66.
 23. Boncheva, M., D.A. Bruzewicz, and G.M. Whitesides, *Millimeter-scale self-assembly and its applications*. Pure and Applied Chemistry, 2003. **75**: p. 621-630.
 24. Morris, C.J. and B.A. Parviz, *Micro-scale metal contacts for capillary force-driven self-assembly*. Journal of Micromechanics and Microengineering, 2007. **18**(1): p. 015022.
 25. Park, K.S., et al., *Fluidic self-assembly of millimeter scale thin parts on preprogrammed substrate at air-water interface*, in *IEEE 23rd International Conference on Micro Electro Mechanical Systems (MEMS'10)*. 2010: Hong Kong, China. p. 504-507.
 26. Park, K.S., et al., *Part scaling and mechanics of thin part self-assembly in the fluidic phase*, in *IEEE 24th International Conference on Micro Electro Mechanical Systems (MEMS'11)*. 2011: Cancun, Mexico.
 27. Benjamin, T.B. and F. Ursell, *The Stability of the Plane Free Surface of a Liquid in Vertical Periodic Motion*. Proceedings of the Royal Society of London. Series A, Mathematical and Physical Sciences, 1954. **225**(1163): p. 505-515.
 28. Douady, S. and S. Fauve, *Pattern Selection in Faraday Instability*. Europhysics Letters, 1988. **6**(3): p. 221-226.
 29. Eggers, J., *Hydrodynamic theory of forced dewetting*. Physical Review Letters, 2004. **93**: p. 094502.
 30. Hocking, L.M., *Meniscus draw-up and draining*. Euro. Journal of Applied Mathematics, 2001. **12**: p. 195-208.
 31. Xiong, X., et al., *Controlled multibatch self-assembly of microdevices*. Journal of Microelectromechanical Systems, 2003. **12**: p. 117-127.

32. Love, C., et al., *Self-Assembled Monolayers of Thiolates on Metals as a Form of Nanotechnology*. Chemical Reviews, 2005. **105**(4): p. 1103-1170.
33. Smedley, G.T. and D.E. Coles, *A refractive tilting-plate technique for measurement of dynamic contact angles*. Journal of Colloid and Interface Science, 2005. **286**: p. 310-318.
34. Pelesko, J.A., *Self-Assembly*. 2007: Chapman & Hall/CRC.
35. *A-Series Hybrid: Reduce your SiP, MCM and flip chip production costs*. Available from: http://www.assembleon.com/smt-equipment/smt-equipment/aseries/A-Series_Hybrid/.
36. Veldhoven. (2011), *Assembléon introduces A-Series Hybrid in Europe at Productronica*. Available from: http://www.assembleon.com/about-us/news-events/press/ASeries_Hybrid.
37. Smith, J.S., et al., *Methods and apparatus for fluidic self assembly*. 2003, Alien Technology Corporation: USA.
38. Snyder, E.J., J. Chideme, and G.S.W. Craig, *Fluidic self-assembly of semiconductor devices: a promising new method of mass producing flexible circuitry*. Microprocesses and Nanotechnology Conference, 2001 International, 2001: p. 256-257.
39. Chhabra, R.P., *Bubbles, drops, and particles in non-Newtonian fluids*. 1993: CRC Press.
40. Sharma, R. and C.P. Lusignan, *Thermally controlled fluidic self-assembly*. 2010, Eastman Kodak Company: USA.
41. Fang, J. and K.F. Böhringer, *Wafer-level packaging based on uniquely orienting self-assembly (The DUO-SPASS processes)*. Journal of Microelectromechanical Systems, 2006. **15**(3): p. 531-540.
42. Lide, D.R., *CRC Handbook of Chemistry and Physics, 88th Edition (CRC Handbook of Chemistry & Physics)*. 2007: CRC Press.
43. Stokes, G.G., *On the Effect of the Internal Friction of Fluids on the Motion of Pendulums*. Vol. 9. 1851: Transactions of the Cambridge Philosophical Society, Vol. 9, p.8.
44. Reynolds, O., *An experimental investigation of the circumstances which determine whether the motion of water shall be direct or sinuous, and the law of resistance in parallel channels*. Proc. Roy. Soc. Lond., 1883. **35**: p. 84-99.
45. Park, K.S., R. Baskaran, and K.F. Böhringer. *Millimeter-scale thin part self-assembly in the fluidic phase and its sensitivity to part scaling*. in *Proceedings of the ASME 2011 International Manufacturing Science and Engineering Conference (MSEC2011)*. 2011. Corvallis, Oregon, USA.
46. Fujita, T., et al., *Seedlayer-less gold electroplating on silicon surface for MEMS applications*. Sensors and Actuators A: Physical, 2007. **135**(1): p. 50-57.
47. Brook, J. and R. Dändliker, *Submicrometer holographic photolithography*. Solid State Technology, 1989. **33**: p. 91-94.
48. Ikuta, K. and K. Hirowatari. *Real three dimensional micro fabrication using stereo lithography and metal molding*. in *Micro Electro Mechanical Systems, 1993, MEMS '93, Proceedings An Investigation of Micro Structures, Sensors, Actuators, Machines and Systems. IEEE*. 1993.

49. Waits, C.M., et al., *Microfabrication of 3D silicon MEMS structures using gray-scale lithography and deep reactive ion etching*. Sensors and Actuators A: Physical, 2005. **119**(1): p. 245-253.
50. Mekaru, H., et al., *Fabrication of a spiral microcoil using a 3D-LIGA process*. Microsystem Technologies, 2007. **13**(3): p. 393-402.
51. Guo, X., et al., *Two- and three-dimensional folding of thin film single-crystalline silicon for photovoltaic power applications*. Proceedings of the National Academy of Sciences, 2009. **106**(48): p. 20149-20154.
52. Py, C., et al., *Capillarity induced folding of elastic sheets*. The European Physical Journal - Special Topics, 2009. **166**(1): p. 67-71.
53. Li, H., et al., *Capillary induced self-assembly of thin foils into 3D structures*. Journal of the Mechanics and Physics of Solids, 2010. **58**(12): p. 2033-2042.
54. Randall, C.L., E. Gultepe, and D.H. Gracias, *Self-folding devices and materials for biomedical applications*. Trends in Biotechnology, 2012. **30**(3): p. 138-146.
55. Jager, E.W.H., E. Smela, and O. Inganäs, *Microfabricating Conjugated Polymer Actuators*. Science, 2000. **290**(5496): p. 1540-1545.
56. Okuzaki, H., et al., *A biomorphic origami actuator fabricated by folding a conducting paper*. Journal of Physics: Conference Series, 2008. **127**(1): p. 012001.
57. Chen, C.-H., et al., *A three-dimensional flexible microprobe array for neural recording assembled through electrostatic actuation*. Lab on a Chip, 2011. **11**(9): p. 1647-1655.
58. Lu, Y.-W. and C.-J. Kim, *Microhand for biological applications*. Applied Physics Letters, 2006. **89**(16): p. 164101-164101-3.
59. Zotov, S.A., et al., *Folded MEMS Pyramid Inertial Measurement Unit*. Sensors Journal, IEEE, 2011. **11**(11): p. 2780-2789.
60. Boncheva, M., et al., *Magnetic self-assembly of three-dimensional surfaces from planar sheets*. Proceedings of the National Academy of Sciences of the United States of America, 2005. **102**(11): p. 3924-3929.
61. Suzuki, K., et al., *Self-assembly of three dimensional micro mechanisms using thermal shrinkage of polyimide*. Microsystem Technologies, 2007. **13**(8): p. 1047-1053.
62. Leong, T.G., et al., *Thin film stress driven self-folding of microstructured containers*. Small (Weinheim an der Bergstrasse, Germany), 2008. **4**(10): p. 1605-9.
63. Hsia, K.J., et al., *Collapse of stamps for soft lithography due to interfacial adhesion*. Applied Physics Letters, 2005. **86**(15): p. 154106-154106-3.
64. Luque, A. and S. Hegedus, *Handbook of Photovoltaic Science and Engineering*. 2003: Wiley.
65. Leistiko, O. *The waffle: a new photovoltaic diode geometry having high efficiency and backside contacts*. in *Photovoltaic Energy Conversion, 1994., Conference Record of the Twenty Fourth. IEEE Photovoltaic Specialists Conference - 1994, 1994 IEEE First World Conference on*. 1994.

66. Camacho, R., et al., *Carbon nanotube arrays for photovoltaic applications*. Journal of the Materials, 2007. **59**(3): p. 39-42.
67. Garnett, E. and P. Yang, *Light Trapping in Silicon Nanowire Solar Cells*. Nano Letters, 2010. **10**(3): p. 1082-1087.
68. Macdonald, D.H., et al., *Texturing industrial multicrystalline silicon solar cells*. Solar Energy, 2004. **76**(1-3): p. 277-283.
69. Nielson, G.N., et al. *Microscale PV Cells for Concentrated PV Applications*. in *24th European Photovoltaic Solar Energy Conference*. 2009. Hamburg, Germany.
70. Gupta, V., et al., *Microsystems-Enabled Photovoltaics: A Path to the Widespread Harnessing of Solar Energy*, in *Future Photovoltaics, May 2010*. 2010, Future Photovoltaics.
71. Nielson, G.N., et al. *Microscale c-Si (c)PV cells for low-cost power*. in *Photovoltaic Specialists Conference (PVSC), 2009 34th IEEE*. 2009.
72. Karp, J.H., E.J. Tremblay, and J.E. Ford. *Micro-optic solar concentration and next-generation prototypes*. in *Photovoltaic Specialists Conference (PVSC), 2010 35th IEEE*. 2010.
73. Gilpin, K., et al., *Robot pebbles: One centimeter modules for programmable matter through self-disassembly*. Proc IEEE Int Conf Rob Autom Proceedings - IEEE International Conference on Robotics and Automation, 2010: p. 2485-2492.
74. Gilpin, K. and D. Rus, *Modular Robot Systems From self-assembly to self-disassembly*. IEEE robotics & automation magazine /, 2010. **17**(3): p. 38.
75. *Print preview - The printing press changed the world; three-dimensional printing could do the same*. Nature, 2012. **487**(7405): p. 6-6.
76. Fedorovich, N.E., et al., *Organ printing: the future of bone regeneration?* Trends in Biotechnology, 2011. **29**(12): p. 601-606.
77. Butscher, A., et al., *Structural and material approaches to bone tissue engineering in powder-based three-dimensional printing*. Acta Biomaterialia, 2011. **7**(3): p. 907-920.

CURRICULUM VITAE

KWANG SOON PARK

Expertise

- MEMS/Semiconductor/Display process technology
- 2D/3D MEMS, Self-assembly, Packaging
- LCD, Flat panel display (Design, Simulation, Measurement)
- Six Sigma MBB (Master Black Belt), DOE, ANOVA, RSM, Gage R&R, Taguchi method, Quality control, Design for manufacturability and yield
- CAD, Simulation

Strength

- ***Self-Assembly, Novel Packaging (supported by Intel and DARPA)***
 - High yield fluidic self-assembly (FSA) in unique orientation
 - Self-assembly of arbitrarily shaped components
 - 2D/3D structure
 - Microfluidic analysis
- ***3D MEMS, 3D Packaging using Self-Assembly (supported by Intel and DARPA)***
 - 3D structure using self-folding
 - Vertical electrical connection for smart 3D devices & 3D integration
- ***LCD Panel Design***
 - Mask layout of TFT device, TFT circuits, Color filter, Black matrix, Cell design, Pixel rendering
 - Schematic Simulation (SPICE) & Optimization of design & process
 - Panel Simulation: a-Si TFT modeling, Optoelectric and Schematic Simulation
 - Test & Evaluation: Electrical and optical performance
 - Commercialization of LCDs
- ***Strong Statistical Background***
 - Six sigma MBB : Project consultant, Quality control over 3 years in LG Display
 - System analysis & Parameter optimization
 - Tolerance analysis, Design for manufacturability
 - Design of experiment (DOE), Analysis of variances (ANOVA), Response surface method (RSM), Taguchi design
 - Robust design with six sigma (DOE, Taguchi design)
 - Parameter contribution analysis

- **Software**

- CADENCE tools: Layout, DRC, LVS
- Matlab, C, Visual basic, Skill language (CADENCE)
- Minitab (Statistical and process management software for six sigma and quality improvement)
- COMSOL Multiphysics, CoventorWare, Flow3D
- SPICE, Parameter extraction
- ExpertLCD, Raphael, Techwiz LCD
- Maya, 3D Max, Sketchup

Professional Experiences

- Senior research engineer, LG Display Co., Ltd, R&D center: 2000.02 - 2008.06

Education

- Ph.D., Electrical engineering at University of Washington (Seattle, WA, USA) : 2008.09 - 2012.06
- MS, Electrical engineering at Kyungpook National University (Daegu, South Korea): 1998.03 - 2000.02
- BS, Electrical engineering at Kyungpook National University (Daegu, South Korea): 1994.03 - 1998.02

Career Highlight

Ph.D. Research

- *Fluidic self-assembly (2008 – 2012)*
 - 3D integration of thin parts using self-assembly
 - Millimeter sized parts in Unique Orientation
 - Square, rectangular, circular and arbitrarily shaped parts
 - Modeling, simulation, parametric analysis and optimization

Strongly contributed to Technical Development & Commercialization of LCDs

- *Model development for mass production (2000 - 2003)*
 - 20.1" UXGA (LM201U01) : LG Display's 1st UXGA IPS panel : Best R&D Prize (2000)
 - 14.1" XGA (LP141X10, X12)
 - 15.4" WXGA (LP154WX1) : World's 1st 15.4" Wide model
 - 17.1" WXGA (LP171W01) : World's 1st 17.1" Wide model
- *Technology development (2004 - 2008)*
 - 4 Mask high aperture ratio LCD (currently applied all TN mode LCDs in the company)
 - Integration of gate driver ICs on TFT glass (to eliminate gate driver ICs) : Best R&D prize (2006)
 - IPS panel robust design project : Silver R&D prize in 2008
 - Program development for CADENCE layout design
 - Failure mode analysis

- Instructor : SmartSPICE, Photomask design, Display engineering, Robust design
- *Six sigma (2003 - 2008)*
 - BB (Black Belt, 2003) : Best six sigma project award
 - MBB (Master black belt, 2005) : Instructor and consultant of six sigma projects
 - Trained in Taguchi DOE (Design of Experiment) : Accomplished 3 projects for robust design

Master Research

- Flow sensor (1998 - 2000)
 - Sensor design, Simulation and optimization
 - Flow rate, Flow direction, Temperature compensation

Honors and Awards

- Rushmer innovator fellowship (2011-2012)
- Electrical engineering three-year RA/TA Fellowship (2008-2011)
- Collage of engineering Max E. Gellert fellowship (2008-2009)
- Silver R&D prize (2008): IPS panel robust design project
- Master black belt (2006): Six Sigma
- Best R&D prize (2006): Integration of Gate Driver ICs on TFT glass
- Best six sigma project (2003)
- Best R&D prize (2000): LG Display's 1st UXGA IPS mode panel
- Taekwang group, Ilju academy foundation fellowship (1994-1998)

Publications

Journal

- K. S. Park, X. Xiong, R. Baskaran, and K. F. Böhringer, "Mechanics and scaling of thin part assembly at a fluidic interface," *Journal of Micromechanics and Microengineering*, vol. 21, p. 025002, 2011.
- K. S. Park, J. H. Hoo, R. Baskaran, and K. F. Böhringer, "Parallel heterogeneous integration of chip-scale parts by self-assembly," *Journal of Microelectromechanical Systems Letters*, 2012. (Accepted, DOI 10.1109/JMEMS.2012. 2205905)
- K. S. Park, J. H. Hoo, R. Baskaran, and K. F. Böhringer, "Orientation controlled parallel assembly at air-water interface," *Journal of Micromechanics and Microengineering*, 2012 (Accepted: 08/13/2012)
- K. S. Park, J. H. Hoo, R. Baskaran, and K. F. Böhringer, " Optimization of angular alignment in self-assembly of thin parts at an air-water interface," *Journal of Microelectromechanical Systems Letters*, 2012. (Submitted)
- K. S. Park, J. H. Hoo, R. Baskaran, and K. F. Böhringer, "Effect of fluid viscosity on dynamics of self-assembly at air-water interface," *Journal of Microelectromechanical Systems Letters*, 2012. (Submitted)

Conference

- K. S. Park, J. H. Hoo, C. Varel, R. Baskaran, and K. F. Böhringer, "3D integration using self-assembly at air-water interface," Solid-state Sensors, Actuators and Microsystems Workshop (Hilton Head Island, South Carolina, 2012).
- J. H. H. K. S. Park, C. Varel, R. Baskaran, and K. F. Böhringer, "Wafer-level high density integration of surface mount technology components in through-silicon trehches," presented at the IEEE 25th International Conference on Micro Electro Mechanical Systems (MEMS'12), Paris, France, 2012 .
- K. S. Park, R. Baskaran, and K. F. Böhringer, "Programmable batch assembly of microparts," presented at the Technologies for Future Micro-Nano Manufacturing, Napa, California, USA, 2011.
- K. S. Park, R. Baskaran, and K. F. Böhringer, "Orientation-specific self-assembly at air-water interface using magnetic field," presented at the Transducers 2011, Beijing, China, 2011.
- J. H. Hoo, K. S. Park, R. Baskaran, and K. F. Böhringer, "Programmable self-assembly for microsystem integration," presented at the Transducers 2011, Beijing, China, 2011.
- K. S. Park, R. Baskaran, and K. F. Böhringer, "Millimeter-scale thin part self-assembly in the fluidic phase and its sensitivity to part scaling," in Proceedings of the ASME 2011 International Manufacturing Science and Engineering Conference (MSEC2011), Corvallis, Oregon, USA, 2011.
- K. S. Park, R. Baskaran, and K. F. Böhringer, "Analysis of self-assembly of thin part at fluidic interface and its modification for orientation-specific assembly," presented at the Foundation of Nanoscience (FNANO) 2011, Snowbird, Utah, USA, 2011.
- K. S. Park, X. Xiong, R. Baskaran, and K. F. Böhringer, "Part size and mechanics of thin part self-assembly in the fluidic phase," presented at the IEEE 24th International Conference on Micro Electro Mechanical Systems (MEMS'11), Cancun, Mexico, 2011.
- K. S. Park, X. Xiong, R. Baskaran, and K. F. Böhringer, "Fluidic self-assembly of millimeter scale thin parts on preprogrammed substrate at air-water interface," presented at the IEEE 23rd International Conference on Micro Electro Mechanical Systems (MEMS'10), Hong Kong, China, 2010.

Patents

- 16 USA, 1 UK, 1 France, 2 Germany, 3 Japan, 4 China, 1 Taiwan, 49 Korea

Country		Patent No.	Date Issued	Title
USA (US)	1	2006279687(A1) 7808608(B2)	12/14/2006 10/05/2010	☛ Liquid crystal display device
	2	2007188432(A1) 7750884(B2)	08/16/2007 07/06/2010	☛ Method and apparatus of driving liquid crystal display device
	3	2003189685(A1) 7643121(B2)	10/09/2003 01/05/2010	☛ Liquid crystal display of line-on-glass type
	4	2006227094(A1) 7583247(B2)	06/12/2006 09/01/2009	☛ Gate driver for a display device and method of driving the same
	5	2006290841(A1) 7532277(B2)	12/28/2006 05/12/2009	☛ Liquid crystal display device using align mark

	6	2005041189(A1) 7443479(B2)	02/24/2005 10/28/2008	❖ Liquid crystal display preventing electronic corrosion and method of fabricating the same
	7	2005225523(A1) 7397453(B2)	10/13/2005 07/08/2008	❖ Liquid crystal display device and driving method thereof
	8	2004263770(A1) 7256861(B2)	12/30/2004 08/14/2007	❖ Liquid crystal display device
	9	2004125278(A1) 7239363(B2)	07/01/2004 07/03/2007	❖ Liquid crystal display device including color filter
	10	2004119673(A1) 7116303(B2)	06/24/2004 10/03/2006	❖ Apparatus and method of driving liquid crystal display device
	11	2004135751(A1) 7113160(B2)	07/15/2004 09/26/2006	❖ Method and apparatus of driving liquid crystal display device
	12	2004119671(A1) 7084842(B2)	06/24/2004 08/01/2006	❖ Apparatus and method for driving liquid crystal display device
	13	2004135752(A1) 7057592(B2)	07/15/2004 06/06/2006	❖ Liquid crystal display device and driving method thereof
	14	2003218699(A1) 6927810(B2)	11/27/2003 08/09/2005	❖ Liquid crystal display device having indented gate electrode and fabricating method thereof
	15	2003189679(A1) 6842203(B2)	10/09/2003 01/11/2005	❖ Liquid crystal display of line-on-glass type
	16	2007002218(A1)	01/14/2007	❖ Color filter substrate and method for fabricating the same
U.K. (GB)	1	2388950(A) 2388950(B)	11/26/2003 08/04/2004	❖ Liquid crystal display device and driving method thereof
FRANCE (FR)	1	2840106(A1) 2840106(B1)	11/28/2003 05/05/2006	❖ Liquid crystal display device and driving method thereof
GERMANY (DE)	1	102006029223(A1) 102006029223(B4)	12/28/2006 06/09/2011	❖ LCD display device comprise alignment marks arranged on respective sides of gate line on lower substrate
	2	10323406(A1)	12/04/2003	❖ Liquid crystal display device having sunken gate electrode and fabricating method thereof
JAPAN (JP)	1	2006338025(A) 4546420(B2)	12/14/2006 09/16/2010	❖ Liquid crystal display element
	2	2007011325(A)	01/18/2007	❖ Color filter substrate and method for fabricating the same
	3	15347558(A)	12/05/2003	❖ Array substrate for liquid crystal display device, manufacturing method therefor and thin film transistor
CHINA (CN)	1	1873484(A) 100442114(C)	12/06/2006 12/10/2008	❖ Liquid crystal display device
	2	1892261(A) 100426013(C)	01/10/2007 10/15/2008	❖ Color filter substrate and method of fabricating the same
	3	1459658(A) 100390649(C)	12/03/2003 05/28/2008	❖ Liquid crystal display device with concave grid electrode and mfg. method thereof
	4	1680843(A) 100381886(C)	10/12/2005 04/16/2008	❖ Liquid crystal display device and driving method thereof
TIWAN (TW)	1	594342(B)	06/21/2004	❖ Liquid crystal display device having sunken gate electrode and fabricating method thereof

KOREA (KR)	2008(1)
	20080092570(A)
	2007(5)
	20070071703(A), 20070021403(A), 20070002145(A), 20070001390(A), 20070000547(A)
	2006(7)
	20060125138(A), 20060113089(A), 20060107636(A) 20060105327(A), 20060104587(A), 20060103590(A), 20060032035(A)
	2005(10)
	20050105591(A), 20050099022(A) & 101009674(B1), 20050086314(A) & 100976559(B1), 20050082347(A), 20050070446(A) & 101006781(B1), 20050068855(A) & 100961268(B1), 20050034957(A) & 100575231(B1), 20050032247(A), 20050020330(A), 20050000652(A) & 100922794(B1)
	2004(8)
	20040068774(A), 20040062154(A) & 100936949(B1), 20040061201(A), 20040055414(A) & 100898791(B1), 20040055338(A) & 100923350(B1),& 20040055336(A) & 100942836(B1), 20040055335(A) & 100942833(B1), 20040035276(A)
2003(10)	
20030095904(A) & 100843478(B1), 20030094849(A), 20030093789(A), 20030093472(A) & 100854948(B1), 20030090403(A), 20030090339(A) & 100491821(B1), 20030080325(A) & 100855486(B1), 20030080324(A) & 100847817(B1), 20030054241(A) & 100487431(B1), 20030026760(A) & 100796486(B1)	